NOTICE

The quality of this microform is heavily dependent upon the quality of the original thesis submitted for microfilming. Every effort has been made to ensure the highest quality of reproduction possible.

If pages are missing, contact the university which granted the degree.

Some pages may have indistinct print especially if the original pages were typed with a poor typewriter ribbon or if the university sent us an inferior photocopy.

Previously copyrighted materials (journal articles, published tests, etc.) are not filmed.

Reproduction in full or in part of this microform is governed by the Canadian Copyright Act, R.S.C. 1970, c. C-30.

AVIS

La qualité de cette microforme dépend grandement de la qualité de la thèse soumise au microfilmage. Nous avons tout fait pour assurer une qualité supérieure de reproduction.

S'il manque des pages, veuillez communiquer avec l'université qui a conféré le grade.

La qualité d'impression de certaines pages peut laisser à désirer, surtout si les pages originales ont été dactylographiées à l'aide d'un ruban usé ou si l'université nous a fait parvenir une photocopie de qualité inférieure.

Les documents qui font déjà l'objet d'un droit d'auteur (articles de revue, tests publiés, etc.) ne sont pas microfilmés.

La reproduction, même partielle, de cette microforme est soumise à la Loi canadienne sur le droit d'auteur, SRC 1970, c. C-30.

RADIATION AND SCATTERING OF STRUCTURES ABOVE PERFECT AND IMPERFECT GROUND

By

Elim CHAN, B.A.Sc.

A thesis submitted to the
School of Graduate Studies and Research
in partial fulfillment of the requirements
for the degree of

Master of Applied Science

Ottawa-Carleton Institute for Electrical Engineering
Department of Electrical Engineering
Faculty of Engineering
University of Ottawa

ISBN 0-315-46733-9

UNIVERSITÉ D'OTTAWA
UNIVERSITY OF OTTAWA

The University of Ottawa requires the signatures of all persons using or photocopying this thesis. Please sign below, and give address and date.

ACKNOWLEDGEMENTS

The author wishes to express her most sincere gratitude to her supervisor, Dr. M.M. Ney, for his valuable advice and guidance throughout this work.

The author is particularly grateful to Dr. G.J. Burke for providing the Numerical Electromagnetic Code (NEC) used in this thesis. Thanks are also due to Dr. S.S. Stuchly for providing the experimental facilities and Mr M. Bui for the experimental results that were needed for this thesis.

The author would also like to thank the staff and colleagues of the Department of Electrical Engineering at the University of Ottawa with whom she had the pleasure of knowing, particularly, the electromagnetic group, for their suggestions and help throughout this thesis.

The author is specially grateful to Mrs S. Meszaros, Dr. M. Stubbs in CRC for proof reading the manuscript, and Mr W. Yue for his help on Tex format in this text.

Finally, special thanks are given to the parents and sister of the author for their encouragement and support.

ABSTRACT

The near and far field scattering of structures above perfect and imperfect grounds is investigated. A numerical method, which is suitable for complex geometries above imperfect ground, is used to evaluate the fields distribution of simple wire antenna structures that could be used as part of a mobile surveillance system. Alarm scenario for different wire antenna configurations are simulated using an electrical model of intruders.

For near-field applications, the numerical method used in the computer simulations showed oscillatory solutions that were not confirmed by the measurements. As a result, a test problem, which consisted of determining the near field scattered by a perfectly conducting hemisphere above perfect ground and located in the far field of a quarter-wave monopole antenna was examined. Since no theoretical solution is available for this problem. A new approach is presented using a spherical eigenmode decomposition.

Results given by the eigenmode approach show that the oscillatory nature of the solution given by the numerical method is due to numerical instabilities that may occur when fields are computed very near scattering structures.

CONTENTS

LIST OF TABLES

LIST OF FIGURES

GLOSSARY

a = radius of conducting cylinder.

a_n^r, b_n^r = coefficents of scattered field of conducting sphere.

$\mathrm{E}_{\pm}^{\mathrm{I}}(\mathrm{r})$ = incident electric field in Sommerfeld method.

$\mathrm{E}_{\pm}^{\mathrm{R}}(\mathrm{r})$ = electric field reflected by the interface in Sommerfeld method.

$\mathrm{E}_{\mathrm{inc}}$ = incident electric field.

$\mathrm{E}_{\mathrm{scat}}$ = scattered electric field.

$\mathrm{E}_{\mathrm{tol}}$ = total electric field.

f_j = basis functions of moment method.

g_0 = free space kernel.

g_g = image kernel term.

H = radiation pattern of halfwave dipole.

$H_n^{(2)}(x)$ = Hankel function of second kind.

$h_n^{(2)}(x) = (\frac{\pi}{2x})^{1/2} H_{n+1/2}^{(2)}(x)$ = spherical Hankel function of second kind.

I_M = maximum current distribution occuring at center of the halfwave dipole.

$J_n(x)$ = Bessel function of second kind.

$j_n(x) = (\frac{\pi}{2x})^{1/2} J_{n+1/2}(x)$ = spherical Bessel function of second kind.

J_s = surface current distribution.

$k = \omega(\mu_0 e_0)^{1/2}$ = phase constant.

L = length of conducting cylinder.

L, M, N = independent vector solution of offcenter source point for wave equation.

m_0 n_0 = vector components for spherical wave generated form origin.

$P_n(\cos x)$ = Associated Legendre Polynomials.

r = observation point.

r' = source point.

R_M = Fresnel plane wave reflection coefficient.

$R_{\pm}^{V}$, $R_{\pm}^{H}$ = vertically ^{V} and horizontally ^{H} oriented dipole components.

S = radiation pattern of point source.

$U_{\pm}^{R}$, $V_{\pm}^{R}$ = Sommerfeld integral term.

w_i = weighting functions of moment method.

α_j = unknown coefficients for approximated function in moment method.

ϵ_0 = permittivity of free space.

ϵ_r = relative dielectric constant of medium.

λ = free space wavelength.

μ_0 = permeability of free space.

σ = conductivity of medium.

$\eta = (\mu_0 \epsilon_0)^{1/2}$ = intrinsic admittance of medium.

CHAPTER 1

INTRODUCTION

The problem of antenna field computations near dissipative planar interfaces has become more pronounced because of the advancement of terrestrial radar communication systems. With the presence of the earth, the performance of antennas is strongly affected by interactions due to obstacles and by surface wave propagation. A significant part of the radiated power from the antenna is absorbed by the lossy ground. As a result, the field along the interface decreases faster than in free space, for which they decay proportionally to $1/R$.

An electromagnetic field generated by an active conducting element or reflected from a passive radiating structure over an imperfect conducting ground is much more complex than it would be without the interface. They are represented in terms of integrals that involve current density distributions. The kernels of these integrals decay rapidly in free space, or in the presence of a perfectly conducting earth in which case the image principle can be applied. Consequently, the solution for the fields, generally does not present numerical difficulties. On the other hand, when an imperfectly conducting (lossy) ground is present, the resulting effects are taken into account by modifying the kernel of these integrals, which become much more difficult to evaluate.

In the past, much effort was devoted to the reduction of these complicated integrals to practical closed-form equations [10]. With the development of large digital computers, evaluations based on the exact integral representations have become more feasible. For instance, recently developed methods allow the evaluation of these integrals with complex kernels with high accuracy, but at the price of large computation

time [12]. On the other hand, approximate methods [11], which avoid the evaluation of these integrals, yield less accurate solutions but in a much faster way.

1.1 Motivation

In practical environments, the presence of various structures, such as shelters, barracks, etc, above the ground affects the electromagnetic field distribution. The theory which accounts for the different effects in a real field condition is rather involved. For instance, if one considers the design of a mobile surveillance systems, earth constitutive parameters as well as the position and geometry of surrounding structures, may vary from place to place. Thus, in order to predict the performance of the antenna of such surveillance systems, computer simulations, including the effects brought by shelters, barracks, trucks located on a lossy ground earth, are needed.

In this thesis, a numerical method based on electric and magnetic integral equation formulation and in conjunction with the method of moments is used to optimize the performance of a simple two-wire antenna configurationwhich is part of a system that should detect intruders, with a minimum of false alarms, within a range of 100 meters, (around 10 λ with an operating frequency of 60 MHz), in any direction. This characteristic is referred as hemispherical dome coverage. In addition, since the system is required to be mobile, the antenna performance should not vary significantly with environmental changes, such as weather conditions, constitutive parameters of the earth, etc. The project described in this thesis, involves as a first step the theoretical study of the performance of a wire antenna configuration of a system, which can detect the disturbances provoked by intruders, moving from any direction above the ground. This study has practical application for remote site security systems and was carried out in collaboration with a large local company involved in electronic system design and manufacturing.

The theoretical model which is used to design such configuration, has some limitations. Indeed, the presence of structures such as trucks and barracks increase the size of the problem. For instance, the modeling of an airplane is a even more involved procedure because the complexity of contours and geometries requires a lot of sub-elements for numerical computations.

In order to verify the theoretical solution, a full-scale site antenna test is not possible because of the limitation imposed by fixed physical structures and subjected to environmental noise. A less costly alternative is the use of an anechoic chamber, since indoor testing provides better control of the experimental conditions. However, due to the physical size of the system to be tested, experiments done in the anechoic chamber must be performed with scaled down models. For this type of application, very near scattered field measurement should be performed. A structure which has certain electromagnetic properties at a given frequency f, will develop a similar field distribution at frequency nf, provided that all linear dimensions are multiplied by the ratio $1/n$ and the complex permittivity by n [1]. In addition, scaled models allow the mapping of the electric field everywhere in the zone of interest, in the presence of complex structures, in order to detect regions where the field level is too low. This experimental study is carried out by other researchers of the Laboratory for Electromagnetics and Microwaves.

In order to test the performance of scaled down models in the anechoic chamber, a near scattered field measurement was first performed and compared with the results given by the numerical technique used for field computations. A closer study of the near field scattering by a metal barrack in the presence of ground and its affect on field distribution was needed. The situation that was chosen for study and comparison was a conducting hemisphere located on a perfectly conducting ground. The conducting hemisphere was placed in the far field of a monopole antenna, also located on the perfect ground. The near scattered field of the hemisphere was measured and

computed. It turned out that the numerical analysis yielded some oscillatory solutions that were not confirmed by the measurements. This situation created a need to verify the result by a closed form analytical solution.

There has been much investigation on the scattering by a sphere. Stratton [2] pioneered the development of spherical modes for the case of plane wave irradiations. He used the plane wave, whose electric vector is linearly polarized in one of the orthogonal axes, in order to approximate a source at large distance. This approach could be applied to most far field scattering problems. However, no solution on the near-field scattering of a conducting sphere irradiated by a dipole is available, especially when the size of the sphere is such that plane wave irradiation cannot be assumed. Most probably, the solution to this more general problem has not received much attention in the past, because the interest of researchers has concentrated on the far scattered field (e.g. radar cross-section). As a second step, a new proposed analytical solution based on spherical eigenmode expansions to approximate spherical irradiation by a dipole source is presented. Analytical results represent a significant contribution to this thesis, since the solution is completely original.

1.2 State of the art

The first investigation on the problem of a dipole in the presence of an imperfectly conducting plane was published by A. Sommerfeld [3]. It cannot be solved in a closed form, but the fields can be expressed in terms of integrals, called Sommerfeld integrals. A large amount of work has been dedicated to this subject since then. The computation time associated with evaluating the integrals is quite inefficient because the kernels are highly oscillatory. Alternately, an approximation is used to replace the Sommerfeld integrals [4][5][6]. Because of their approximate nature, the range of applications that would yield accurate solutions is rather restricted. Image principles have also been applied to approximate the solution. Lindell and Alanen [7][8][9] used

an exact image theory to evaluate this kind of problem. The image of a point source was interpreted as a line source that extends to infinity in a complex space, since the distance from the image to the point at which the field is computed is a complex number. Similarly, a dipole image located at a complex depth was introduced by Wait [10].

Miller *et al.* [11],[12] developed a procedure which utilizes a numerical algorithm for evaluating the exact Sommerfeld integrals for a given set of ground parameters, with slight modification to the integrals in order to avoid difficulties inherent to the oscillatory nature of the kernels. The subsequent evaluations employed an interpolation method in order to minimize the computation time. The same authors used Fresnel plane-wave reflection coefficients to approximate the solution in situations where radiating structures are not located near the ground.

The backbone of all the theoretical methods mentioned above remains the same: they use a modified Green's function to replace the free space Green's function in the integral equation formulation to account for the presence of a lossy ground plane. Among all methods that were used to evaluated the radiating structures with the presence of an imperfectly conducting plane, the classical Sommerfeld integral method still remains the most accurate approach for analyzing this kind of problem. However, the computation for the integrals is quite time consuming. Other alternatives, such as complex image theory, seem to be more appealing in terms of computation time. Also, the Fresnel reflection coefficients can provide a solution even more quickly, but with less accuracy. The latter method is very useful for a rapid evaluation of fields, such as needed for the design and optimization of antenna systems. The Sommerfeld procedures developed by Miller *et al.* yield accurate solutions with a minimal increase in computer time. The Numerical Electromagnetic Code (NEC), used for the simulations in this work, utilizes this approach.

CHAPTER 2

THEORY OF NUMERICAL METHODS

Closed form solutions found by spherical-wave expansions are generally limited to idealized cases, such as a conducting sphere discussed in Chapter 5. However, it is possible to obtain the solution of problems involving general structures and forms of antennas by numerical means. The numerical method used to analyze most antenna problems is built around the numerical solution of integral equations written in terms of currents induced on conducting structures by external fields and/or active sources. The integral formulation, which utilizes both electric field and magnetic field integral equations, was derived by Pocklington, for wire scatterers and surface antennas [36]. It turns out that the electric field integral equation is best suited for the case of thin-wire structures of small or vanishing conductor volume. On the other hand, the magnetic field integral equation gives good results on voluminous structures with large smooth surfaces [11]. The integral solutions are then solved numerically by the method of moments [13],[14].

When an antenna system is affected by a ground plane, the free-space integral equation formulation is altered by the lossy ground plane in three ways:

1) modification of the current distribution through near-field interaction
2) change of the fields illuminating the structures
3) change of the re-radiated fields.

Therefore, when a ground plane is present, the free-space Green's function must be modified to yield a more complex Green's function that accounts for the presence of a ground plane. The solution for the fields developed by current elements in the presence of a ground plane was developed by A. Sommerfeld [3]. While this solution

is used directly in the integral-equation computer program, the oscillatory kernel of the Sommerfeld integrals uses excessive computation time and hence limits its application. In order to maintain a reasonable computation time, the Sommerfeld integrals have been slightly changed to eliminate some singularities and to minimize the oscillations. A lookup table of the Sommerfeld solution is generated by this procedure and interpolation is used to find specific values [11],[12]. When a lossy ground plane is involved and the structures are not too near the ground, the Fresnel plane-wave reflection coefficients can be used to modify the image method in order to obtain the field solution in a faster manner. The solution for a perfectly conducting ground is much simpler since the image method can be applied directly.

2.1 Integral equation formulation

Integral equations of various kinds have been widely used for the analysis of thin-wire antennas and scatterers [12] [16]. The electric field produced by a volume current distribution J, with the time variation $e^{j\omega t}$ understood, can be calculated through the integral expression:

$$\mathbf{E}(\mathbf{r}) = \frac{-j\eta}{4\pi k} \int_V \mathbf{J}(\mathbf{r}) \cdot \mathbf{G}(\mathbf{r},\mathbf{r}')dV' \tag{2.1}$$

where the free-space Green's function is defined by the wave equation:

$$\mathbf{G}(\mathbf{r},\mathbf{r}') = (\nabla^2 + k^2)\mathbf{g}(\mathbf{r},\mathbf{r}')$$

and $\mathbf{g}(\mathbf{r},\mathbf{r}')$ is given as:

$$\mathbf{g}(\mathbf{r},\mathbf{r}') = \frac{e^{-jk|\mathbf{r}-\mathbf{r}'|}}{|\mathbf{r}-\mathbf{r}'|}$$

where $\mathbf{r}'$ is the source point, $\mathbf{r}$ is the variable observation point, $k = \omega\sqrt{\mu_0\epsilon_0}$, and $\eta = \sqrt{\mu_0\epsilon_0}$.

When the current distribution is limited to a perfectly conducting surface, the volume integral of the current distribution can be reduced to a surface integral. Thus (2.1) becomes

$$\mathbf{E}(\mathbf{r}) = \frac{-j\eta}{4\pi k}\int_S \mathbf{J}_s(\mathbf{r})\cdot\mathbf{G}(\mathbf{r},\mathbf{r}')dA' \tag{2.2}$$

with $\mathbf{J}_s$ being the surface current density. The observation point $\mathbf{r}$ is restricted to be off the surface S, so that $\mathbf{r} \neq \mathbf{r}'$, since the integrand $\mathbf{g}(\mathbf{r},\mathbf{r}')$ is unbounded otherwise. An integral equation for the current induced on S by an incident electric field $\mathbf{E}_{inc}$ can be obtained by imposing the boundary condition on the surface S.

$$\mathbf{n}(\mathbf{r}) \times [\mathbf{E}_{inc}(\mathbf{r}) + \mathbf{E}_{scat}(\mathbf{r})] = 0$$

where $\mathbf{n}(\mathbf{r})$ is the unit normal vector of the surface at $\mathbf{r}$ and $\mathbf{E}_{scat}$ is the secondary field due to the induced surface current $\mathbf{J}_s$ by the primary field $\mathbf{E}_{inc}$. Using (2.2) and the boundary condition on S yields the desired integral equation:

$$-\mathbf{n}(\mathbf{r}) \times \mathbf{E}_{inc}(\mathbf{r}) = \frac{-j\eta}{4\pi k}\mathbf{n}(\mathbf{r}) \times \int_S \mathbf{J}_s(\mathbf{r}')\cdot(\nabla^2 + k^2)\mathbf{g}(\mathbf{r},\mathbf{r}')dA'. \tag{2.3}$$

When the wire radius a is much less than the wavelength λ and the wire length L, (i.e. $a \ll \lambda$ and $a \ll L$), this vector integral equation can be reduced to a scalar integral equation by using the thin wire approximation, for which the following assumptions can be made:

1) transverse currents can be neglected relative to axial currents on the wire.
2) volume circumferential variation in the axial current can be neglected.
3) currents can be represented by thin filaments on the wire axis.
4) boundary conditions for the electric field need be enforced in the axial direction only.

Consequently, the surface current can then be represented by a current filament $I(s)\mathrm{s} = 2\pi a\mathbf{J}_s(\mathbf{r})$ (see Fig 2.1) , and (2.3) becomes the integral over the length of the wire

$$-\mathbf{n}(\mathbf{r}) \times \mathbf{E}_{inc}(\mathbf{r}) = \frac{-j\eta}{4\pi k}\mathbf{n}(\mathbf{r}) \times \int_L I(s')(k^2\mathrm{s} - \nabla\frac{\partial}{\partial s'})\mathbf{g}(\mathbf{r},\mathbf{r}')ds', \tag{2.4}$$

which is subsequently reduced to the scalar equation

$$-\mathbf{s}\cdot\mathbf{E}_{inc}(\mathbf{r}) = \frac{-j\eta}{4\pi k}\int_L I(s')(k^2\mathbf{s}\cdot\mathbf{s}' - \frac{\partial^2}{\partial s\partial s'})g(r,r')ds'. \tag{2.5}$$

Since $\mathbf{r}'$ is now the point at s' on the wire axis while $\mathbf{r}$ is a point at s on the wire surface $|\mathbf{r}-\mathbf{r}'| \geq a$ and the integrand is bounded.

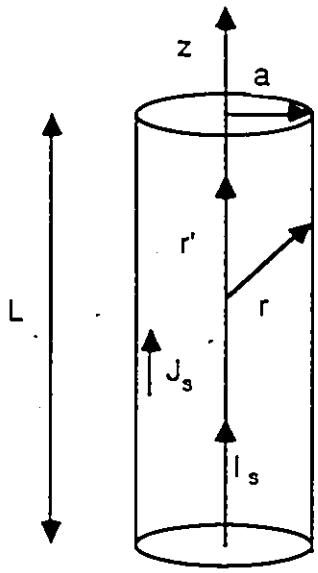

short wire element

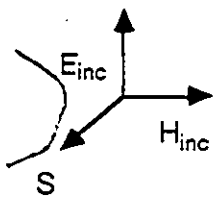

incident field

Fig. 2.1 Current filament and its parameters.

$\mathbf{J}_s$ is the surface current distribution, I_s is the current filament at the axis of the wire, $\mathbf{r}'$ is the distance from the center of the current filament to the source point, $\mathbf{r}$ is the distance to the observation on the wire surface, a is the radius of the wire, and L is the length of the wire element.

The magnetic field integral equation is derived similarly by using the surface current distribution $\mathbf{J}_s$, as

$$\mathbf{H}_{scat}(\mathbf{r}) = \frac{1}{4\pi}\int_S \mathbf{J}_s(\mathbf{r}')\times\nabla' g(\mathbf{r},\mathbf{r}')dA' \tag{2.6}$$

If the current $\mathbf{J}_s$ is induced by an external incident field $\mathbf{H}_{inc}$, then the total magnetic field inside the perfectly conducting surface must be zero. Hence, for $\mathbf{r}$ just inside the

surface S,

$$\mathbf{H}_{inc}(\mathbf{r}) + \mathbf{H}_{scat}(\mathbf{r}) = 0.$$

The integral equation for $\mathbf{J}_s$ can be found by letting $\mathbf{r}$ approach the surface point $\mathbf{r}_0$ from inside the surface along the normal $\mathbf{n}(\mathbf{r}_0)$, hence

$$-\mathbf{n}(\mathbf{r}_0) \times \mathbf{H}_{inc}(\mathbf{r}_0) = \mathbf{n}(\mathbf{r}_0) \times \frac{1}{4\pi} \lim_{r \to r_0} \int_S \mathbf{J}_s(\mathbf{r}') \times \nabla' g(\mathbf{r}, \mathbf{r}') dA', \tag{2.7}$$

where $\mathbf{n}(\mathbf{r}_0)$ is the normal vector at $\mathbf{r}_0$ directed outward. The limit can be evaluated by using the potential theory to yield the desired integral equation [11],

$$-\mathbf{n}(\mathbf{r}_0) \times \mathbf{H}_{inc}(\mathbf{r}_0) = -\frac{1}{2}\mathbf{J}_s(\mathbf{r}_0) + \frac{1}{4\pi} \int_S \mathbf{n}(\mathbf{r}_0) \times [\mathbf{J}_s(\mathbf{r}') \times \nabla' g(\mathbf{r}, \mathbf{r}')] dA'. \tag{2.8}$$

2.2 Numerical solution by method of moments

The method of moments [13] [14] [15] is one of the most important methods for solving electromagnetic field problems and can be applied to both deterministic and eigenvalue problems. In the following discussion only the deterministic problem is considered. It can be formulated with the inhomogeneous equation

$$Lf = y \tag{2.9}$$

where L is a linear operator, f is the unknown function to be determined, and y is the input or excitation. The unknown function f can be expressed in terms of basis or expansion functions f_j which are in the domain of L

$$f = \sum_N \alpha_j f_j \tag{2.10}$$

Generally, the f_j's form a set of known orthogonal functions and should fulfill the associated boundary conditions The α_j's are the unknown coefficients to be determined. The set of basis functions can be finite or infinite. However, in practical

situations, the summation has to be truncated. Consequently, the solution will be an approximation of the exact solution.

Since L is a linear operator, (2.9) can be written as

$$\sum_N \alpha_j L f_j = y \tag{2.11}$$

Consider the inner product in the function space

$$< u, v >= \int_\Omega u v^* d\Omega,$$

where Ω is the domain of the functions. It can be conceptually seen as a projection u in the direction of v. Choosing a set of weighting functions $\{w_i\}$ defined in the range of the operator L, a set of equations for determining the coefficients α_j can be obtained by taking the inner product of equation (2.11) with each component of $\{w_i\}$. The original functional equation thus becomes a set of linear equations which is written in the matrix form:

$$[M]\alpha = \mathbf{y}$$

where

$$\begin{aligned} M_{ij} &=< w_i, L f_j > \\ y_i &=< w_i, y > \end{aligned} \tag{2.12}$$

and $\alpha = [\alpha_1, \alpha_2, \alpha_3, \cdots, \alpha_j \cdots]^T$, in which ^{T} is the transpose of a matrix. If the matrix $[M]$ is regular, then $[M]^{-1}$ exists, the $\alpha_j's$ are given by $\alpha = [M]^{-1}\mathbf{y}$, and the solution is found by using (2.10). Let $R(L)$ be the range of the operator L. The right-hand side of (2.12) is the orthogonal projection of the subspace of $R(L)$ spanned by the operation of L on the exact solution f, i.e. $\mathbf{y}$, onto the subspace W spanned by $\{w_i\}$. The left-hand side of (2.12) is the projection of the subspace spanned by the operation of L on the f_j's onto W. The moment method equates these two projections (see Fig. 2.2). Since the error, also called weighted residual, is orthogonal to the projection, it is of the second order and, consequently, the method is an error minimization procedure.

There are many possible choices of the weighting functions $\{w_i\}$ and basis functions $\{f_j\}$. The selections of the $\{w_i\}$ lead to the different specializations of the moment method. Some of them give faster convergence, while others give matrices easier to evaluate [15]. When $w_i = f_i$, the procedure is called Galerkin's method, which has been found to yield accurate results with rapid convergence. Sometimes, however, the inner product

$$M_{ij} = \int_\Omega w_i L f_j d\Omega \tag{2.13}$$

is difficult to evaluate. One way to sidestep this inconvenience is to require that (2.11) be satisfied at discrete points in the region of interest, generally where boundary conditions must be met. This is a point matching of the integral equation which is the collocation or point matching method.

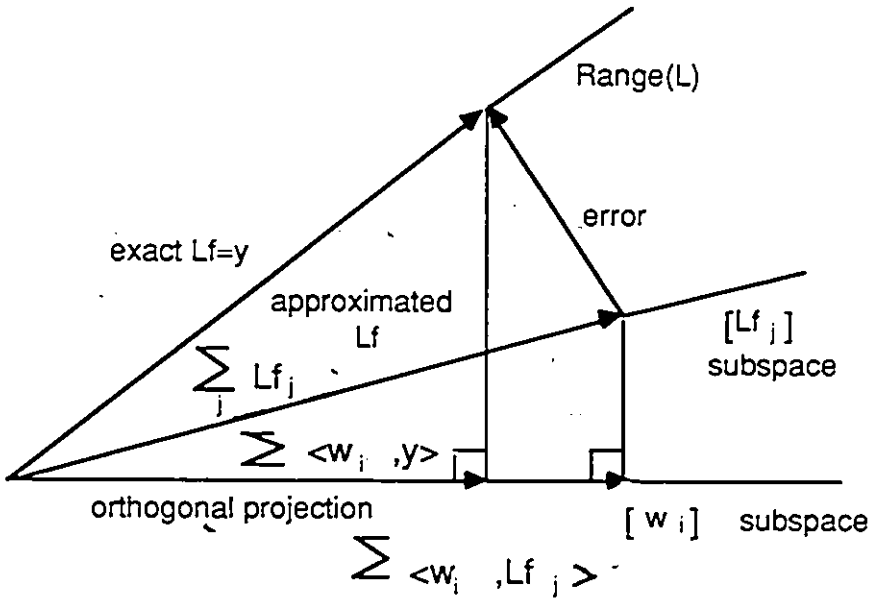

Fig. 2.2 Illustration of the moment method [14].

The method of moments equates the orthogonal projection of both the approximated solution and the exact solution onto the subspace spanned by the weighting function.

This is the approach that is used to solve the present problem: if $\{w_i\}$ is chosen to be a set of Dirac functions $w_i(r) = \delta(r - r_i)$, with $\{r_i\}$ a set of points on the conducting surface, the elements of the matrix $[M]$ and the vector y hence become

$$M_{ij} = Lf_j|_{r=r_i}$$

$$y_i = f_j(r_i)$$

which is equivalent to enforcing (2.11) at discrete points. Collocation is generally less accurate than Galerkin's method, but the inner products involved in the matrix elements are computed in a trivial manner.

Generally, the expansion functions are defined over the entire domain of interest. They can also be defined only on subsections of that domain. This further simplifies the evaluation of the matrix elements. For instance, wires are divided into short straight segments with sampling points at their centers while surfaces are approximated by a set of flat patches with sampling points at their centers. The current at the center of each segment is represented by a combination of functions defined on each subsection. For instance, the total current on segment j has the form

$$I_j(s) = A_j + B_j \sin k(s - s_j) + C_j \cos k(s - s_j), \quad |s - s_j| < \Delta_j/2. \tag{2.14}$$

The 3N unknown constants implied in (2.14) are reduced to N unknowns, by an extrapolation procedure which is applicable to single or multiple connected segments [16].

2.3 The Sommerfeld method [12]

The free space integral equation can be extended to handle wires located near the boundary interface by modifying the Green's function so that it includes the fields scattered from the interface. When source points and the observation points are both located above ground ($_+$) or below ground ($_-$) the direct field $\mathbf{E}^D_{\pm}(\mathbf{r})$ from the wire source is given by:

$$\mathbf{E}^D_{\pm}(r) = \int_{C'(\mathbf{r})} I(s')\mathbf{s}' \cdot \mathbf{G}^D(\mathbf{r},\mathbf{r}')ds', \qquad (z \cdot z' \geq 0)$$

where $G^D(r,r')ds'$ is the free space Green's function defined in (2.1).

Given the incident electric field $\mathbf{E}^I_\pm(\mathbf{r})$, and introducing the electric field reflected by the interface $\mathbf{E}^R_\pm(\mathbf{r})$, one can apply the boundary condition for the electric field on the conducting wires:

$$\mathbf{s}\cdot\mathbf{E}^I_\pm(\mathbf{r}) = -\mathbf{s}\cdot\mathbf{E}^D_\pm(\mathbf{r}) - \mathbf{s}\cdot\mathbf{E}^R_\pm(\mathbf{r});\quad \mathbf{r}\in C_\pm(\mathbf{r})$$

where s' and $\mathbf{s}$ are unit vectors tangent to the wire at s and s', $C_\pm(\mathbf{r})$ is the contour of an arbitrary antenna surface and the field component produced by the interface is

$$\mathbf{E}^R_\pm(\mathbf{r}) = \int_{C_\pm(\mathbf{r})} I_\pm(s')\mathbf{s}'\cdot\mathbf{G}^R_\pm(\mathbf{r},\mathbf{r}')ds' \tag{2.15}$$

with

$$\begin{aligned}\mathbf{G}^R_\pm(\mathbf{r},\mathbf{r}') &= \frac{k_\pm^2 - k_\pm^2}{k_+^2 + k_-^2}\mathbf{G}^I_\pm(\mathbf{r},\mathbf{r}') + \mathbf{R}_\pm(\mathbf{r},\mathbf{r}')\\ \mathbf{G}^I_\pm(\mathbf{r},\mathbf{r}') &= -\mathbf{I}_R\cdot\mathbf{G}^D_\pm(\mathbf{r},\mathbf{I}_R\cdot\mathbf{r}'),\quad \mathbf{I}_R = x\mathbf{x}+y\mathbf{y}+z\mathbf{z}\end{aligned} \tag{2.16}$$

The additional term $R_\pm$ of the reflected Green's function involves the Sommerfeld integrals and is constructed from the following components for horizontally ^{H} and vertically ^{V} oriented dipoles, with cylindrical coordinates (r,ρ,z):

$$\begin{aligned}R^V_{\pm\rho} &= \frac{C_1}{k_\pm^2}\frac{\delta^2}{\delta\rho\delta z}k_\pm^2 V^R_\pm\\ R^V_{\pm z} &= \frac{C_1}{k_\pm^2}\left(\frac{\delta^2}{\delta z^2}+k_\pm^2\right)k_\mp^2 V^R_\pm\\ R^H_{\pm\rho} &= \frac{C_1}{k_\pm^2}\cos\phi\left(\frac{\delta^2}{\delta\rho^2}k_\pm^2 V^R_\pm + k_\pm^2 U^R_\pm\right)\\ R^H_{\pm\phi} &= \frac{-C_1}{k_\pm^2}\sin\phi\left(\frac{1}{\rho}\frac{\delta}{\delta\rho}k_\pm^2 V^R_\pm + k_\pm^2 U^R_\pm\right)\\ R^H_{\pm z} &= -\cos\phi R^V_{\pm\rho}\end{aligned} \tag{2.17}$$

where the source is at $\mathbf{r}' = z'\mathbf{z}$ and the field is evaluated at $\mathbf{r} = \rho(\cos\phi\mathbf{x}+\sin\phi\mathbf{y})+z\mathbf{z}$. The V^R, H^R terms are the Sommerfeld integrals [2],[3],[12]. The source points are located on the axis of the wire, and the observation points are located on the surface of the wire with the assumption of the thin wire approximation (see Fig 2.3). The horizontal current element is along the x axis.

The Sommerfeld integral terms are

$$U_{\pm}^{R} = \int_0^{\infty} D_1(\lambda) exp(-\gamma_{\pm}|z+z'|) J_0(\lambda\rho)\lambda d\lambda$$
$$V_{\pm}^{R} = \int_0^{\infty} D_2(\lambda) exp(-\gamma_{\pm}|z+z'|) J_0(\lambda\rho)\lambda d\lambda \qquad (2.18)$$

with

$$D_1(\lambda) = \frac{2}{\gamma_+ + \gamma_-} - \frac{2k_{\pm}^2}{\gamma_{\pm}(k_+^2 + k_-^2)}$$
$$D_2(\lambda) = \frac{2}{k_-^2\gamma_+ + k_+^2\gamma_-} - \frac{2}{\gamma_{\pm}(k_+^2 + k_-^2)}$$

and $\gamma_{\pm} = (\lambda^2 - k_{\pm}^2)^{1/2}$. The terms $U_{\pm}^{R}$ and $V_{\pm}^{R}$ differ from those commonly used in the sense that they have static terms subtracted in order to remove the oscillatory nature of the kernels. This allows better accuracy during the interpolation procedure. The term subtracted from $V_{\pm}^{R}$ allows convergence of the integral as ρ and $z + z'$ approach zero with only an R^{-1} singularity in the second derivatives of $V_{\pm}^{R}$. The term subtracted from $U_{\pm}^{R}$ does not alter the singularity but completes the G_I term in equation (2.18). The two-dimensional interpolation method used in the code provides a shorter computation time while maintaining the accuracy obtained by using the Sommerfeld integrals. The interpolation method evaluates the Sommerfeld integrals at a grid of values $(\rho, z + z')$, given a set of ground parameters. Then, the computed values are stored in the form of a lookup table in order to interpolate the values needed subsequently. The time required for evaluating the matrix elements is greatly reduced by this method.

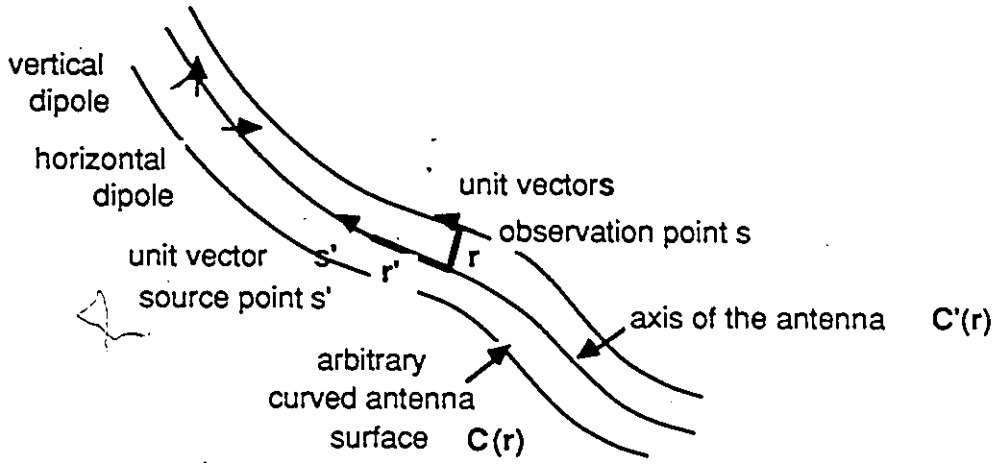

Fig. 2.3 Arbitrary curved antenna surface $C_{\pm}(\mathbf{r})$.

The arbitrary antenna is divided into small vertical and horizontal dipoles. The total field is the field produced by a combination of these dipoles.

2.4 The Reflection coefficient method [11] [12]

This method employs the plane wave reflection and image theory in order to simplify the evaluation of the fields produced by structures above an imperfect ground. The free space kernel g_0 is modified by adding an image kernel term g_{sg}. This additional term g_{sg} is called the reflection coefficient Green's function for the lossy ground. It includes g_i, the image Green's function obtained from the image theory, multiplied by the Fresnel plane wave reflection coefficient. For example, in the case of a vertically oriented dipole, the Green's function is

$$g \simeq g_{sg} = g_0 + R_M g_i \tag{2.19}$$

where R_M is the Fresnel plane wave reflection coefficient for the transverse magnetic (TM) polarization and is given by:

$$R_M = \frac{\epsilon_E \cos\theta - (\epsilon_E - \sin^2\theta)^{1/2}}{\epsilon_E \cos\theta + (\epsilon_E - \sin^2\theta)^{1/2}} \tag{2.20}$$

where ϵ_E is the relative complex permittivity of the ground, and θ is the angle between the ray connecting the source point with observation point and the normal

of the interface (see Fig 2.4). This is similar to the case of a plane wave incident on a semi-infinite plane medium. This method is valid for large distances between the source points and observation points. It takes much less computation time than the Sommerfeld integral method, while providing results which agree within 10%.

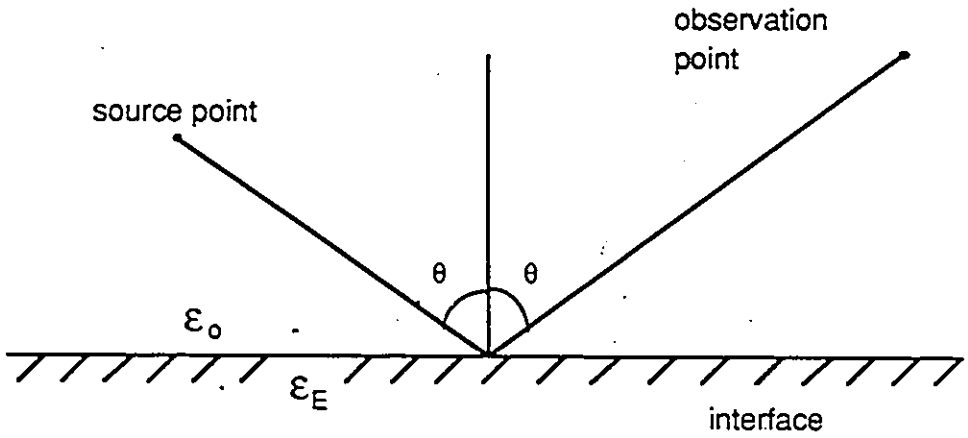

Fig. 2.4 Illustration of the Fresnel reflection coefficient method.

CHAPTER 3

NUMERICAL COMPUTATIONS

3.1 Introduction

In recent years, the use of leaky cables has become increasingly important for the detection of obstacles along some defined path. For instance, the surveillance of installations that must be held secure is a typical application of their use. Such detection systems, called guided radar [38], are presently in the operating stage. They can detect intruders or moving objects approaching or crossing a defined perimeter. However, targets moving at certain altitude above the cables cannot be detected by such systems. Consequently, there emerged the need to develop a volumetric detection system (3-dimensional electronic fence), that would allow surveillance over a hemisphere covering the region of interest. In addition, in the scope of mobile surveillance systems for military launching sites or high security mobile stations, leaky cables are not practical, since they generally have to be buried.

In order to test the performance of a volumetric system, one could build it full scale. Unfortunately, this precludes a study of the effects casued by fixed structures and modified ground constitutive parameters at reasonable cost. An alternate approach is to use scaled down models and test them in an anechoic chamber. However, low conductivities are difficult to achieve with synthesized substances. Computer simulations provide a low cost alternative to evaluate and optimize performance of an antenna system in realistic conditions, including the change of electromagnetic properties of the ground, the location of fixed structures and moving intruders.

3.2 Antenna system

The requirements for the antenna configuration, stress its mobility and the simplicity of design for easy integration in the surveillance system and its compatibility with existing systems (i.e. leaky cable). The simplest antenna that would give almost a perfect volumetric coverage is a single dipole, which has a zero radiation pattern in the direction of its axis. Thus, it could provide a volumetric dome coverage except that it has an asymmetrical radiation pattern along its axis. In addition, in the presence of a ground plane, the radiation pattern may have a zero at grazing angles unless the ground has infinite conductivity. The radiation pattern depends also on the ground parameters. These may vary from one location to another, a range of $\epsilon_r = [2.0, 30.0]$ and $\sigma = [0.001, 0.1]$ S/m were suggested by the company. Lower conductivities of the ground may degrade the antenna performance by affecting the desired coverage, and field distribution especially at grazing angles.

In order to provide good isolation between outgoing and incoming signals, a configuration with two wire-antennas of length $\lambda/2$ is selected comprised of an active antenna and a detecting antenna. A single frequency signal is sent by the active antenna. Any fluctuation of the signal at the terminals of the detecting antenna can be interpreted as the presence of a possible intruder in the detection zone. The two simple antenna dipoles can be arranged either both vertically polarized, horizontally polarized or perpendicular to each other.

3.3 Equivalent human model

Computer simulations should include the presence of human intruders as well as small animals, which are the main cause of false alarms. The introduction of such complex inhomogeneous structures into the numerical computation model is difficult. In order to obtain the result within, at least, an order of magnitude with the use of

the existing software. An approximate approach is to substitute simple mathematical models such as conducting cylinders, with equivalent radar cross-sections as human body. It is important to note that the use of equivalent conducting cylinders is a very crude approximation to this complex problem. In order to create false alarm scenarios, equivalent models of small animals are also used. Thus, computer simulations allow one, first, to determine the signal level above which an alarm state should be triggered, then to verify whether the signal produced by a human intruder versus animal can be extracted without requiring overly complex signal processing.

The radar cross section of a man was measured by F.V. Schultz *et al* [19]. The human subject under test was 200 pounds and six feet tall. Their measurement were performed at five different frequencies. In order to be introduced in the simulations, the human model was converted into an equivalent perfectly conducting cylinder in terms of equivalent radar cross-section. For surveillance systems, the allocated frequency is 60 MHz. Unfortunately, no data on the radar cross section of the human body is available at this particular frequency.

The radar cross section of a perfectly conducting circular cylinder is:

$$\sigma_\tau = \frac{a\lambda}{2\pi}\cos\theta\frac{\sin^2(\frac{2\pi L}{\lambda}\sin\theta)}{\sin^2\theta}. \qquad 3.1$$

where a and L is the radius and length of the cylinder, respectively, and θ is the angle defined by the direction of the incident wave and the axis of the cylinder. The proportion of height and width of a human is $L = 4.5a$. The dimensions of the equivalent cylinder of a human at five different frequencies is shown in table 3.1.

However, if one considers values of Table 3.1, no absorption or resonance, in terms of radar cross-section, occurs at the five available frequencies. In addition, resonances for human body occur only above 1 GHz [20]. Consequently, it is reasonable to extrapolate the radius a at 60 MHz, from the data available below 1 GHz. Thus, after extrapolation, the dimensions are $a = 0.1596$ m and $L = 0.72$ m. A smaller

Table 3.1 Radar cross section of human and its equivalent cylinder.

frequency (in MHz)	human $\sigma(m^2)$ [19]	equivalent conducting cylinder, θ=0, L=4.5a	
		a (in meter)	L (in meter)
410	0.033 2.330	0.0467 0.1929	0.2100 0.8679
1120	0.098 0.997	0.0246 0.0532	0.1105 0.2394
2890	0.140 1.050	0.0107 0.0210	0.0482 0.0944
4800	0.368 1.880	0.0089 0.0153	0.0401 0.0690
9375	0.495 1.220	0.0050 0.0068	0.0227 0.0306

cylinder about one fourth the dimensions of the human equivalent cylinder was used to represent small animals. The smaller dimensions of the conducting cylinder reduce the σ by a factor of 16, as a crude estimate from the size of the small animals. Again, this is a rough approximation of the problem, due to the lack of data on the radar cross section of small animals. Thus, the computation in this simulation can only provide an estimate for such false alarm scenarios. For further insight to the problem, a more elabrate model such as block models for humans should be employed instead.

The arrangement of the two halfwave dipoles which were used in this computation, was an active antenna collinear with the detecting antenna. The spacing relative to wavelength were selected as 2, in order to provide a good isolation [36]. This value was further confirmed by the computations. Any intrusion would modify the voltage level at the detecting antenna. The voltage induced at the receiving antenna by the equivalent cylinder was computed for positions of the target varying from 10 to 50

meters (2 to 10 λ) from the antenna configuration, with 2.5 meters (1/2 λ) steps. This is the required range for mobile surveillance systems.

The difference between the human and the animal equivalent cylinders can be seen in Fig 3.1a to c. The constant voltage received without intruders is plotted as a reference. In Fig 3.1a, the orientation of the cylinder axis coincided with the field vertical polarization of the dipoles. For small animals the induced voltage is obviously not detectable from the reference.

The cylinders were horizontally positioned with respect to the dipoles, in order to simulate crawling intruders. As it is shown in Fig 3.1b, the reception for this orientation is much weaker than the vertical case. This can be explained by the fact that the axis of the cylinders are in the plane which is perpendicular to the polarization of the dipole. However, a difference from 17.5 to 25 meters (3.5 to 5 λ) can be observed.

In order to increase the perturbed signal level produced by the crawling intruders, the detecting antenna which was at the bottom, was changed from vertical orientation to horizontal orientation. The very low level of the detected voltage in this case indicates that this is not an appropriate arrangement for the system (see Fig 3.1c). As a result, this configuration will not be considered for further computer simulations.

3.4 Electric field strength

It is important to have some knowledge about the electric field strength on the perimeter of the site. The field level outside the perimeter and how it decays within the perimeter is part of the specifications required by the manufacturer for defining the size of the perimeter for such an antenna system design. The reason for this is the size of the perimeter should be smaller for lower conductivities in order to receive detectable signal.

In Fig 3.2a, the electric field intensity produced by vertical antenna system is computed. The observation points are located at one meter above ground, at a distance of 75 to 150 meters (15 to 30 λ) form the antenna system. The transmitting antenna was fed with unit voltage. One can observe that the electric field intensity with low conductivity and permittivity values is much lower in magnitude than the one with high values. This shows that the electric field tends to better penetrate a ground with low constitutive parameter values. The strong influence of the ground parameters is also demonstrated in Fig 3.2b, where the observation points are located three meters above the ground. The electric field strength is higher in comparison with the corresponding values for the lower ground parameter values (Fig 3.2a). This is due to the asymmetrical characteristic in azimuth angle of the radiation pattern of the antenna system. This will be discussed more in detail in the next section.

Numerical computations of horizontally polarization, show that the field intensity is reduced by at least one half (Fig 3.3a, and Fig 3.3b). Hence, for the case where the observation points are located one meter above the ground, both curves (representing lower and higher ground parameter values) display a rather low reception level. When the observation points are moved from one to three meters above the ground, the electric field strength shows the same behavior as for the vertically polarized antenna configuration.

3.5 Radiation pattern

It is well known that the presence of the ground not only affects the field strength, but also the field distribution and the radiation pattern. Thus, modification of the ground constitutive parameter values will have some impact on the radiation pattern characteristic of the surveillance system. In addition, in most situations there are fixed structures in the perimeter of interest which may interfere with the electromagnetic produced by the antennas. In order to determine the radiation coverage

performance under these conditions, the radiation patterns of the antenna system in the presence of perfectly conducting structures on the perimeter is required. This simulates the presence of structures such as shelters or launching platform, etc. For the field computations, it is modelled by a rectangular metallic structure with a dimension of $1.2 \times 1.2 \times 6\ \lambda$ (see Fig 3.4 and 3.5). The metallic structure is located at a distance of $6\ \lambda$ away from the antennas. For comparison, radiation patterns of the system with and without the metallic structure are plotted in elevation and azimuth angles. In addition, situations with the upper and lower bounds of the ground constitutive parameter values are considered in the simulations, in order to observe the effects on the radiation coverage performance of the system accounting for the various soil properties that can be enconuntered in real situation. For reasons explained before, only vertically and horizontally polarized antenna configurations will be investigated.

From the characteristics shown in Fig 3.6, 3.7, 3.8, one can see that the radiation patterns are affected by the metallic shelter in several ways. First of all, as expected, it destroys the symmetry of the radiation pattern. In addition, zeros are generated, as compared to the case without structure, especially in the ($\theta = 90^0$, $\phi = [-90^0, 90^0]$ and azimuth planes (see Fig 3.7 and 3.8). The presence of zero radiating pattern degrades the performance of the system, in a sence that any intrusion in these directions can be difficultly detected, likewise, the modification of the ground constitutive parameter values affects the coverage performance, especially when the metallic structure is present (see Fig 3.4b).

For the horizontal dipoles configuration the metallic structure degrades the coverage performance, as in the vertical dipole case. However, the effect is not as pronounced as it can be seen in Fig 3.9, 3.10, 3.11. The symmetry of the radiation pattern of horizontally polarized dipole is in the elevation angle while the vertically polarized dipole is in the azimuth angle. The symmetry in the azimuth plane in the vertically polarized dipoles is distroyed by introducing the metallic structure.

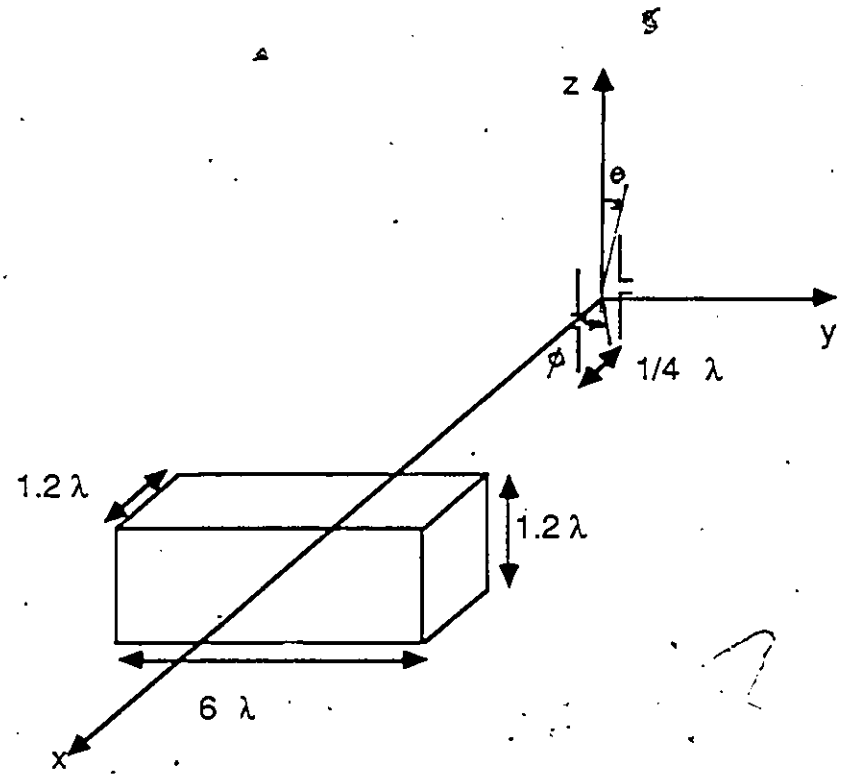

Fig 3.4 Metallic structure with the vertical dipoles configuration.

Table 3.2 shows the complex input impedance of the antenna, with and without the metallic structure. This indicates that the complex impedance of the antenna is affected more in the vertical orientation than the horizontal case. This further confirms that the radiation pattern is more sensitive to the presence of metallic structure in the case of the vertical dipoles configuration than in the horizontal case.

3.6 Conclusion

The advantage of the dipole configuration resides in its simple structures. In addition, it meets the radiation coverage requirements except at grazing angles above the ground. From the numerical computations result, it is found that a metallic structure will enchance the directivity of radiation pattern of the system in the direction of the structure and degrade the desired radiation coverage in other directions. The

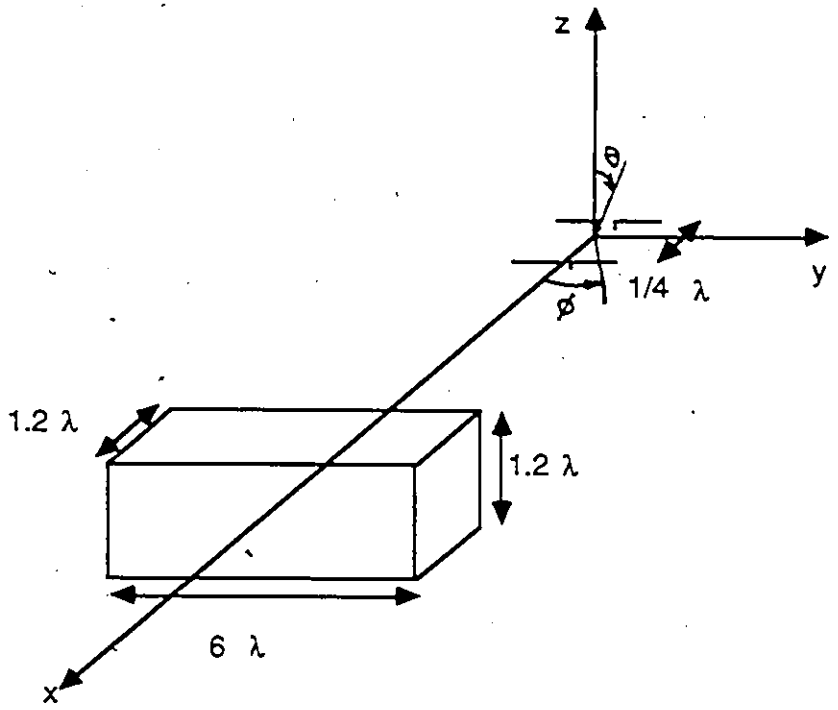

Fig 3.5 Metallic structure with the horizontal dipoles configuration.

Table 3.2 Complex input impedance of dipole antenna configuration.

Bistatic dipole system	distance between dipole	complex input impedance(ohms) ground parameter	
		ε=2.0, σ=0.001	ε=30.0, σ=0.1
vertical	1/4 λ	104.1+j 79.3	108.8+j 72.4
with metallic structure	1/4 λ	106.3+j 79.5	112.7+j 69.0
horizontal	1/4 λ	87.2+j 83.7	51.4+j 96.4
with metallic	1/4 λ	87.4+j 84.0	51.3+j 96.5

degree of degradation depends on the size and location of the structure with respect to the antenna system. In order to further study the near field distribution affected by the metallic structure, a near field scattering of a conducting sphere was investigated. From field computations is is difficult to conclude that the simple antenna arrangement provides suitable coverage for detecting airborne intruders, due to the presence of zero radiation pattern produced by near-by structures. One reaches the same conclusion. For crawling intruders since the presence of the imperfect ground produces zero at grazing angles, complimentary system such as leaky cables should be employed to improve the reception at grazing angle. However, such structures cannot be introduced in the numerical computations simultaneously due to limited computer memory resource.

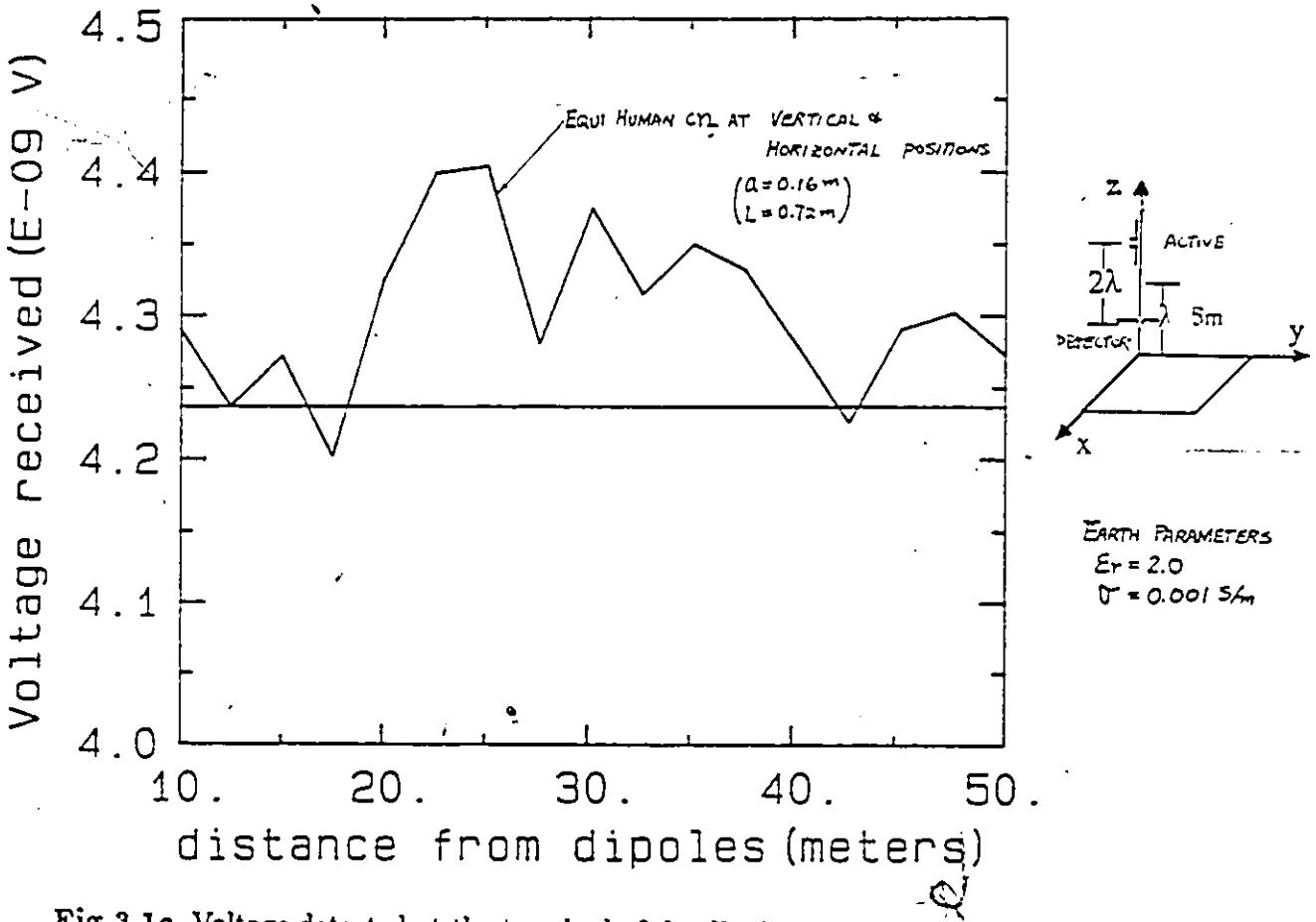

Fig 3.1c Voltage detected at the terminal of the dipole when the two antennas are in orthogonal position.

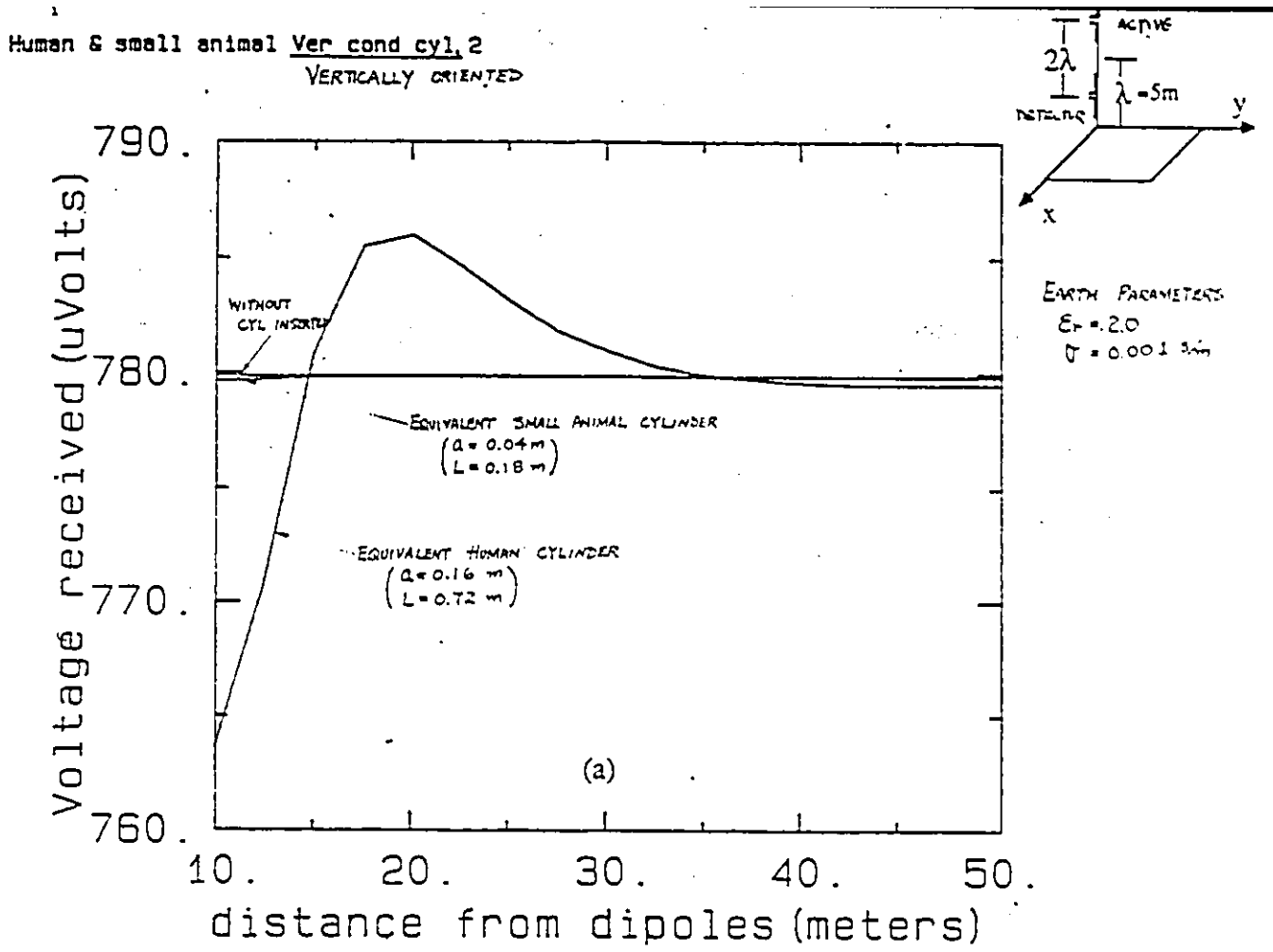

Fig 3.1 Voltage detected at the terminal of the vertical dipole introduced by human intruder and small animals in a) vertical position, b) horizontal position.

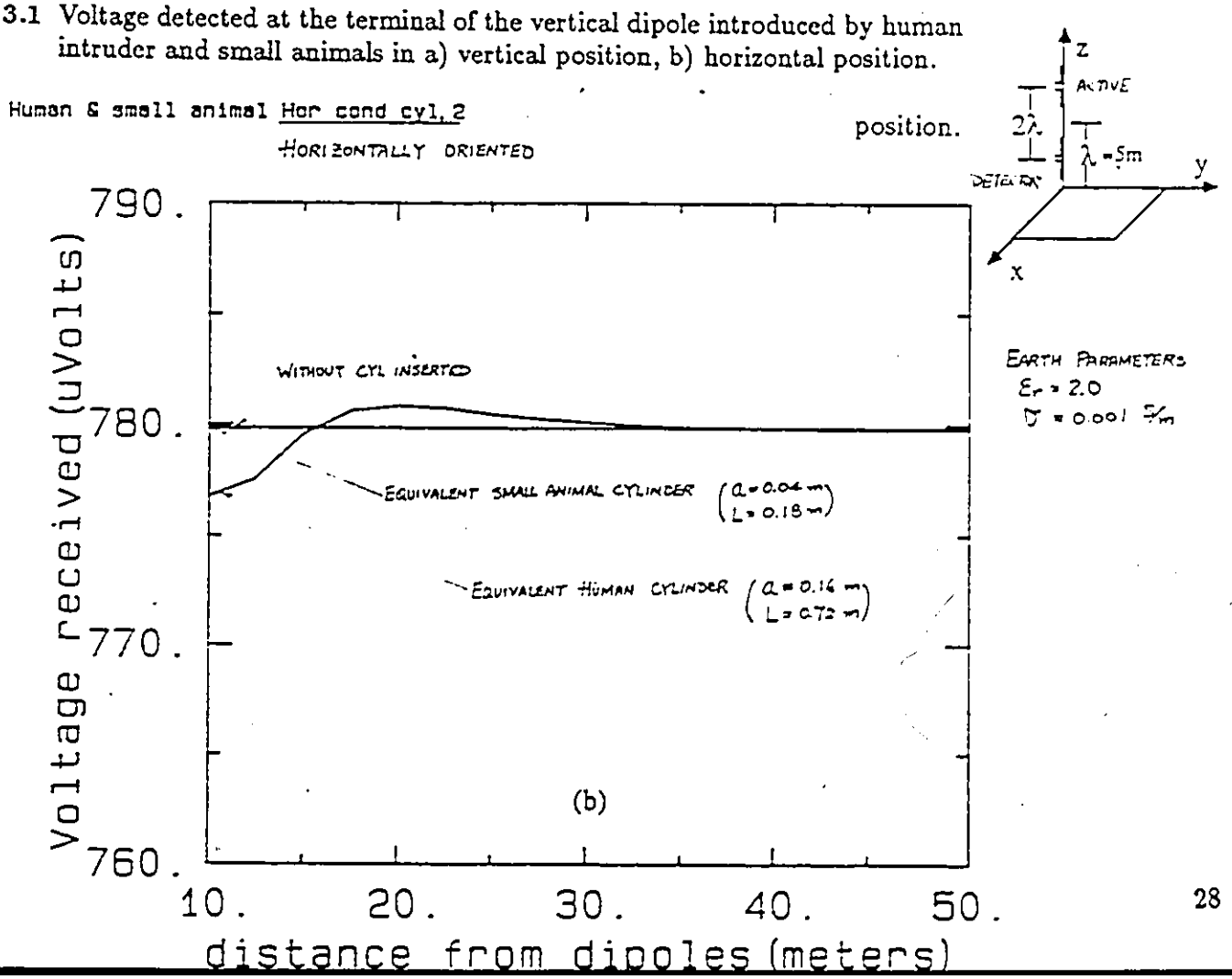

position.

(a)

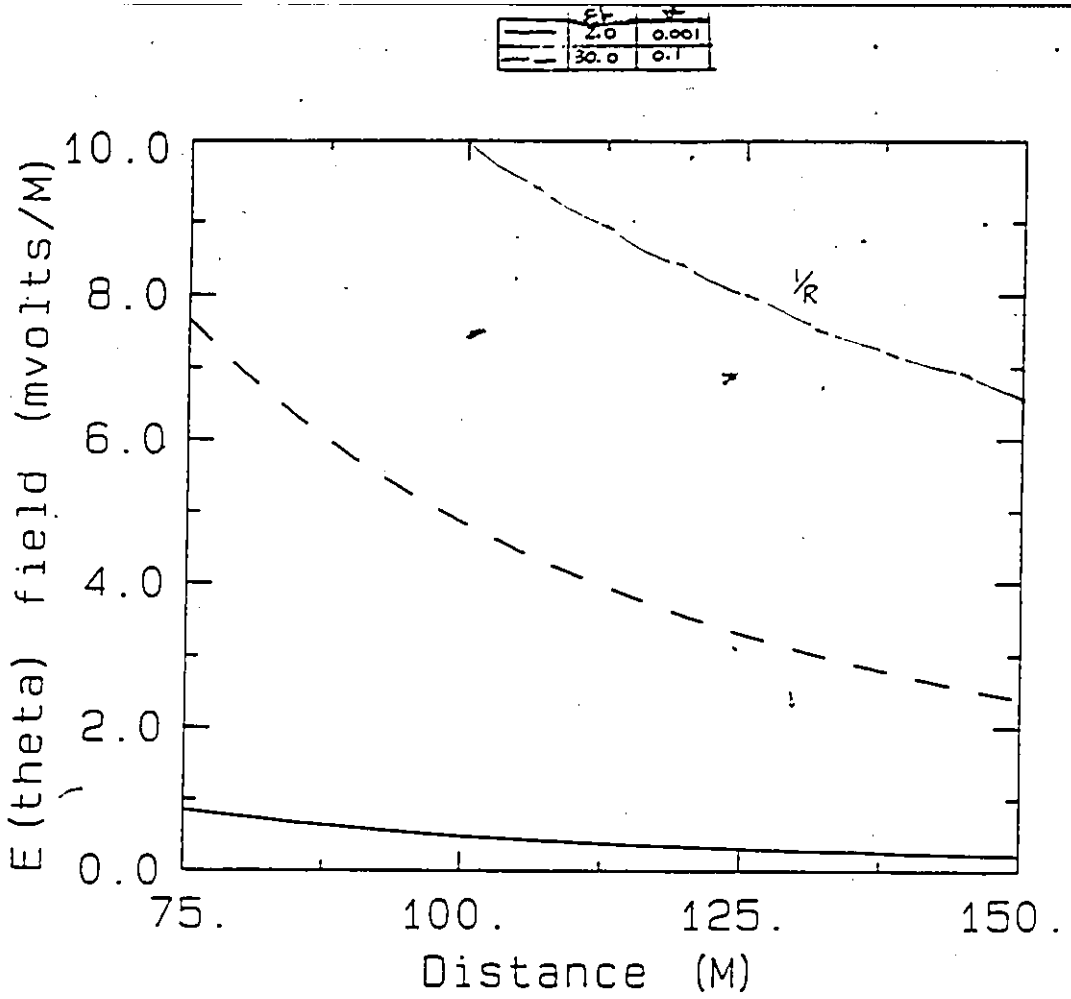

Fig 3.2 Electric field strength affected by ground parameters in vertical dipole.

Observation points are located at a) one meter, b) three meters.

(b)

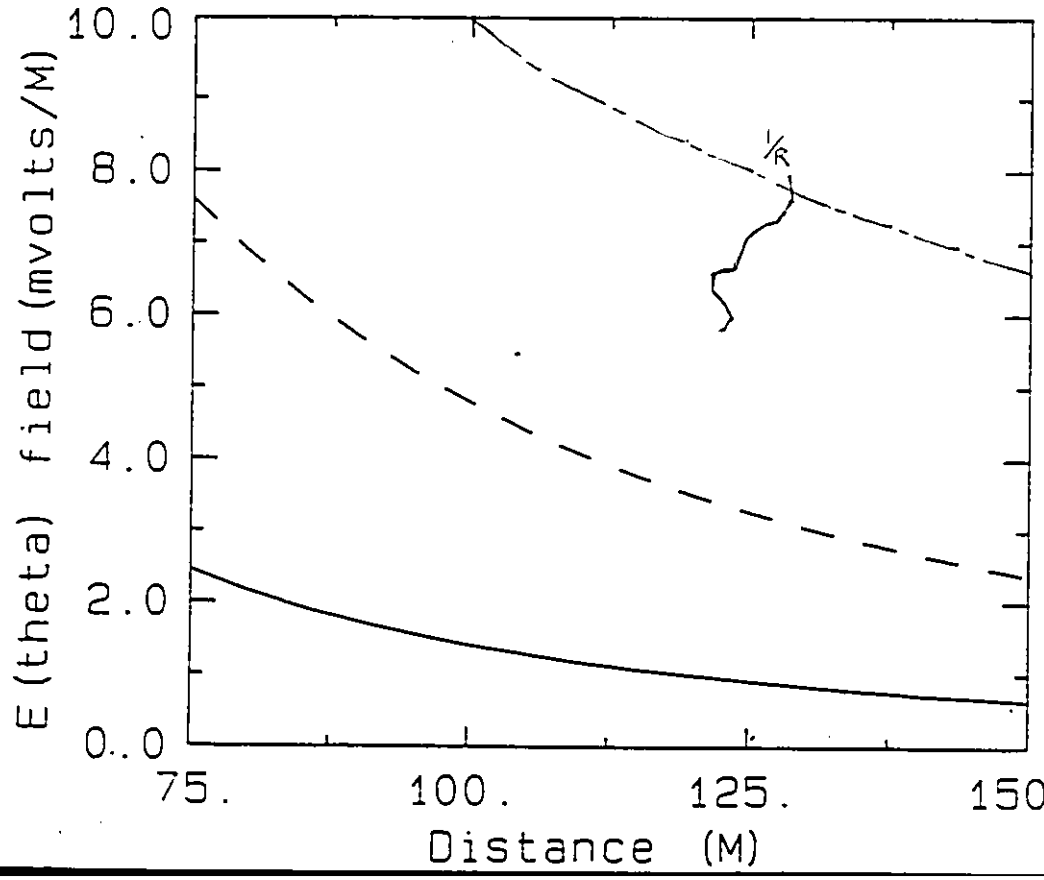

(a)

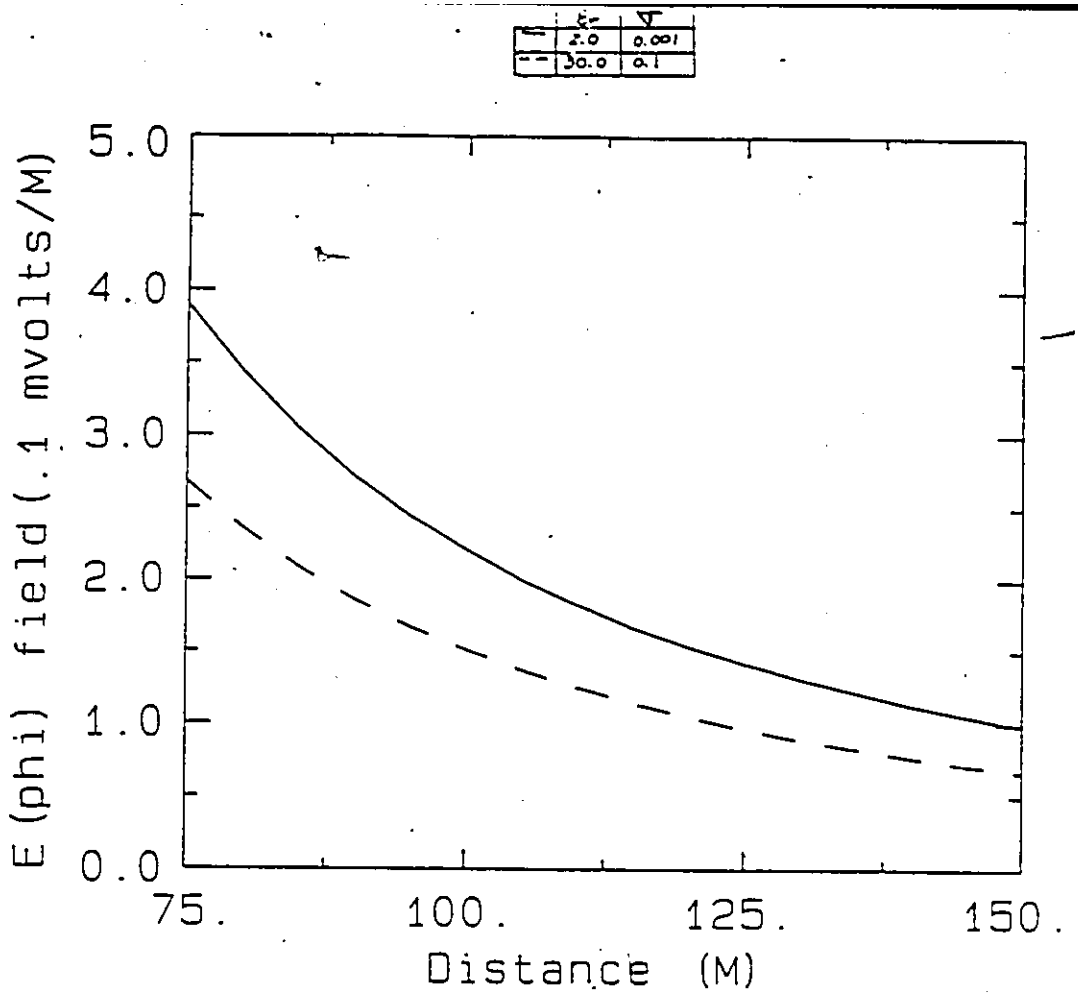

Fig 3.3 Electric field strength affected by ground parameters in horizontal dipole.

Observation points are located at a) one meter, b) three meters.

(b)

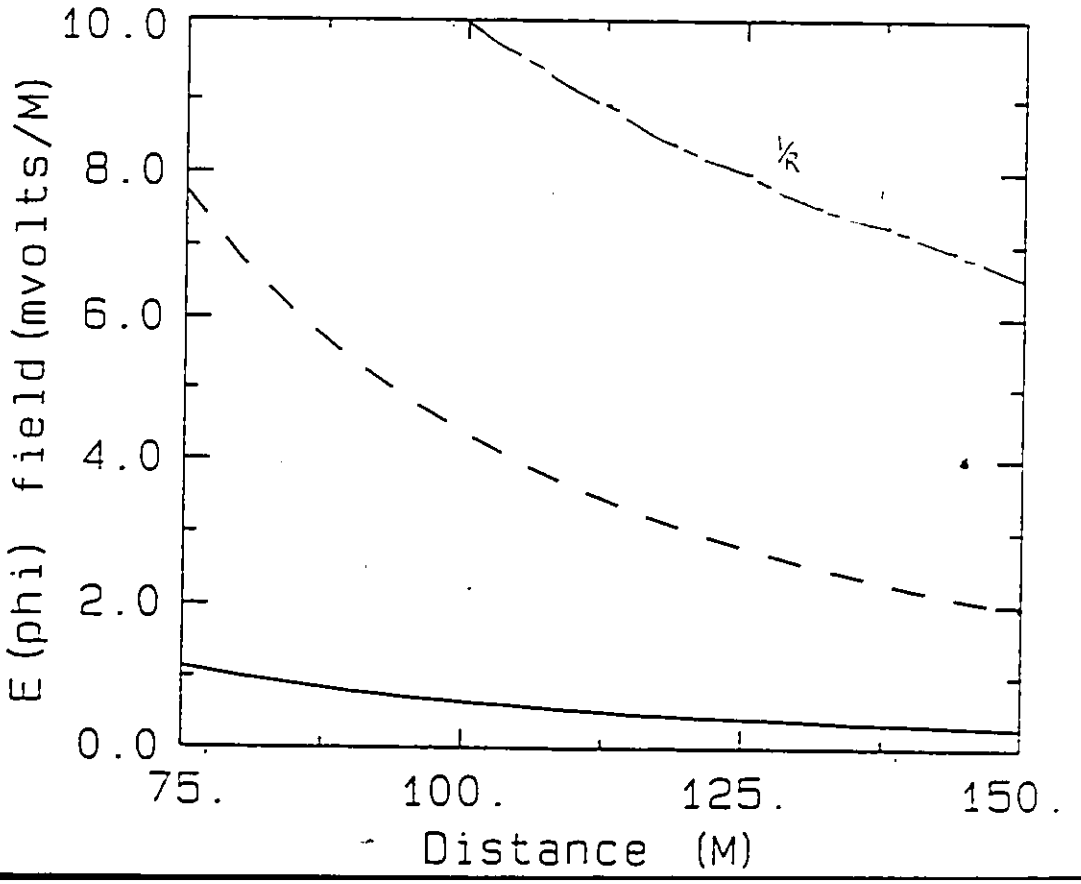

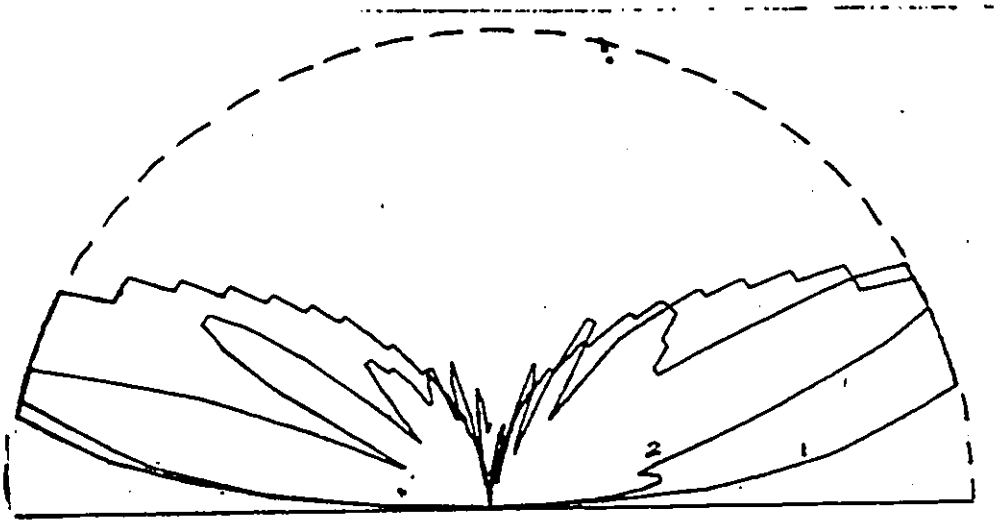

Fig 3.6 The radiation pattern of vertical dipoles configuration for elevation angle $\theta = [-90^0, 90^0]$, $\phi = 0^0$.

It is affected by ground parameters.a) $\epsilon = 2.0$, $\sigma = 0.001$, b) $\epsilon = 30.0$, $\sigma = 0.1$, and by a metallic structure 1)without, 2) with metallic structure.

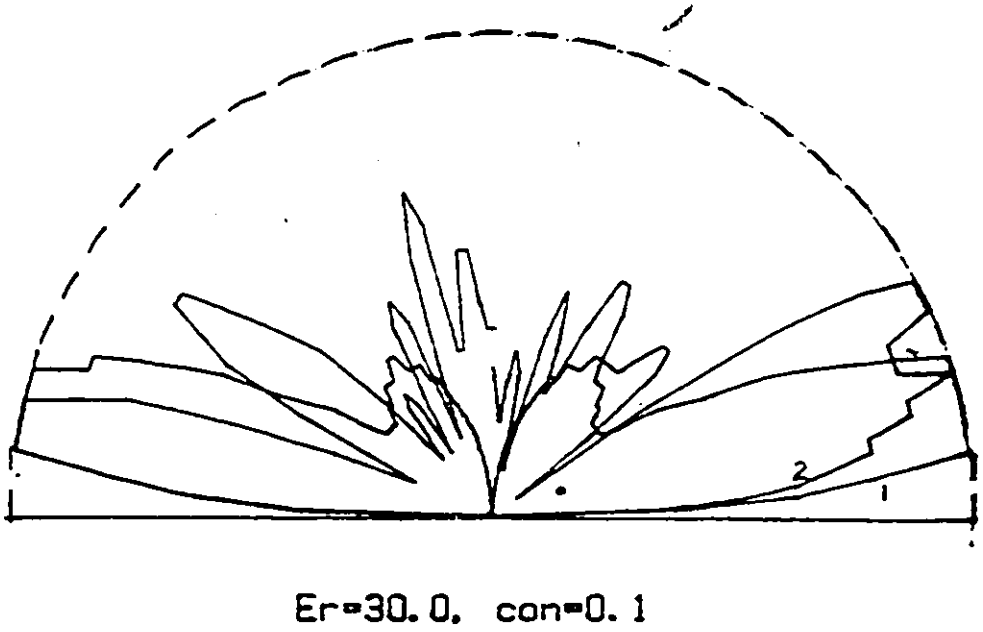

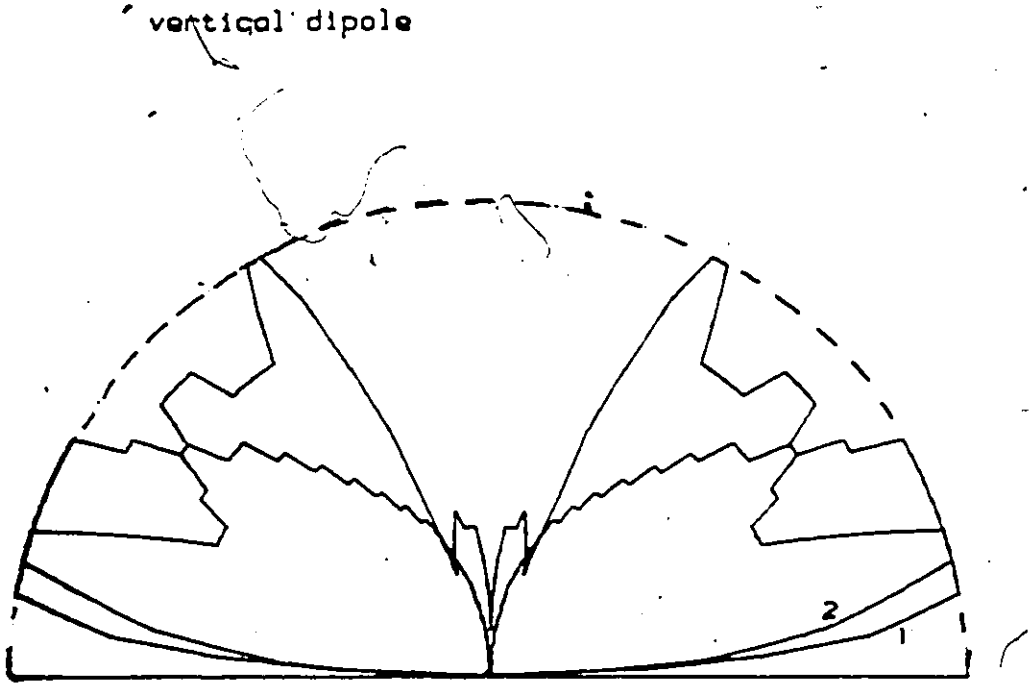

Fig 3.7 The radiation pattern of vertical dipoles configuration for elevation angle $\theta = [-90^0, 90^0]$, $\phi = 90^0$.

It is affected by ground parameters a) $\epsilon = 2.0$, $\sigma = 0.001$, b) $\epsilon = 30.0$, $\sigma = 0.1$, and by a metallic structure 1)without, 2) with metallic structure.

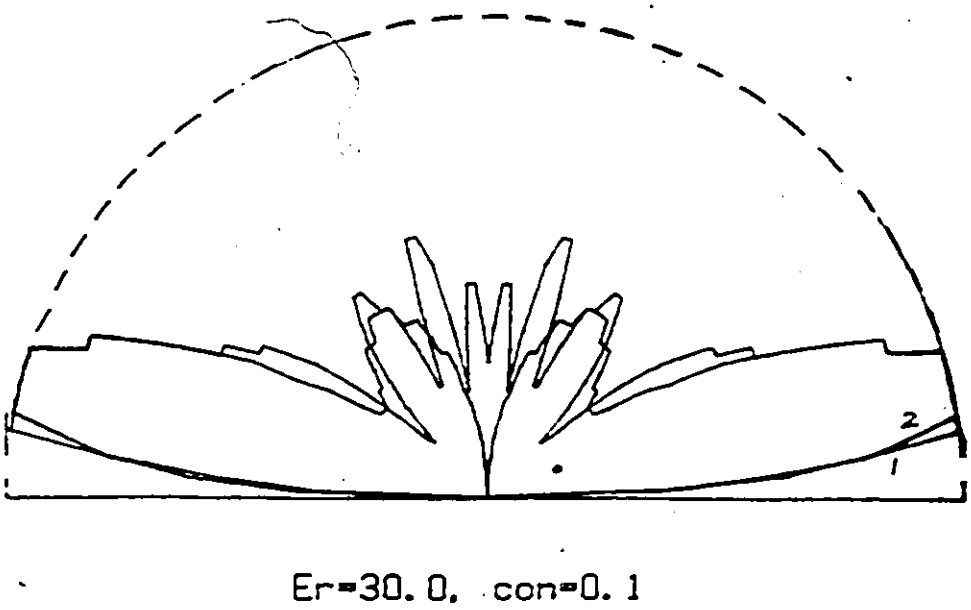

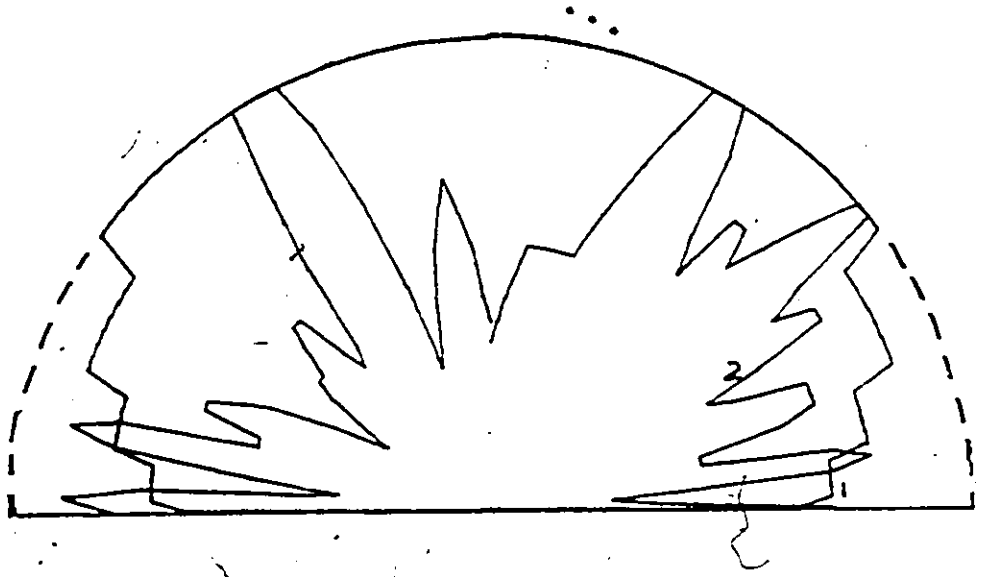

Fig 3.8 The radiation pattern of vertical dipoles configuration for azimuth angle. It is affected by ground parameters a) $\epsilon = 2.0$, $\sigma = 0.001$, b) $\epsilon = 30.0$, $\sigma = 0.1$, and by a metallic structure 1)without, 2) with metallic structure.

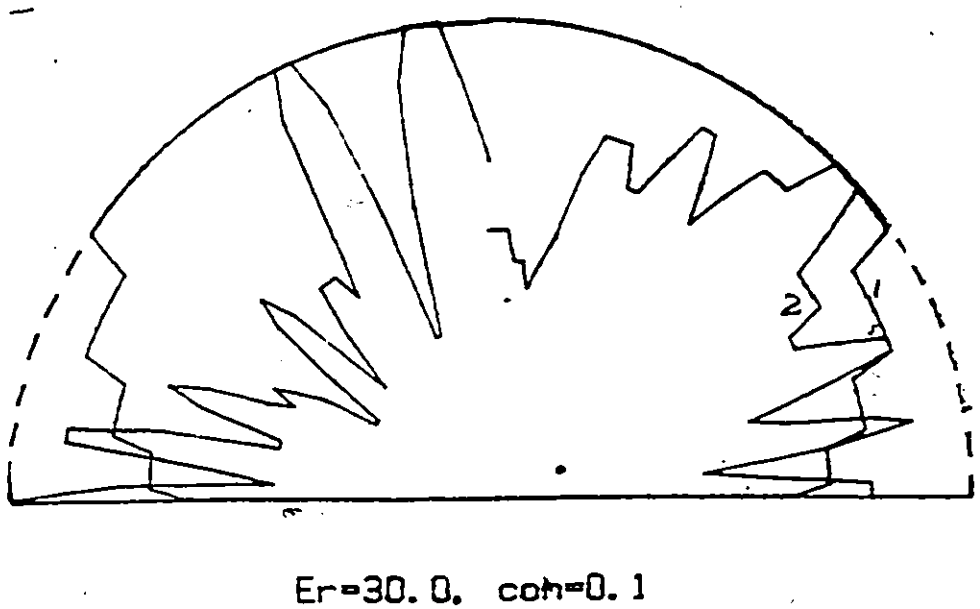

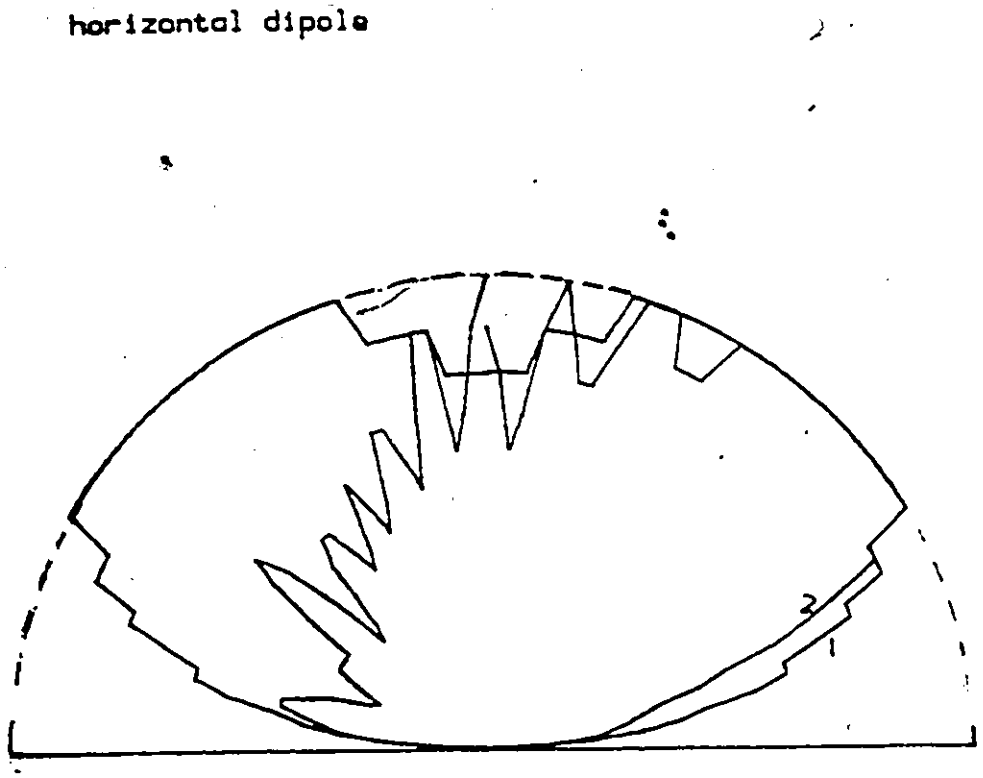

Fig 3.9 The radiation pattern of horizontal dipoles configuration for elevation angle $\theta = [-90^0, 90^0]$, $\phi = 0^0$.

It is affected by ground parameters a) $\epsilon = 2.0$, $\sigma = 0.001$, b) $\epsilon = 30.0$, $\sigma = 0.1$, and by a metallic structure 1)without, 2) with metallic structure.

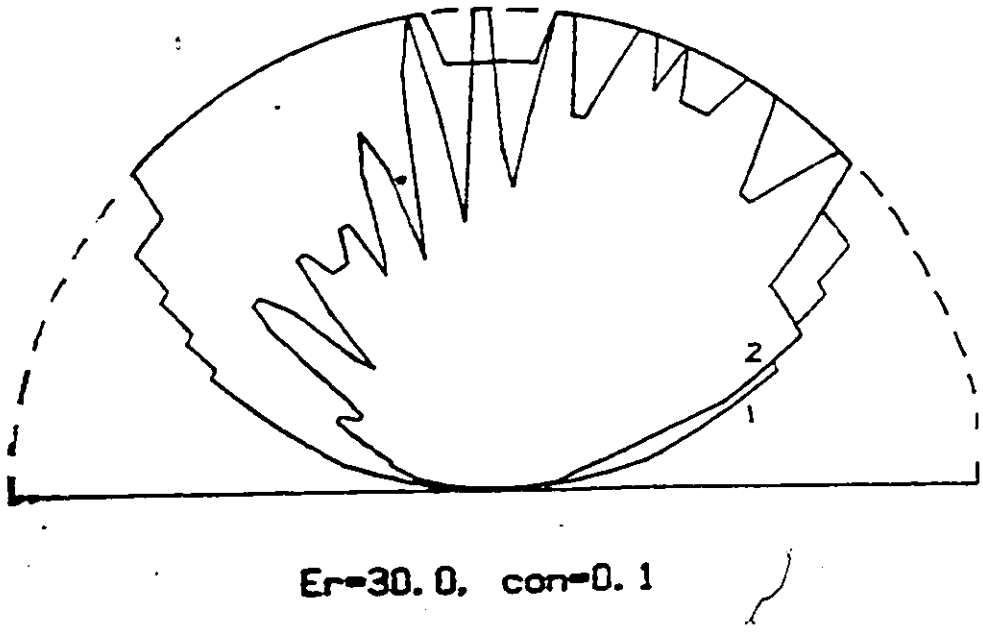

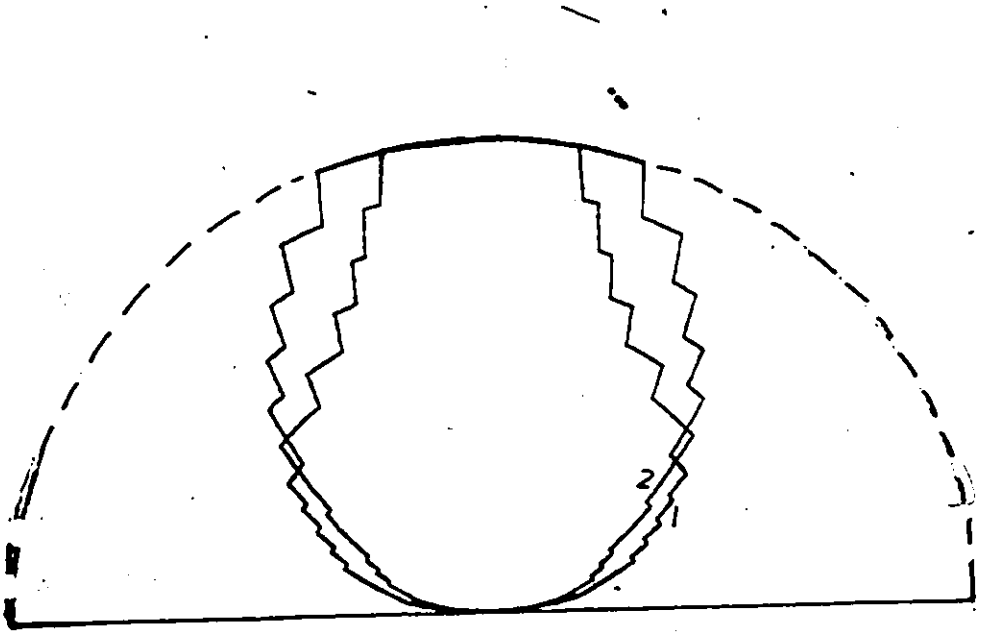

Fig 3.10 The radiation pattern of horizontal dipoles configuration for elevation angle $\theta = [-90^0, 90^0]$, $\phi = 90^0$.

It is affected by ground parameters a) $\epsilon = 2.0$, $\sigma = 0.001$, b) $\epsilon = 30.0$, $\sigma = 0.1$, and by a metallic structure 1)without, 2) with metallic structure.

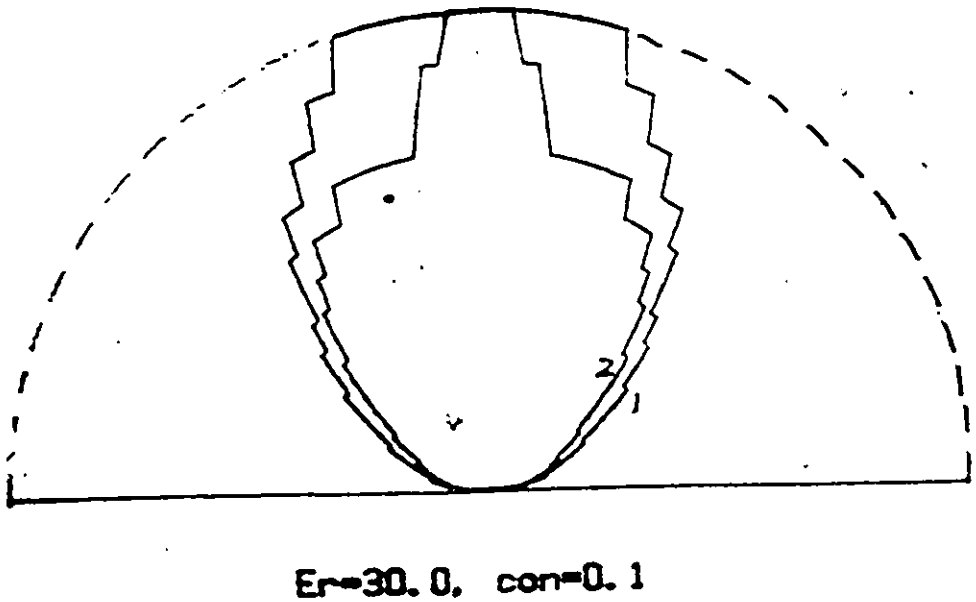

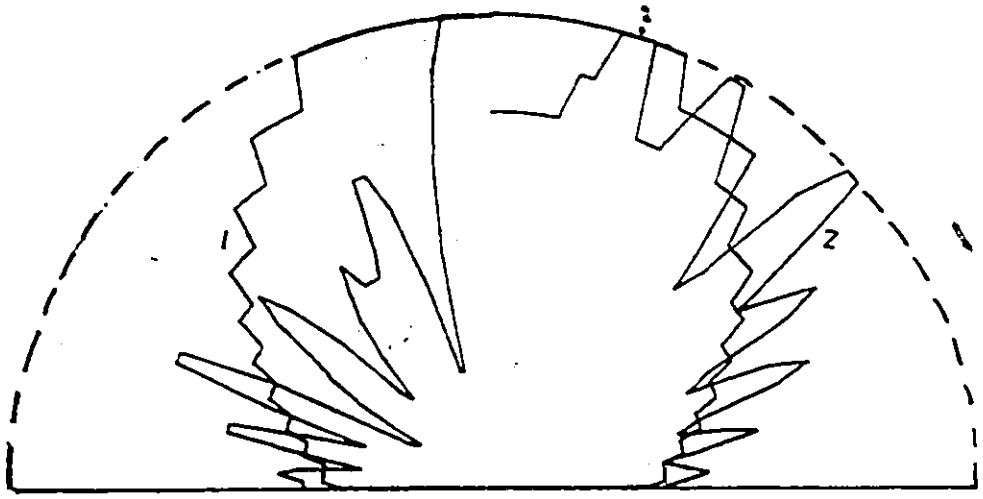

Fig 3.11 The radiation pattern of horizontal dipoles configuration for azimuth angle. It is affected by ground parameters a) $\epsilon = 2.0$, $\sigma = 0.001$, b) $\epsilon = 30.0$, $\sigma = 0.1$, and by a metallic structure 1)without, 2) with metallic structure.

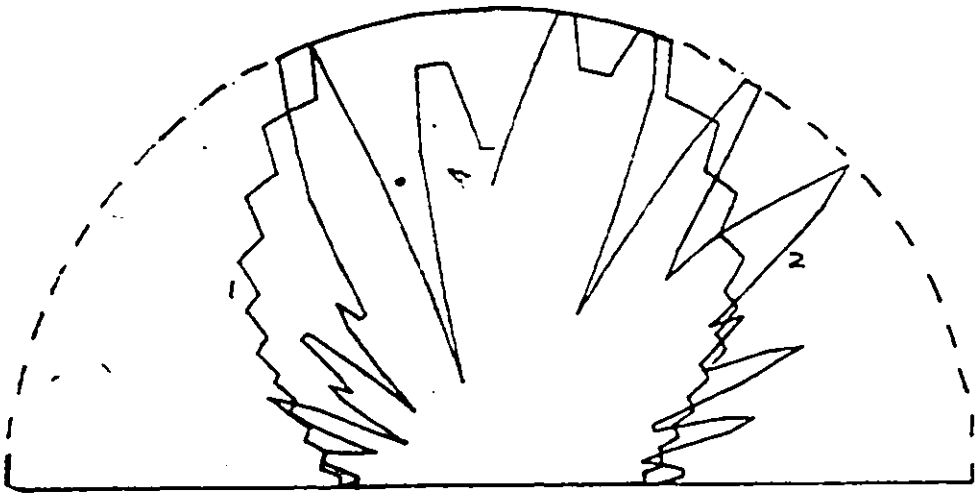

CHAPTER 4

EXPERIMENTAL PROCEDURE & RESULT

As briefly explained before , other researchers of the Laboratory for Electromagnetics and Microwaves was carring out experimental work on scaled down models. The NEC computer package was needed to confirm the validity, through experimental results, of the scale down model. The basic motivation for this experimental procedure is to have a deeper insight into the effects of metal barrack on the field distribution of an antenna. And also airplanes in airport and mobile communication units may disturb the field so that zero radiation pattern, called the shadowing zone, can occur in the vicinity of these structures. The advantage of testing the coverage of an antenna configuration of a security system, using a scaled down model is the flexibility of modifying the environmental structures. For this type of application, very near scattered field measurements should be performed. As a first experimental test, the near field scattering by a conducting sphere was measured and recorded. In order to eliminate environmental effects, experiments were performed in an anechoic chamber which eliminates interference such as reflection from walls, radiation from instruments and other electronic systems, and thus provides a well controlled environment for measurements. The source of radiation was a quarterwave monopole located a few wavelengths away, above a perfectly conducting ground (see Fig 4.1).

The size of the sphere was of the order of a wavelength [18]. A small non-disturbing electric probe was used to measure the electric field intensity at various points near the scatterer. The location of the measurement points was pre-programmed by a computer-aided scanning system. Measured field intensities were automatically acquired, stored, and displayed. This allowed the data to be measured with good accuracy in a relatively short period of time.

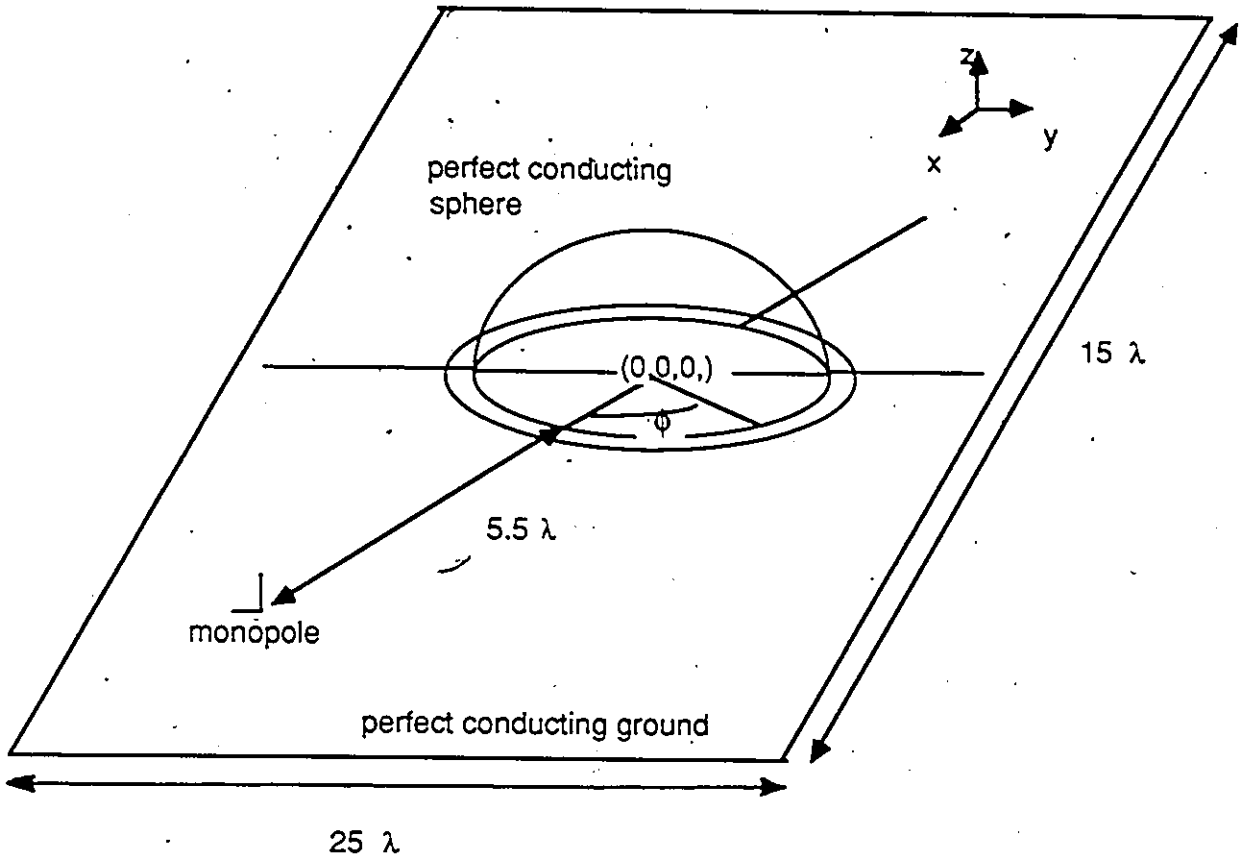

Fig 4.1 Setup of the experiment.

The conducting hemisphere is situated on top of a conducting plane that can be considered of infinite extent. The data points were taken at an short electric distance from the sphere in order to measure the near scattered field.

4.1 Experimental set up

The quarter-wavelength monopole antenna located above the perfectly conducting ground was 6.25 λ_0 away from the origin of the spherical coordinate system. The scatterer, which consisted of a perfectly conducting hemisphere of 1.5 λ_0 diameter was centered at the origin. According to the image method, this situation is equivalent to the case of a conducting sphere in free space irradiated by a halfwave dipole. The hemisphere was covered with nickel paint coating in order to simulate a perfect

conducting surface. The ground plane was wrapped with aluminum foil to simulate a perfect conducting ground. Its dimension were about $25\lambda_0$ by $15\lambda_0$ and the operating frequency was 2.88 GHz. The conducting hemisphere was located at the center of the ground surface. The ground could be considered to be of infinite extent with respect to the sphere size so that edge effects could be neglected. The measurement points were located around the hemisphere at a distance of $1/20\lambda_0$ from it, and at $1/125\lambda_0$ above the ground plane. Also, two sets of measurement points were positioned along the orthogonal axes of the hemisphere in steps of $0.1\lambda_0$.

4.2 Scanning system

A computer-aided scanning system was developed in the Department [39]. The block diagram of the system is shown in Fig 4.2. It basically consists of three units: the transmitter, the receiver and a computer which controls the movement and orientation of the probe, and the data acquisition system.

The output power from the transmitting antenna can be measured by inserting a directional coupler at the output of the generator, as shown in Fig 4.3. Two power meters are connected at the two ports of the directional coupler. The power fed to the antenna can be deduced from the transmitted and the reflected power.

A triaxial electric-field probe, which consists of three miniature dipoles oriented orthogonally with respect to each other, is used to measure the magnitude of the three field components with minimum interaction. Each dipole is covered with a protective substrate to prevent mechanical damage. The RF signal induced in the dipoles is fed to a zero-bias beam lead Schottky diode placed at their center gap, so that it is converted to a DC voltage. The DC output voltage is proportional to the square of the electric field intensity, assuming that the diodes operate in their quadratic zone:

$$|\mathbf{E}|^2 = |E_x|^2 + |E_y|^2 + |E_z|^2$$

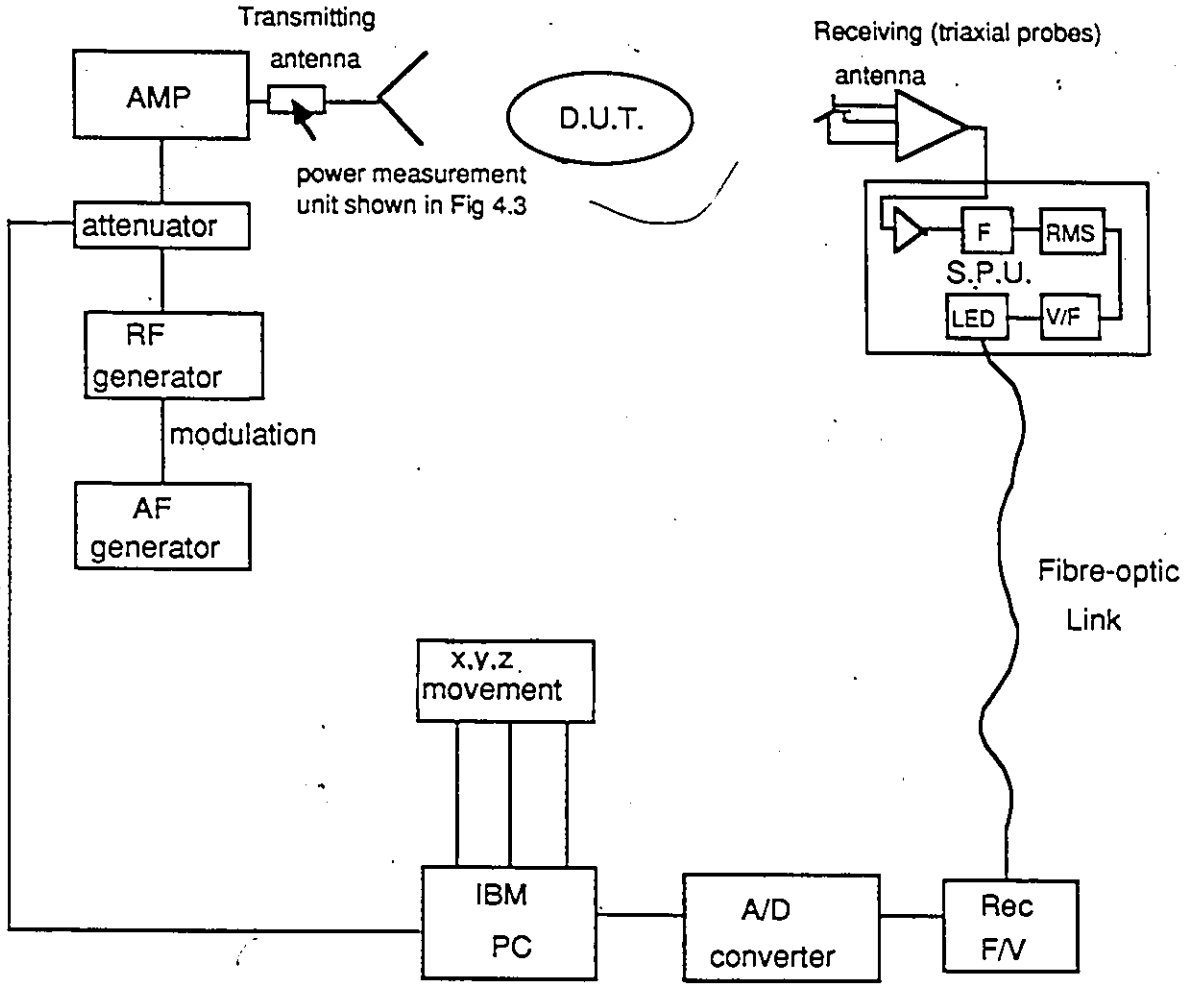

Fig 4.2 Block diagram of the scanning system:

The set-up consists of three basic units: transmitting unit, receiving unit and computer unit. The computer unit is used to control data acquisition and movement of the receiving antenna probe.

The telemetry transmitter mounted on the mechanical scanning unit, is used to amplify and convert the received DC signal into a frequency modulated pulse signal for optical transmission. The signal from the dipoles are summed and amplified in the telemetry transmitter through an RMS voltage to frequency converter in order to convert the DC voltage to a series of frequency modulated digital pulse trains which

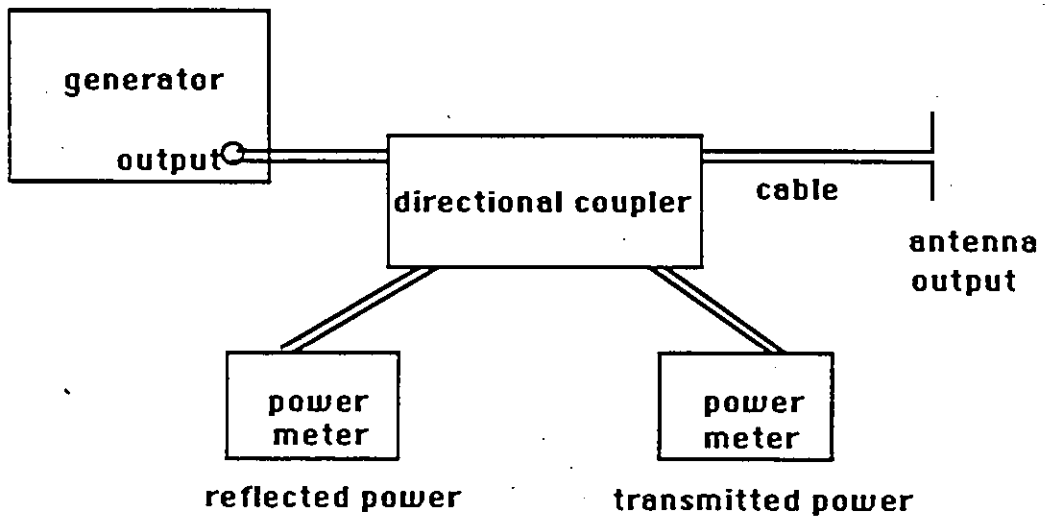

Fig 4.3 The input power feed to the monopole antenna.

are fed to an infrared LED (Light Emitting Diode) that generates the optical signal. The frequency modulated signal from the LED is then transmitted through optical fibre to the receiver outside the anechoic chamber. Optical fibre transmission is used instead of metallic cable, in order to eliminate RF interferences due to the scattering by metallic cables and measurement system electronics, and to reduce the cross talk between transmitting and receiving channels.

The transmitter unit has an R.F.(Radio Frequency) generator, amplitude modulated by an A.F.(Automatic Frequency) generator. A programmable attenuator is used to control the level of the output signal of the generator, which is then amplified and fed to the transmitting antenna.

4.3 Experimental results

Experimental results are compared with those given by the numerical method described in Chapter 2. From Fig 4.4, it can be clearly observed that oscillations appear in the results provided by the numerical method while points from the experimental procedure are smoothly distributed. The reason for this oscillatory behavior

remains unknown at this stage. However, it is felt that it is probably due to numerical instabilities. This explanation will be confirmed in Chapter 5 where the above results are compared with those given by the analytical approach in the same situation. Also, the experimental accuracy expected at that frequency is better than 5% [39] cannot explain the discrepances. In Fig 4.5 and Fig 4.6 the measured electric field at points along the orthogonal axes of the hemisphere are normalized and plotted against the values evaluated by the numerical method. For these two sets of points the numerical method and measurements are in agreement within a constant multiplicative factor in absolute values. This tends to corroborate the conclusion of numerical instabilities for points close to the sphere. Hence, a search for an analytical solution is necessary to validate our conclusion.

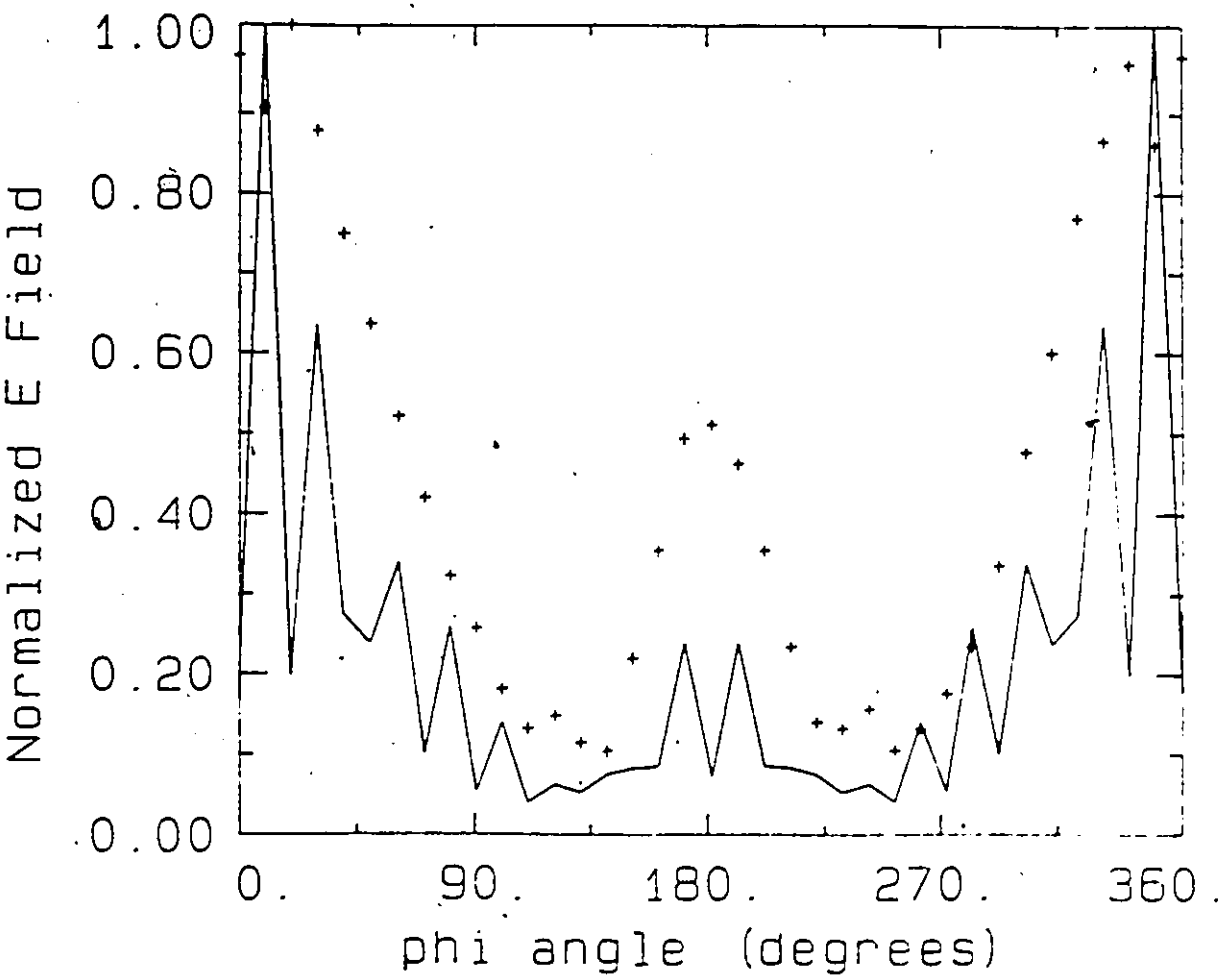

Fig 4.4 Comparison in normalized total electric field between Numerical computation and Experimental results.

(points around the sphere)
Experimental result +, Numerical computation _ .

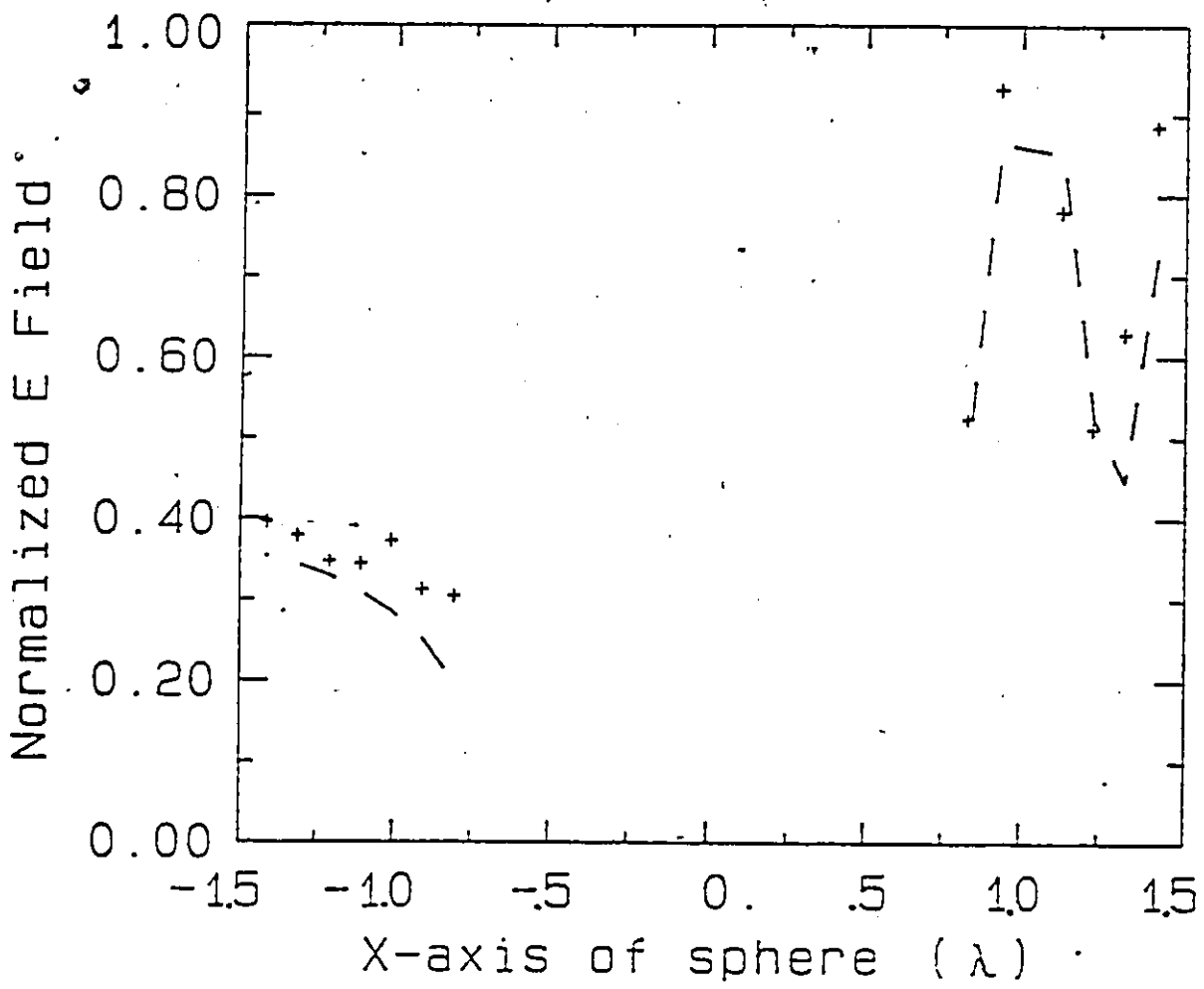

Fig 4.5 Comparison in normalized total electric field between Numerical computation and Experimental results.

(points on the X-axis)
Experimental result +, Numerical computation _ .

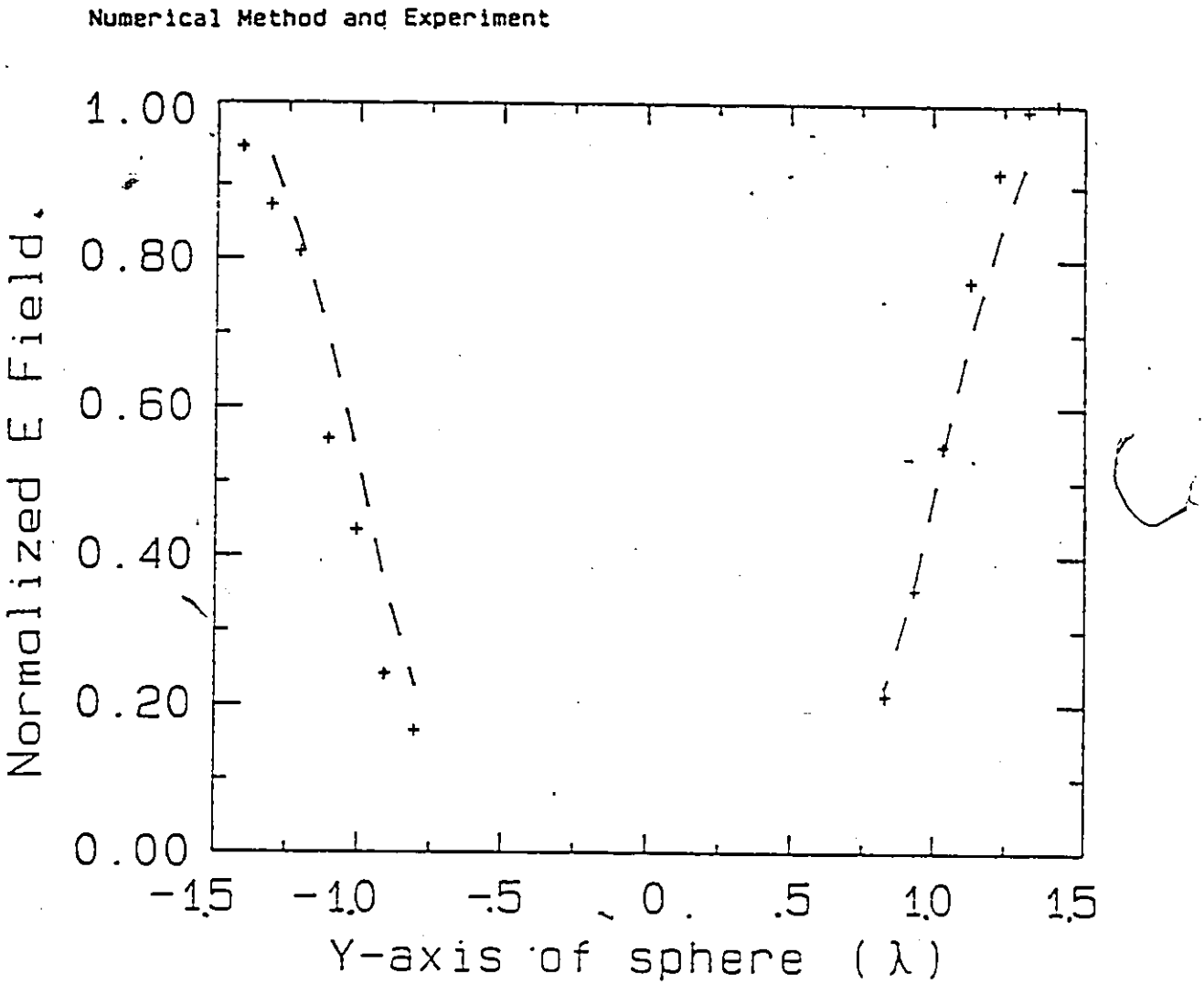

Fig 4.6 Comparison in normalized total electric field between Numerical computation and Experimental results.

(points on the Y-axis)
Experimental result +, Numerical computation _ .

CHAPTER 5

EIGENMODE EXPANSION

5.1 Introduction

The ideal case used in the experiment was a perfectly conducting hemisphere situated above perfect ground. The radiation source was a quarter wavelength monopole located several wavelengths away from the hemisphere. An analytical solution to this experimental situation will be found, in order to compare the results with those obtained experimentally and those obtained by using the numerical method described in Chapter 3. It is important to stress that the analytical solution found in this chapter is not available in the literature and that a new original approach to solve the problem is described in in this thesis. All the structures involved in the experiment, i.e. the hemisphere, the monopole and the ground are perfect conductors. As a result, the problem can be simplified by using the image method, i.e., it can be replaced by the case of a conducting sphere suspended in free space and irradiated by a halfwave dipole.

5.2 Assumptions

In the literature, all analytical solutions pertain to the problem of the scattering of a sphere produced by a plane wave, which pertains to a far field condition [2] [25]. This also implies that the electromagnetic wavefront which is incident upon the sphere is constant in magnitude and, consequently, the size of the sphere should be small. The same assumption cannot be applied in this case, because the size of the sphere is comparable to the distance from the source (see Fig. 5.1).

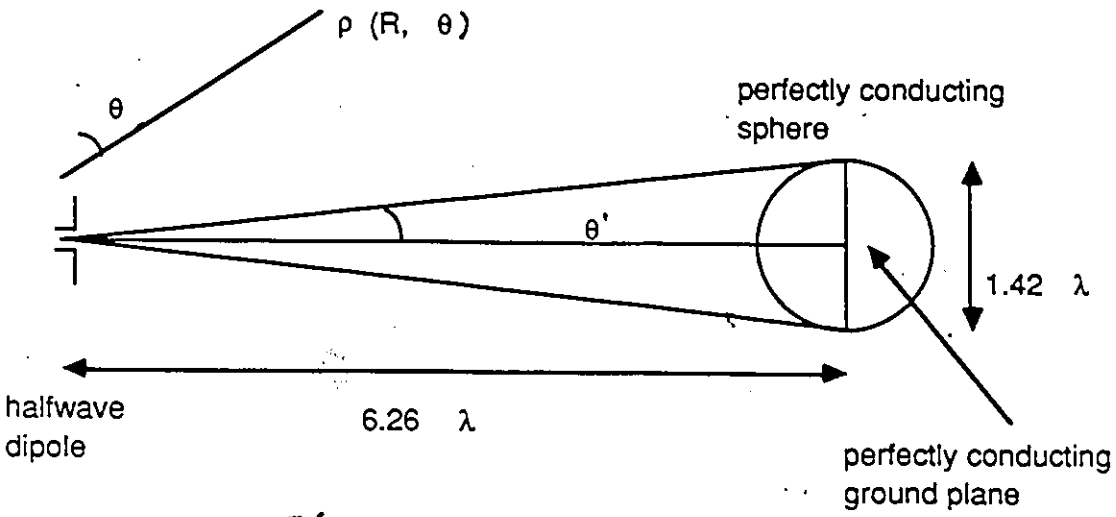

Fig 5.1 Geometry of the problem for the analytical approach.

Since the plane and the hemisphere are perfectly conducting, the image method can be used.

Considering the geometry of the system, the hemisphere can be considered to be located at the far field of the dipole. Indeed, for a short dipole the general expression of the elevation component for the electric field is:

$$E_\theta = \frac{K}{4\pi\epsilon}\left(\frac{1}{R^3} - j\frac{2\pi}{\lambda R^2} - \frac{4\pi^2}{\lambda^2 R}\right)\sin\theta$$

where K is some constant. In our case R=6.26λ. Thus, at the location of the sphere:

$$E_\theta = \frac{K}{4\pi\epsilon}\left(\frac{1}{245.314376\lambda^3} - j\frac{2\pi}{39.1876\lambda^3} - \frac{4\pi^2}{6.26\lambda^3}\right)\sin\theta.$$

The first two terms are negligible when compared to the third term, which is the far field expression of the short dipole:

$$E_\theta = -\frac{K}{4\pi\epsilon}\frac{4\pi^2}{R\lambda^2}\sin\theta$$

The far field pattern of the halfwave dipole can be thought of a superposition of that of short dipoles and is given by [36]:

$$E_\theta = j\omega\mu\frac{2I_m}{k}\frac{e^{-jkR}}{4\pi R}\sin\theta\frac{\cos(\frac{\pi}{2}\cos\theta)}{\sin^2\theta} \qquad (5.1)$$

where I_m is the maximum current distribution occurring at the center of the halfwave dipole. The above expression involves the function $\frac{e^{-jkR}}{jkR}$ and a function of θ. For the halfwave dipole, the electric field at the front and back of the sphere ($\theta = 90°$) is given by:

$$|E_\theta(5.5\lambda)| = \omega\mu\frac{2}{k4\pi(5.5\lambda)}I_m = 8.3339I_m$$

$$|E_\theta(7.02\lambda)| = \omega\mu\frac{2}{k4\pi(7.02\lambda)}I_m = 6.5294I_m$$

The amplitude ratio between the two sides is:

$$\left|\frac{E_\theta(5.5\lambda)}{E_\theta(7.02\lambda)}\right| = \frac{4\pi(7.02\lambda)}{4\pi(5.5\lambda)} = 1.2764$$

As one can see from the above ratios, there is a significant difference between the amplitude of the electric field at the front and the back of the sphere. Therefore, the geometry of this specific problem precludes a representation of the dipole source by a plane wave. In addition, the dependence in θ is a factor that has to be taken into account. However, for the case treated here, it will be shown that the solution can be obtained by replacing, in a first step, the halfwave dipole by a point source at the same location which radiates a pure spherical wave with fields varying as e^{-jkR}/jkR, where $k = 2\pi/\lambda$.

Considering the volume defined by the sphere, which is important for field matching conditions, the expression of the fields developed by the halfwave dipole is, to a good approximation, the same as the one developed by a point source. This is due to the fact that the solid angle at which the sphere is seen by the source is relatively small, as illustrated by Fig. 5.2.

The maximum difference between these two cases in the domain of interest occurs for $\theta' \simeq 7°$. Let Os be unity, then Oh = 0.991 from (5.1). The relative error is at most 1% in magnitude for this assumption. As the angle θ' increases (see Fig 5.3), the validity of the assumption becomes less effective. The radiation pattern of the dipole can no longer be simplified by a single spherical wave expression. In this case,

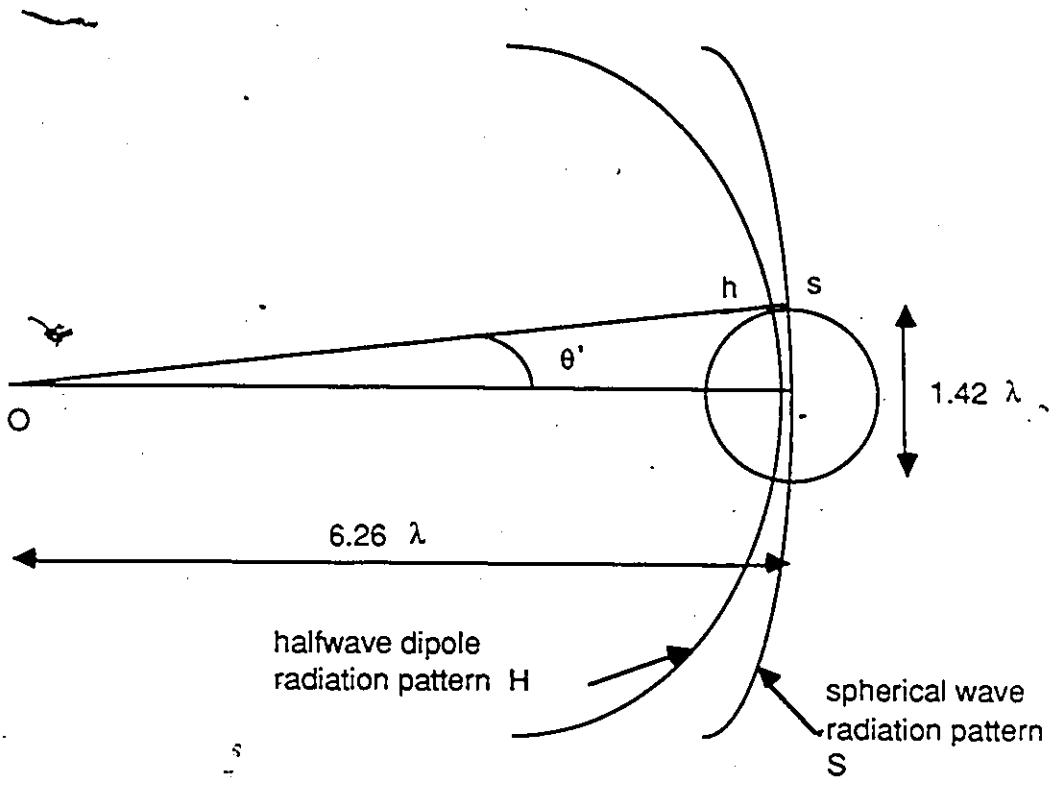

Fig 5.2 Illustration of the assumption.

S and H represents the radiation pattern of the spherical source and the halfwave dipole, respectively.

a spherical wave expansion is required, which complicates the problem in a significant manner.

5.3 Spherical wave expansion

The use of spherical-wave expansions [2] [21] [23] is a well-known technique for solving electromagnetic field problems. The incident field from a radiating object can be decomposed into summations of eigenmodes. In this thesis, the geometry of the problem requires that the eigen functions be spherical wave functions. The scattered field generated by the induced current on the scatterer can be developed with the same set of eigen functions with unknown coefficients. The single spherical wave function

of the point source that is used for the series development is a scalar function that can then be transformed into spherical vector functions. The coefficients of the scattered field can be found by imposing boundary conditions on the total incident field on the surface of the scatterer. Then, once the coefficients are determined, the total field can be found anywhere else.

The scattering sphere is located at the origin of the coordinate system and its scattered field can be expressed by spherical waves generated from the origin. The difficulty resides in the fact that the source (single spherical wave) is not located

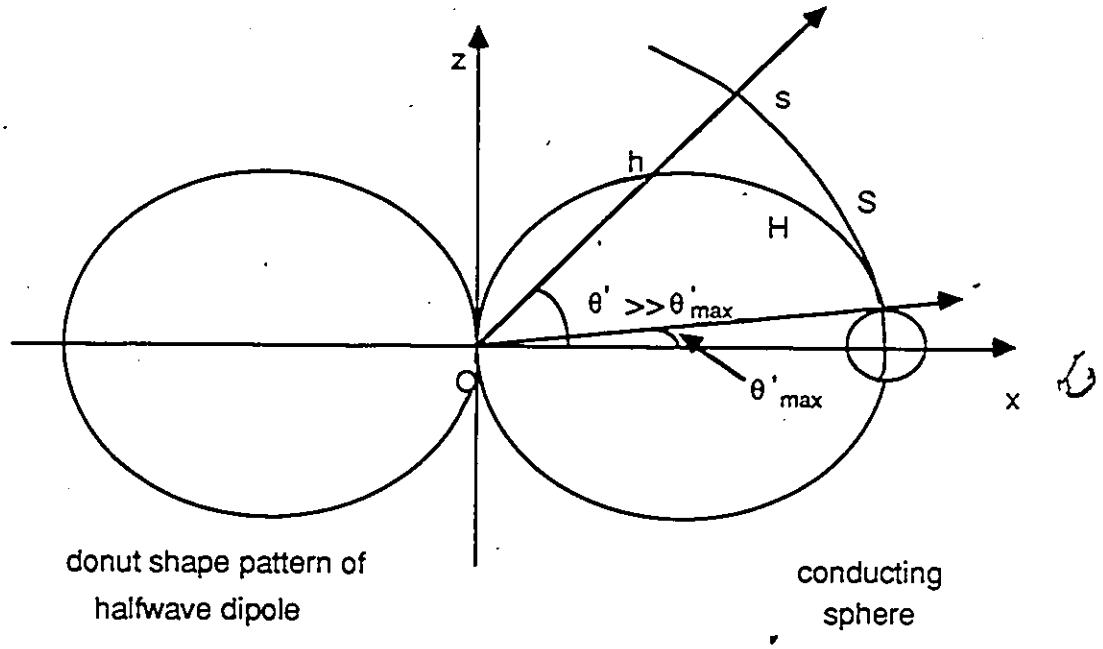

Fig 5.3 Illustration of the error produced by the assumption.

The elevation angle defined in Fig 5.1 is called θ'_{max}. As this angle increases the difference in **Oh** and **Os** will also increase. The increased angle is labelled as θ'.

at the origin and should be expressed by the same set of eigen functions, but with different coefficients.

5.3.1 Scalar representation of the offcentre source

The expansion of an isotropic source centered at the origin is simple, since it requires a single spherical function. However, the expression of the same simple source situated at a point other than the origin is much more involved. Let $B(r_0, \theta_0, \phi_0)$ be a point of observation and $A(r_s, \theta_s, \phi_s)$ the source point of the spherical wave, the coordinates r_0, θ_0, ϕ_0, and r_s, θ_s, ϕ_s are referred to a fixed coordinate system centered at O (see Fig. 5.4). The distance from A to B is, $R = (r_0^2 + r_s^2 - 2r_0 r_s \cos\gamma)^{1/2}$ where $\cos\gamma = \cos\theta_0 \cos\theta_s + \sin\theta_0 \sin\theta_s \cos(\phi_0 - \phi_s)$. The problem consists of representing a wave function generated in A as a sum of spherical waves generated at O, where the scattering sphere is located. The incident wave is spherically symmetric about the source point A, and it is expressed by the scalar function $h_0^{(2)}(kR) = \frac{e^{-jkR}}{-jkR}$ where $h_0^{(2)}(kR)$ is the spherical Hankel function. It is related to the regular Hankel function by:

$$h_n^{(2)}(\rho) = (\frac{\pi}{2\rho})^{1/2} H_{n+\frac{1}{2}}^{(2)}(\rho).$$

It can be expanded in an infinite series [2]:

Suppose $r_0 < r_s$. Then $\frac{e^{-jkR}}{-jkR}$ is finite at $kR = 0$, hence

$$h_0^{(2)}(kR) = \frac{e^{-jkR}}{-jkR} = \sum_{n=0}^{\infty} c_n j_n(kr_0) P_n(\cos\gamma). \tag{5.2}$$

where

$$c_n j_n(kr_0) = \frac{1}{2}(2n+1) \int_0^{\pi} h_0^{(2)}(kR) P_n(\cos\gamma) \sin\gamma d\gamma \tag{5.3}$$

and $P_n(\cos\gamma)$ the Associated Legendre Polynomials. From the relation

$$(\frac{d}{\rho d\rho})^m (\frac{h_n^{(2)}(\rho)}{\rho^n}) = (-1)^m \frac{h_{n+m}^{(2)}(\rho)}{\rho^{n+m}}$$

and using Taylor's theorem [33], one obtains

$$h_0^{(2)}((\rho+\sigma)^{1/2}) = \sum_{m=0}^{\infty} \frac{(-\frac{1}{2}\sigma)^m h_m^{(2)}(\rho^{1/2})}{m! \rho^{1/2m}}$$

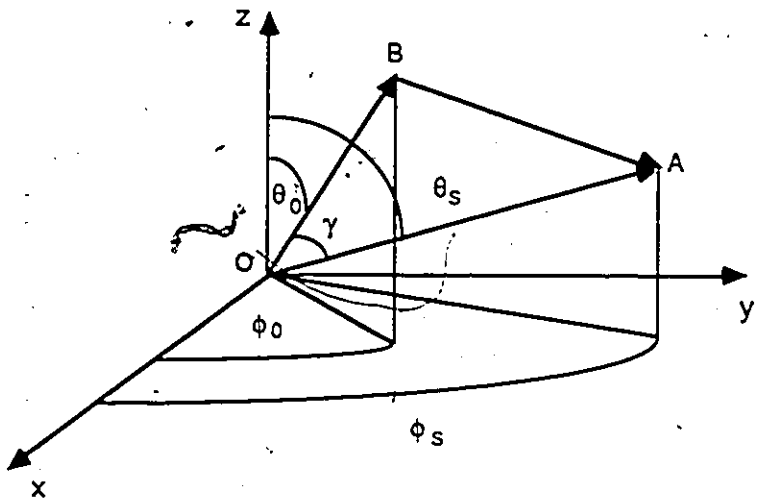

Fig 5.4 Definition of geometrical parameters for the analytical approach.

B is the observation point, A is the source point, where OA = r_s, OB = r_0. The angle γ is the angle between OA and OB, and $|\mathrm{OB}|\cos\gamma$ is the projection of OB upon OA.

Then, if $|\sigma| < |\rho|$ the above expression becomes

$$h_0^{(2)}(kR) = \sum_{m=0}^{\infty} \frac{((kr_0)^2 - 2kr_s kr_0\cos\gamma)^m (-1)^m h_m^{(2)}(kr_s)}{m!(2kr_s)^m}$$

for sufficiently small kr_0. Since $P_n(\cos\gamma)$ is orthogonal to all powers of $\cos\gamma$ less than n, the first term in the expansion of $h_0^{(2)}(kR)$ which gives a contribution to the right-hand side of (5.3) is for m=n.

Taking the derivative n times with respect to kr_0, dividing both sides by $(kr_0)^n$, setting $kr_0 = 0$ and using the identity

$$[\frac{d^n j_n(\rho)}{d\rho^n}]_{\rho=0} = \frac{2^n (n!)^2}{(2n+1)!}$$

in which $j_n(\rho)$ is the spherical Bessel function of the first kind:

$$j_n(\rho) = (\frac{\pi}{2\rho})^{1/2} J_{n+\frac{1}{2}}(\rho)$$

in which $J_n(\rho)$ is the regular Bessel function of the first kind, one obtains

$$c_n \cdot \frac{2^n(n!)^2}{(2n+1)!} = \frac{1}{2}(2n+1)\int_0^{\pi} h_n^{(2)}(kr_s)P_n(\cos\gamma)\cos^n\gamma\sin\gamma d\gamma \qquad (5.4).$$

Then, identifying with (5.4):

$$\int_0^{\pi} P_n(\cos\gamma)\cos^n\gamma\sin\gamma d\gamma = \frac{2^{n+1}(n!)^2}{(2n+1)!}$$

$$c_n = (2n+1)h_n^{(2)}(kr_s).$$

Finally, substituting into (5.2) yields

$$h_0^{(2)}(kR) = \frac{e^{-jkR}}{-jkR} = \sum_{n=0}^{\infty}(2n+1)h_n^{(2)}(kr_s)j_n(kr_0)P_n(\cos\gamma) \quad (r_0 < r_s) \qquad (5.5)$$

Since $h_0^{(2)}(kR)$ is symmetrical with respect to r_s and r_0, one can easily find

$$h_0^{(2)}(kR) = \sum_{n=0)}^{\infty}(2n+1)h_n^{(2)}(kr_0)j_n(kr_s)P_n(\cos\gamma) \quad (r_0 > r_s) \qquad (5.6)$$

where $P_n(\cos\gamma)$ can be written as

$$P_n(\cos\gamma) = \sum_{m=0}^{n}\epsilon_m\frac{(n-m)!}{(n+m)!}P_n^m(\cos\theta_0)P_n^m(\cos\theta_s)\cos m(\phi_0-\phi_s)$$

where $\epsilon_m = 1$, if $m = 0$, and $\epsilon_m = 2$ otherwise. $P_n^m(\cos\theta)$ is the Associate Legendre Polynomials.

5.3.2 Total Electric field outside the sphere

The solutions of the vector wave equation in spherical coordinates can be deduced directly from the characteristic functions (5.5) and (5.6) above. Consider a scalar function f, which is the solution of the wave equation

$$\nabla^2 f + k^2 f = 0$$

It can be shown [2] that three independent vector solutions L,M,N can be constructed from f:

$$\mathbf{L} = \nabla \cdot f$$

and

$$\mathbf{M} = \nabla \times \mathbf{r}f = \mathbf{L} \times \mathbf{r} = \frac{1}{k}\nabla \times \mathbf{N}. \tag{5.7}$$

Since the divergence of the electric field is zero , and L is a purely longitudinal field, the vector solution can be expressed in term of M,N alone:

$$M_r = 0, \qquad M_\theta = \frac{1}{\sin\theta}\frac{\delta f}{\delta \phi}, \qquad M_\phi = -\frac{\delta f}{\delta \theta}, \tag{5.8}$$

and

$$N_r = \frac{n(n+1)}{kr} f, \qquad N_\theta = \frac{1}{kr}\frac{\delta^2(rf)}{\delta r \delta \theta}, \qquad N_\phi = \frac{1}{kr\sin\theta}\frac{\delta^2(rf)}{\delta r \delta \phi}. \tag{5.9}$$

Therefore, the electric field generated from a spherical symmetrical source point at A is found as

$$\mathbf{E}_{inc} = \mathbf{M} + \mathbf{N} \tag{5.10}$$

where, from (5.8) and (5.9), the components of M and N are

$$\begin{aligned}
M_r &= 0, \\
M_\theta &= -\sum_{n=0}^{\infty}(2n+1)h_n^{(2)}(kr_s)j_n(kr) \\
&\quad \sum_{m=0}^{n}\epsilon_m m\frac{(n-m)!}{(n+m)!}P_n^m(\cos\theta_s)\frac{P_n^m(\cos\theta)}{\sin\theta}\sin m(\phi-\phi_s), \\
M_\phi &= -\sum_{n=0}^{\infty}(2n+1)h_n^{(2)}(kr_s)j_n(kr) \\
&\quad \sum_{m=0}^{n}\epsilon_m \frac{(n-m)!}{(n+m)!}P_n^m(\cos\theta_s)\frac{\delta}{\delta\theta}[P_n^m(\cos\theta)]\cos m(\phi-\phi_s).
\end{aligned}$$

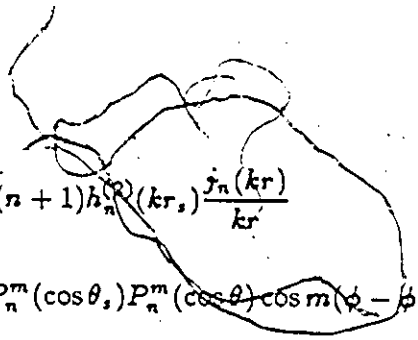

$$N_r = \sum_{n=0}^{\infty}(2n+1)(n)(n+1)h_n^{(2)}(kr_s)\frac{j_n(kr)}{kr}$$
$$\sum_{m=0}^{n}\epsilon_m\frac{(n-m)!}{(n+m)!}P_n^m(\cos\theta_s)P_n^m(\cos\theta)\cos m(\phi-\phi_s),$$

$$N_\theta = \sum_{n=0}^{\infty}(2n+1)h_n^{(2)}(kr_s)\frac{[krj_n(kr)]'}{kr}$$
$$\sum_{m=0}^{n}\epsilon_m\frac{(n-m)!}{(n+m)!}P_n^m(\cos\theta_s)\frac{\partial}{\partial\theta}[P_n^m(\cos\theta)]\cos m(\phi-\phi_s),$$

$$N_\phi = -\sum_{n=0}^{\infty}(2n+1)h_n^{(2)}(kr_s)\frac{[krj_n(kr)]'}{kr}$$
$$\sum_{m=0}^{n}\epsilon_m m\frac{(n-m)!}{(n+m)!}P_n^m(\cos\theta_s)\frac{P_n^m(\cos\theta)}{\sin\theta}\sin m(\phi-\phi_s).$$

The induced secondary field from the conducting surface can be constructed as

$$\mathbf{E}_{scat} = \sum_{n=0}^{\infty}a_n^r\mathbf{m}_0 + b_n^r\mathbf{n}_0 \tag{5.11}$$

where

$$E_{scat\ r} = \sum_{n=0}^{\infty}\sum_{m=0}^{n}b_n^r(n)(n+1)\frac{h_n^{(2)}(kr)}{kr}p_n^m(\cos\theta)\cos m\phi,$$

$$E_{scat\ \theta} = \sum_{n=0}^{\infty}\sum_{m=0}^{n}a_n^r(-mh_n^{(2)}(kr)\frac{P_n^m(\cos\theta)}{\sin\theta}\sin m\phi)$$
$$+ b_n^r(\frac{[krh_n^{(2)}(kr)]'}{kr}\frac{\partial}{\partial\theta}[P_n^m(\cos\theta)]\cos m\phi),$$

$$E_{scat\ \phi} = \sum_{n=0}^{\infty}\sum_{m=0}^{n}a_n^r(-h_n^{(2)}(kr)\frac{\partial}{\partial\theta}[P_n^m(\cos\theta)]\cos m\phi)$$
$$+ b_n^r(-m\frac{[krh_n^{(2)}(kr)]'}{kr}\frac{P_n^m(\cos\theta)}{\sin\theta}\sin m\phi)$$

Applying the boundary condition at $r = a$, where a is the radius of the sphere, onto the surface of the sphere yields

$$E_{inc_\theta} + E_{scat_\theta} = 0$$
$$E_{inc_\phi} + E_{scat_\phi} = 0 \tag{5.12}$$

From (5.12) the coefficients a_n^r and b_n^r of the scattered field can be determined:

$$a_n^r = -\sum_{n=0}^{\infty}(2n+1)h_n^{(2)}(kr_s)\frac{j_n(ka)}{h_n^{(2)}(ka)}\sum_{m=0}^{n}\epsilon_m\frac{(n-m)!}{(n+m)!}P_n^m(\cos\theta_s) \tag{5.13}$$

$$b_n^r = -\sum_{n=0}^{\infty}(2n+1)h_n^{(2)}(kr_s)\frac{[kaj_n(ka)]'}{[kah_n^{(2)}(ka)]'}\sum_{m=0}^{n}\epsilon_m\frac{(n-m)!}{(n+m)!}P_n^m(\cos\theta_s) \qquad (5.14)$$

Details of the derivation is given in the appendix.

The resultant total field at any point outside the sphere is the vector sum of the incident field given by (5.10) and the scattered field given by (5.11):

$$\mathbf{E}_{total} = \mathbf{E}_{inc} + \mathbf{E}_{scat} \qquad (5.15)$$

where $\mathbf{E}_{inc}$ is given by (5.1).

It is important to notice that for determining the coefficients of the eigenmodes for the scattered field expansion, the source of radiation could be approximated by a spherical point source. However, for the computation of the total field the original expression of the dipole is used, since the observation point can be at any location where the assumption of point source is not necessarily valid.

5.4 Results of the eigenmode expansion

As discussed earlier in section 5.2, due to the geometry of the experiment, the conventional plane wave approximation could not be applied. Consequently, another model was chosen to approximate the dipole source of radiation. The model chosen was spherical wave expansion technique to represent an offcenter point source at the same coordinate as the center of the radiating dipole. The scattered field was found by imposing the boundary conditions on the conducting sphere surface. The total electric field at any other point was simply the vector sum of the incident and scattered electric field. The theoretical analysis was implemented on a VAX11/750 computer. The program code can be found in the appendix. First of all, the incident spherical wave electric field is computed to verify the convergence of the series expansion. Then, the total field is computed in the near-field scattered region of the sphere and the results are compared with the measurements and the numerical approach.

5.4.1 Spherical wave expansion for the incident wave

The series expansion for the spherical wave generated by a point source, involves an infinite summation. However, in practice, the summation has to be truncated to a reasonable number of modes. To determine the convergence of the series, the electric field around the offcenter source at equidistant points was computed. A convergence test was used in the program to terminate the summation process. This is to optimize the computation time and the summation process and to minimize truncation errors. The convergence criterion is defined by the parameter ϵ which is defined as the percentage difference between the previous computed value and the current computed value. The convergence criterion of 10^{-4} is considered acceptable and was used in the computaton. Convergence was observed for about 60 terms with this criterion.

The magnitude and phase of the theoretical expansion of the incident electric field wave are plotted in Fig 5.5, Fig 5.6 and Fig 5.7, in the OXZ, OYZ, and OXY plane, respectively. In each plane, the observation points were taken on concentric circles centered on the offcentered point source. Their radii were varied from 2 to 8 λ_0 in 2 λ_0 steps. For observation points near the source, some ripples occurred as can be seen in Fig 5.5a, Fig 5.6a, and Fig 5.7a. However, for the region of interest, where the scattering sphere is located, the magnitude of the field is constant, as is expected for a spherical wave. The phase of the electric field is plotted in Fig 5.5b, Figs 5.6b, and 5.7b. Ripples are also observed in the OXZ, and OXY plane (see Fig 5.5b, Fig 5.7b). Again, as for the magnitude, the phase is constant in the region of interest, which is the case for a spherical wave.

In order to compare the analytical results and the measurements, the total electric field was calculated at the same locations as shown in Fig 5.8.

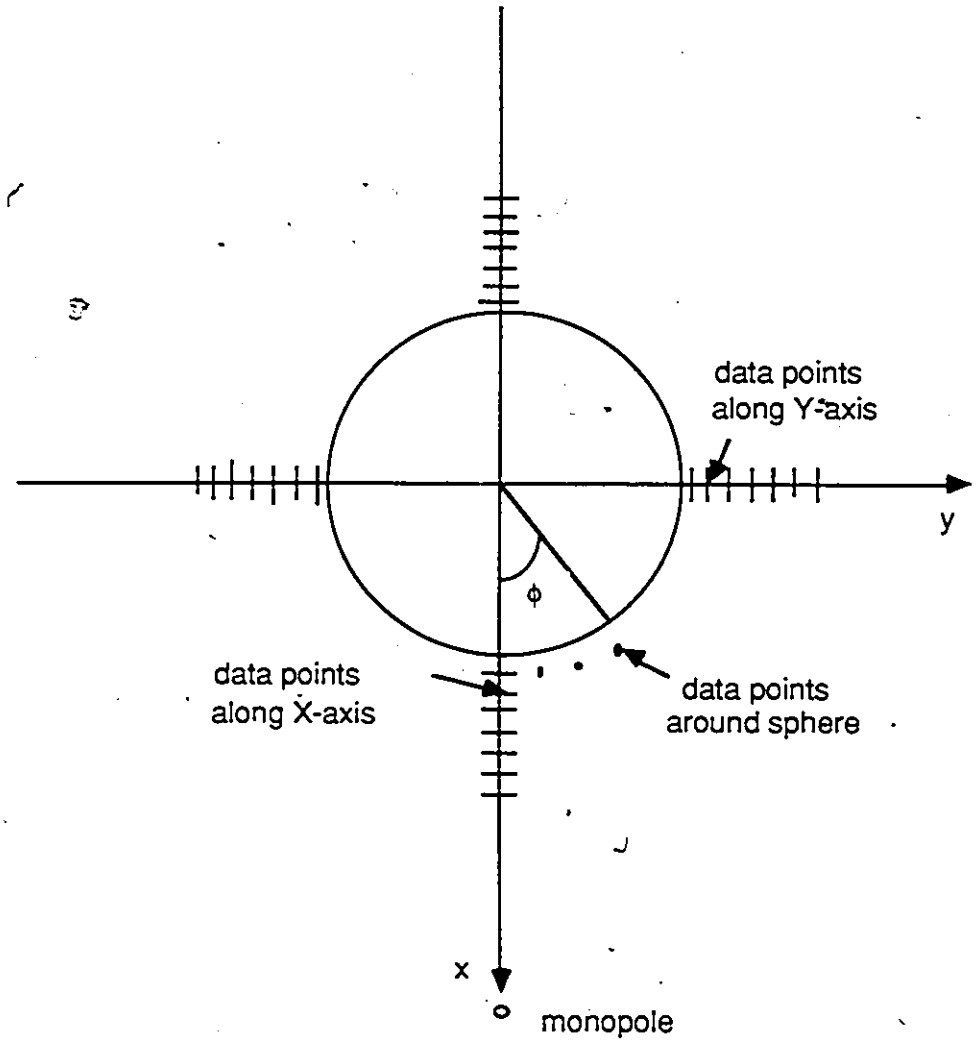

Fig 5.8 Location of the experimental points around a conducting half sphere.

Within a constant factor, the values computed by numerical method and theoretical analysis agree remarkably well with the measurements for observation points located on the axes of the sphere, as shown in Figs 5.9 and 5.10. However, for points located around the sphere, the numerical method displays an oscillatory behavior which is not corroborated either by the eigen mode expansion or the experimental results (see Fig 5.11). In this case, the distance of the observation points from the sphere was $1/20\lambda$ at 2.88 GHz. In the case of the theoretical analysis, the observation

points give a smooth curve. However, there is some discrepancy around 180° between the theoretical analysis and the experimental results. It may also due to the fact that the observation points are too close to the sphere, since the results for the X and Y axes are in good agreement with the experimental results. In order to further confirm that the oscillatory behavior is due to numerical errors, the observation points were located a little further away from the sphere and then reevaluated by the numerical method. The oscillatory behavior disappeared and resulted in a smooth curve as can be see in Fig 5.12, where the distance was increased to $1/5\lambda_0$. One can conclude that, these numerical instabilities are due to the coupling between the measuring probe and the scattered sphere.

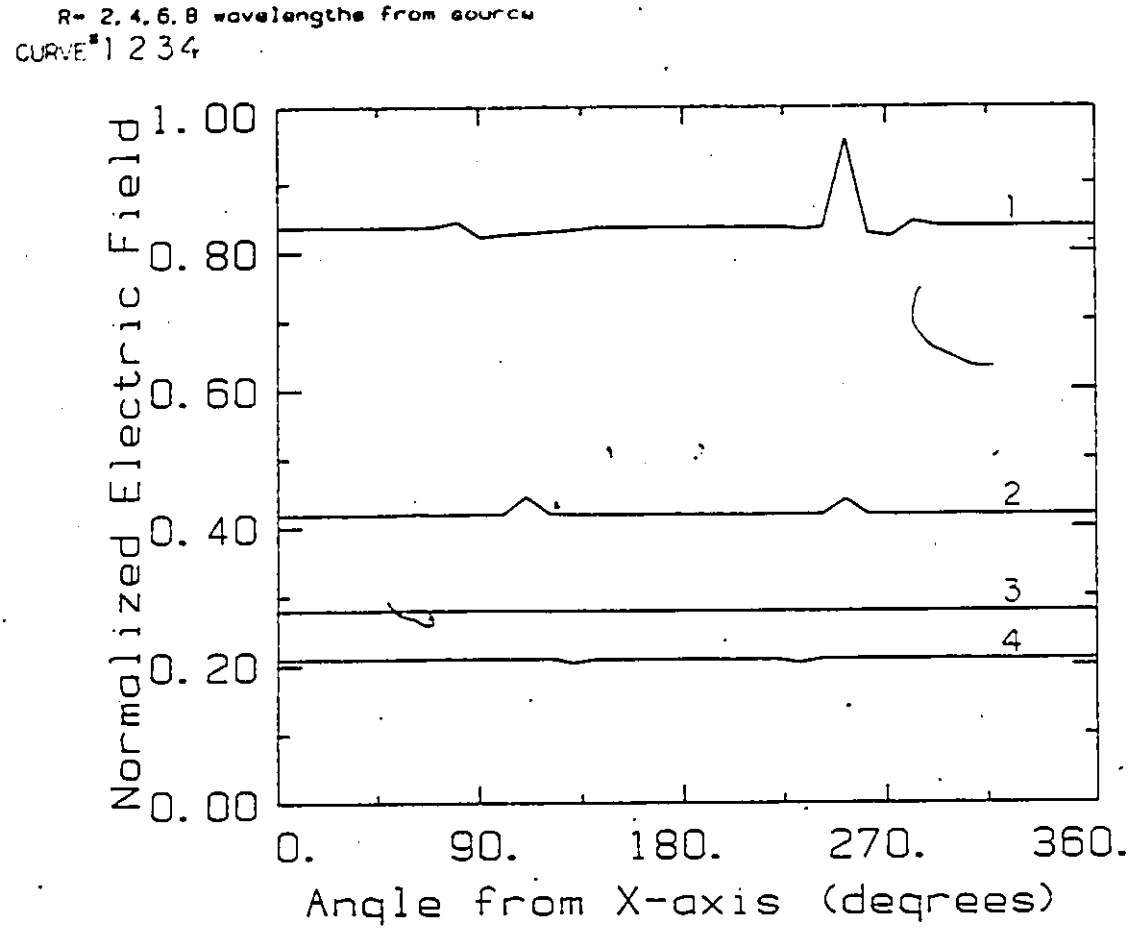

Fig 5.5 Eigen-mode generated wave fronts of a point source (plane OXZ).

(a) Constant magnitude plot and (b) constant phase plot of equidistance points from the points source. In a plane parallel to XZ plane.

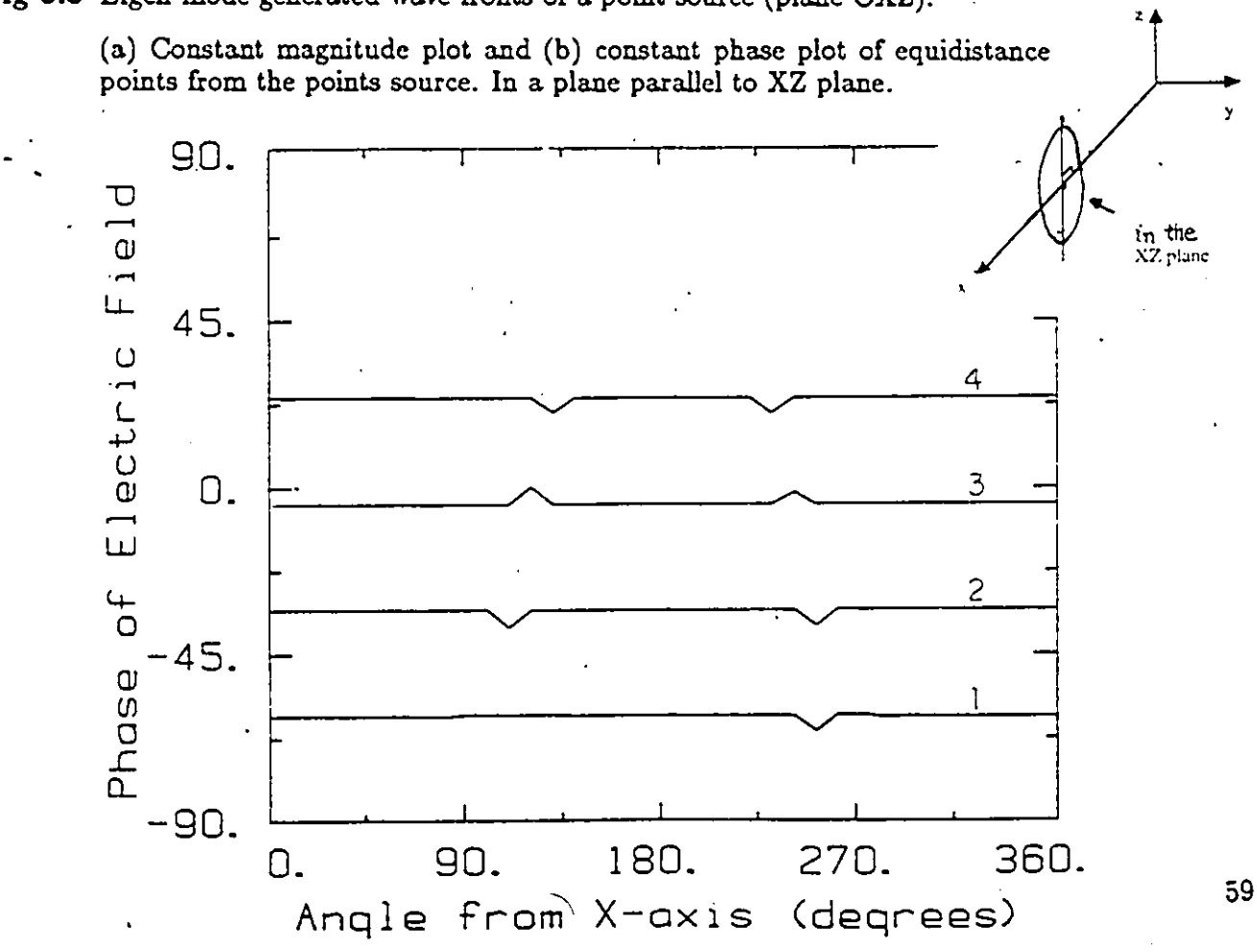

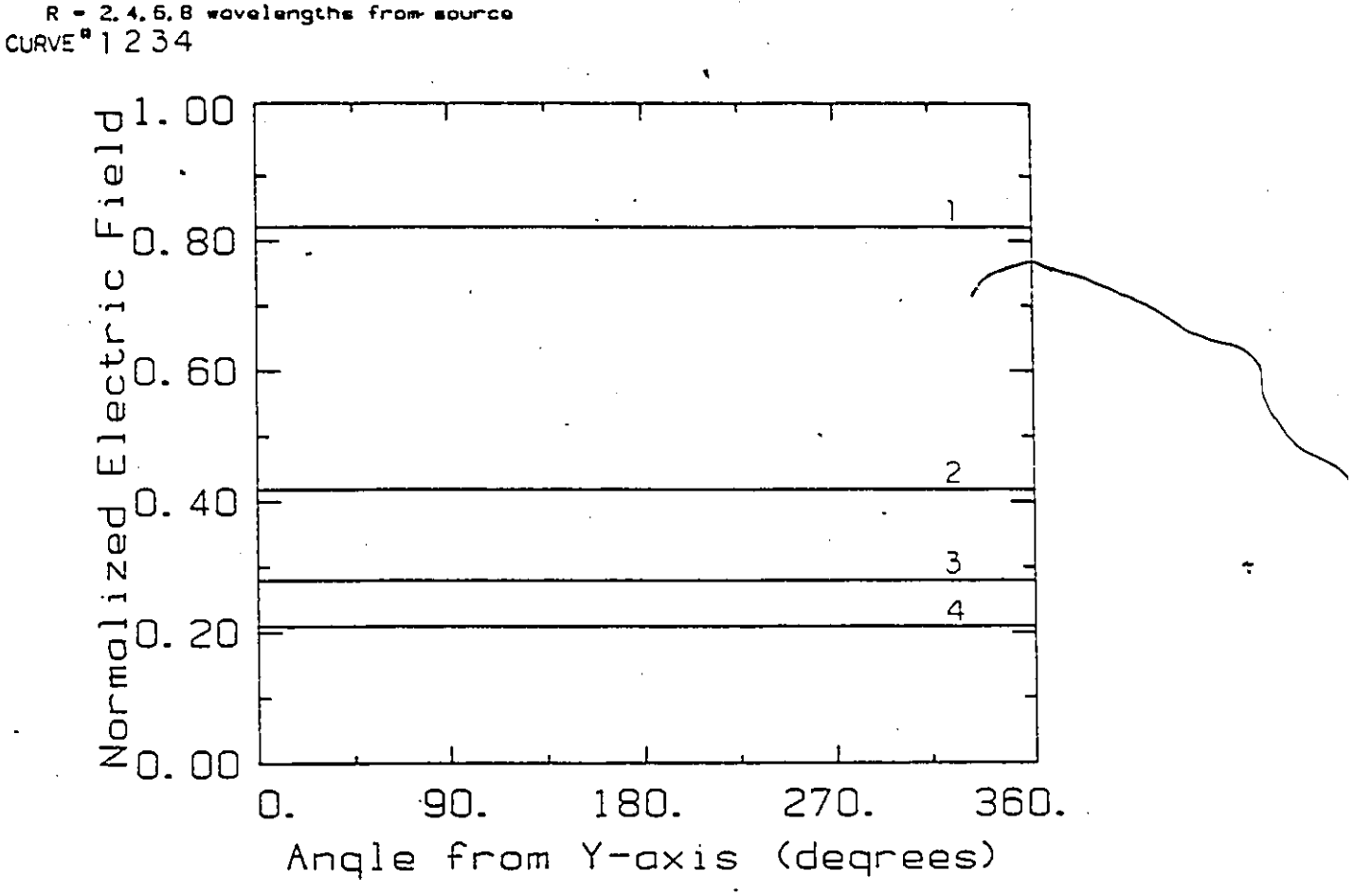

Fig 5.6 Eigen-mode generated wave fronts of a point source (plane OYZ).

(a) Constant magnitude plot and (b) constant phase plot of equidistance points from the points source. In a plane parallel to YZ plane.

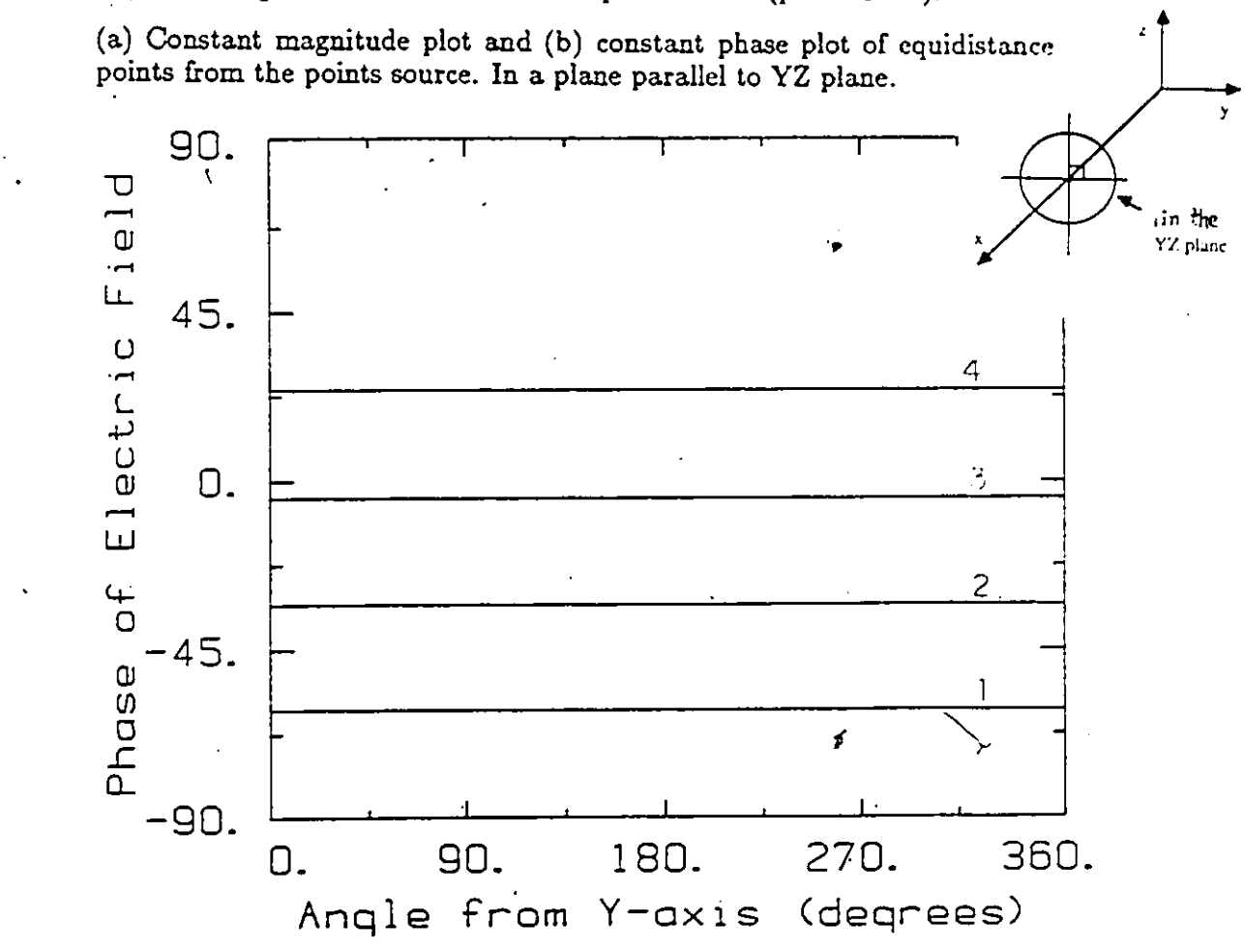

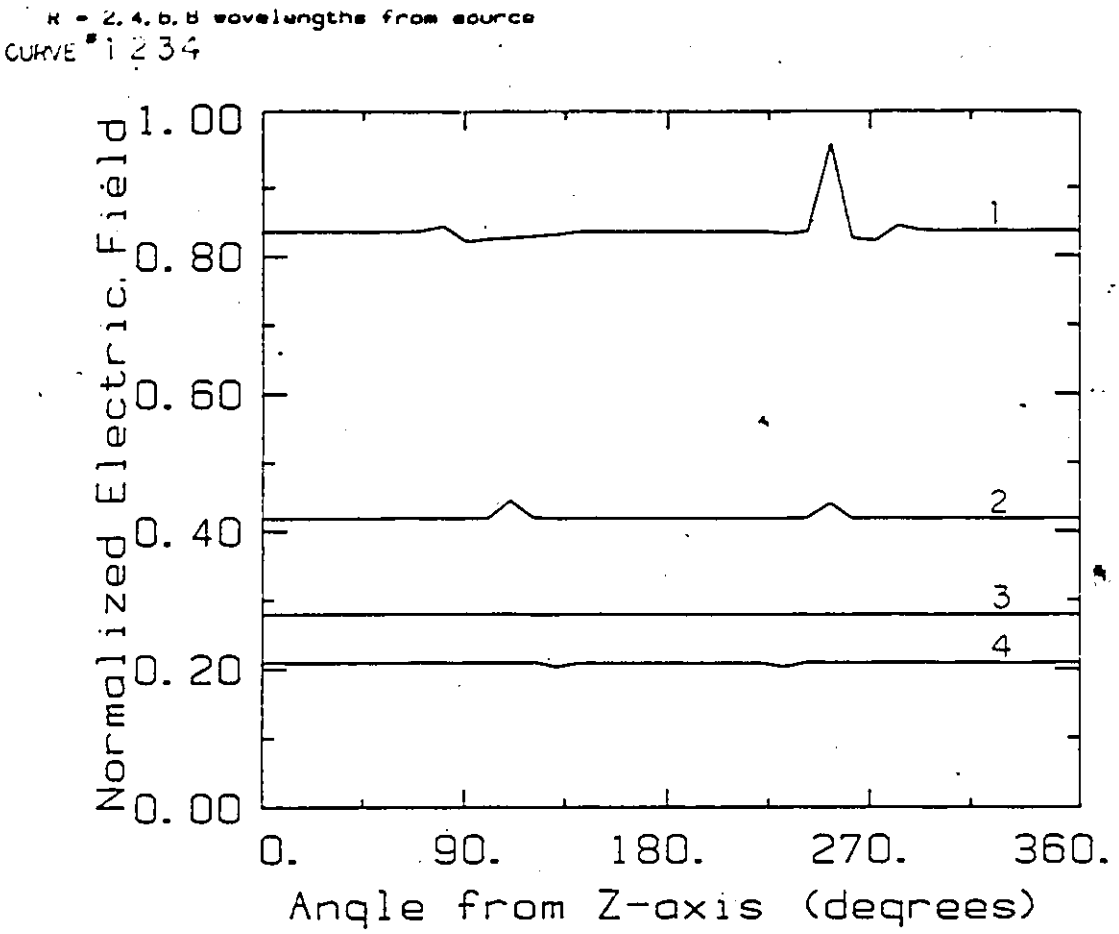

Fig 5.7 Eigen-mode generated wave fronts of a point source (plane OXY).

(a) Constant magnitude plot and (b) constant phase plot of equidistance points from the points source. In a plane parallel to XY plane.

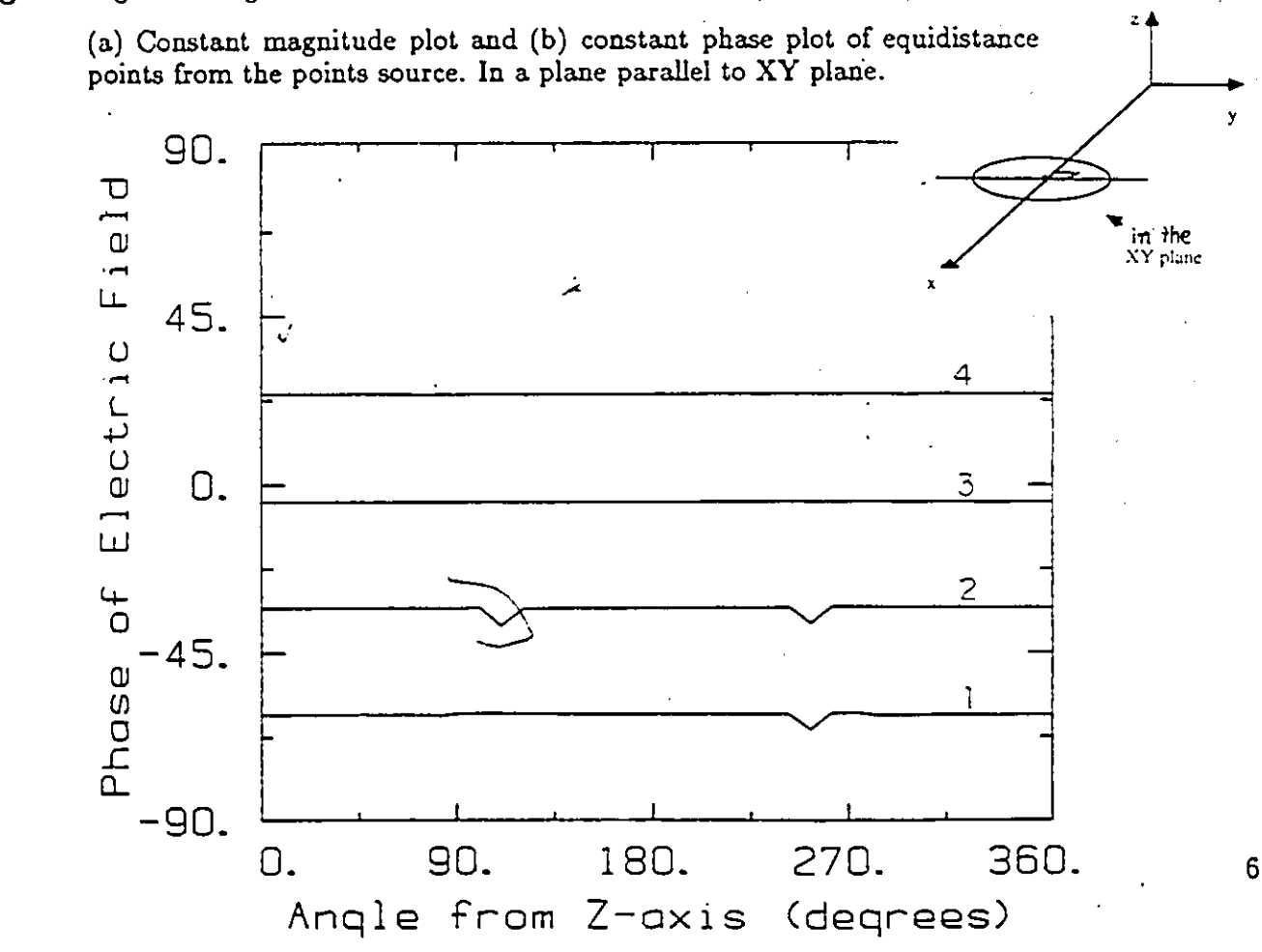

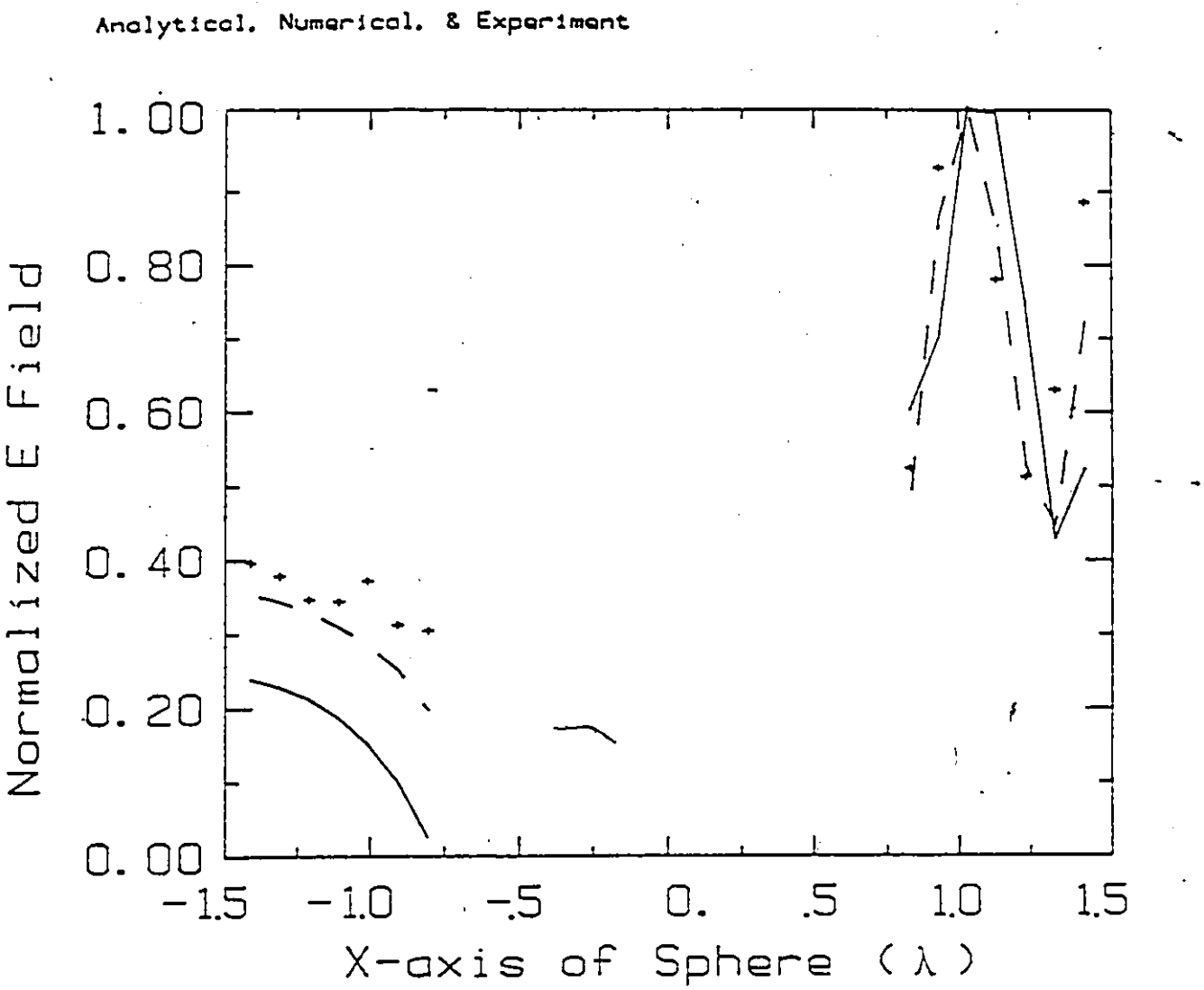

Fig 5.9 Comparison in normalized total electric field between the different methods.

(points on the X-axis)
Experimental result +, eigenmode expansion _ , numerical computation ––.

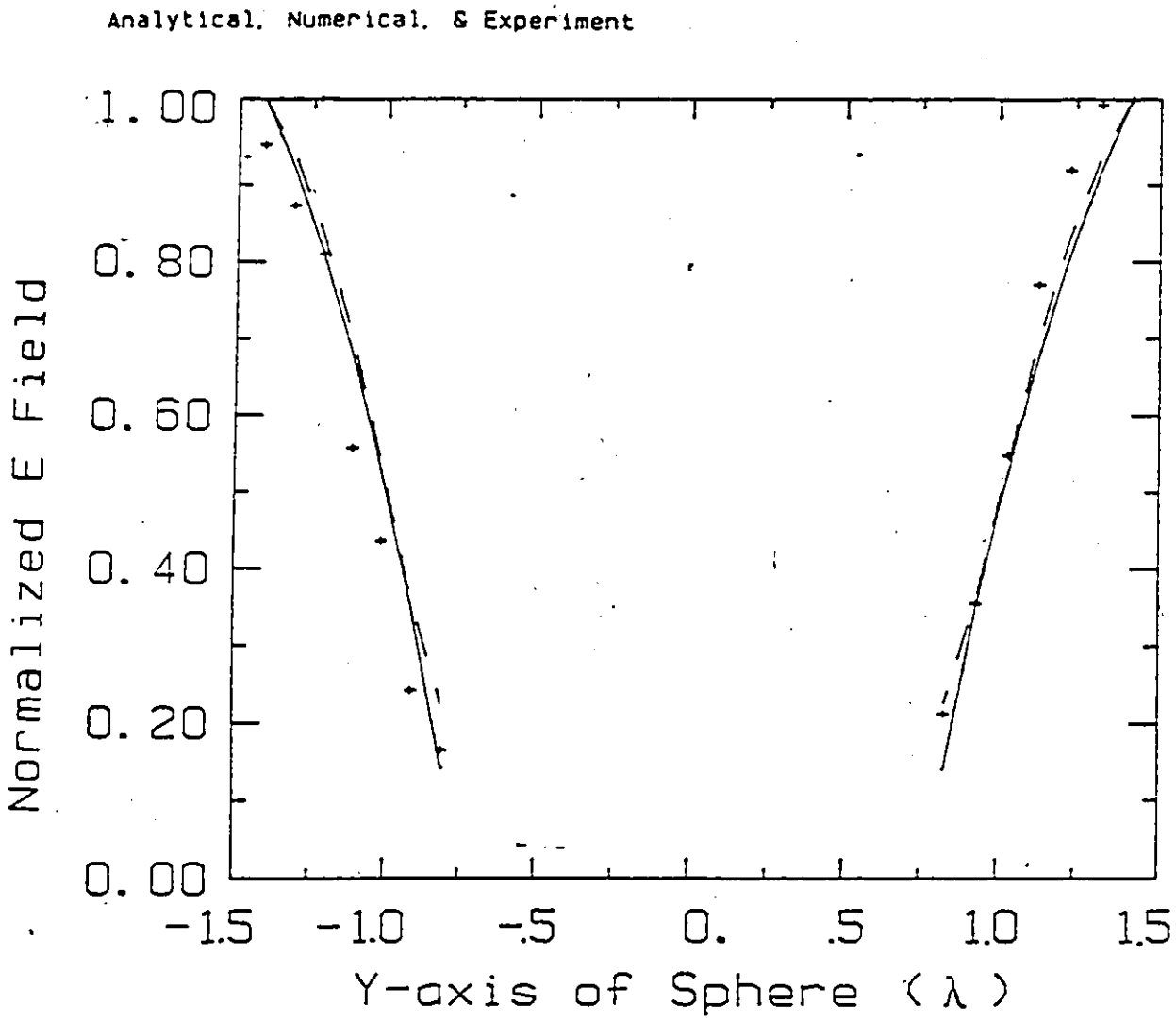

Fig 5.10 Comparison in normalized total electric field between the different methods.

(points on the Y-axis)
Experimental result +, eigenmode expansion ‾ , numerical computation – –.

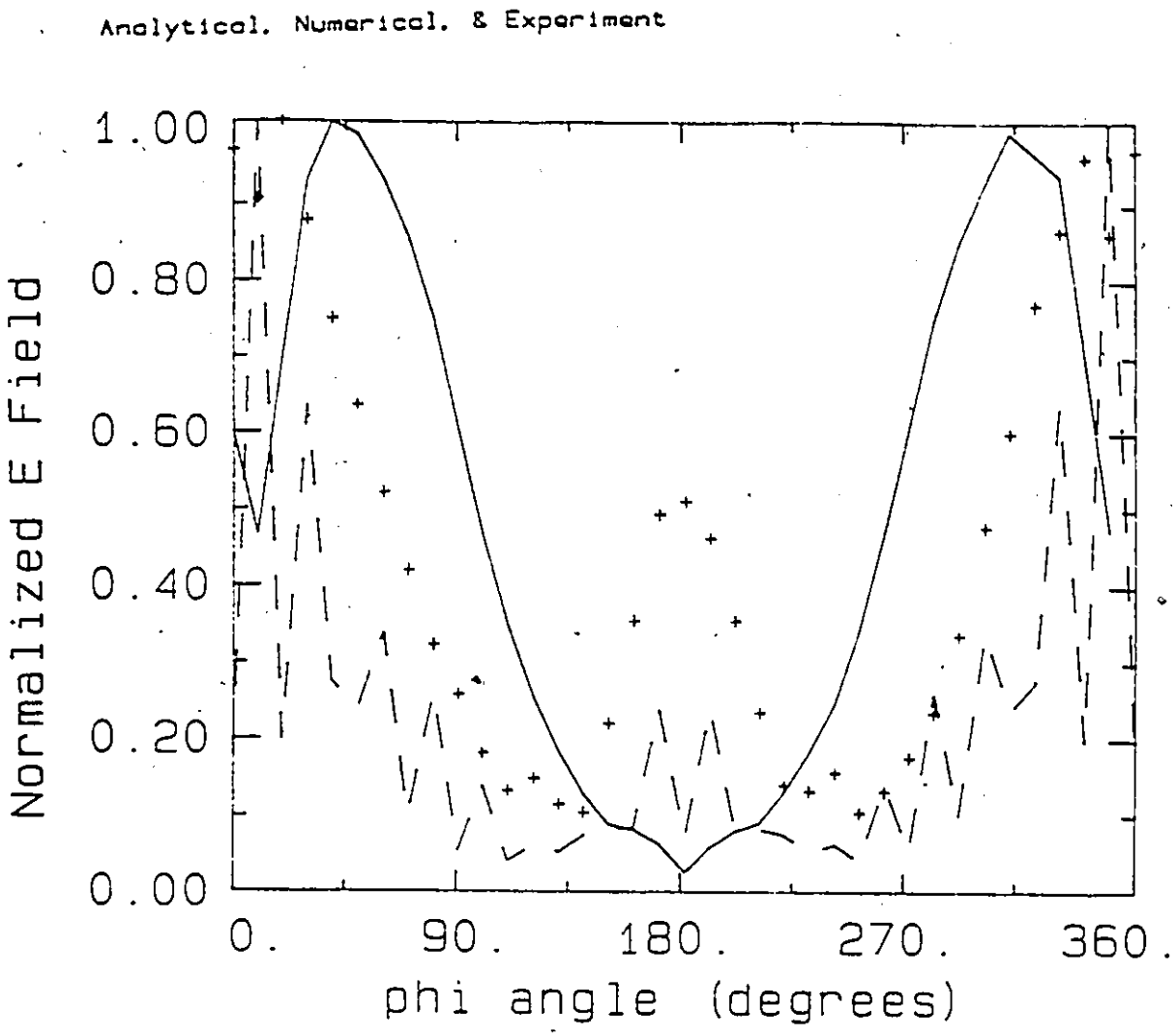

Fig 5.11 Comparison in normalized total electric field between the different methods. (points around the sphere)
Experimental result +, eigenmode expansion _ , numerical computation – –.

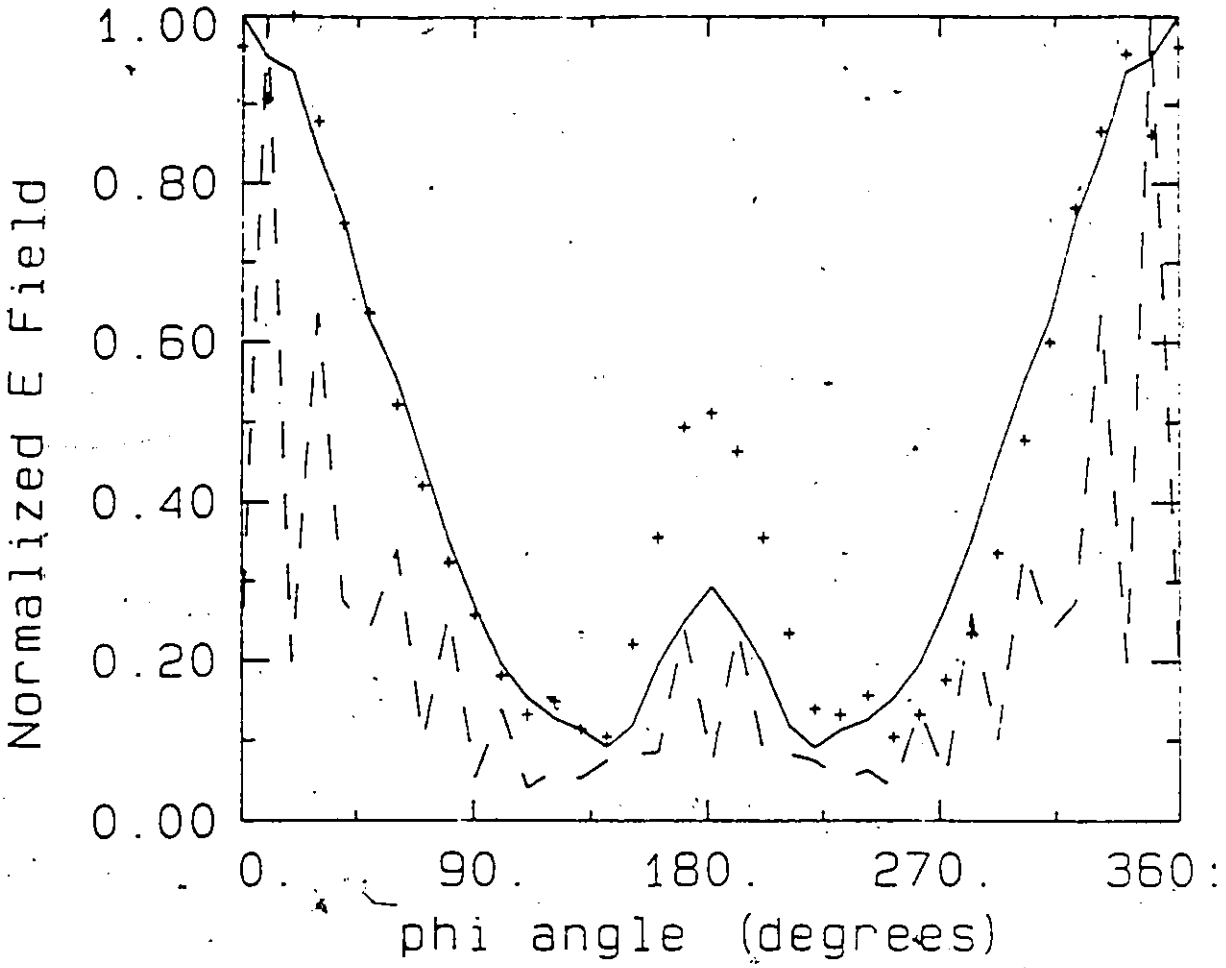

Fig 5.12 Comparison in normalized total electric field between experimental and numerical-results for different distances from the sphere. .
(points around the sphere)
Experimental result +, numerical computation, –– (0.5 cm from sphere), _ (1.5 cm form sphere).

CHAPTER 6

CONCLUSIONS & COMMENTS

The problem of radiating and scattering structures above an imperfect ground was investigated. The general problem cannot be solved analytically and therefore numerical methods must be used. Two numerical methods based on the Sommerfeld integrals and on the Frensel's reflection coefficient were described in chapter 2. It is explained that the Frensel's reflection coefficient is the most computationally efficient, at the price of a reduced accuracy, as compared to the Sommerfeld integrals approach. Thus, it is useful for computer aided design procedures, where many parameters are involved. The Sommerfeld integrals approach can be used at the final stage of the design procedure or for cases where radiating structures are very near the ground, for which Fresnel's approach fails.

A software package (NEC) using the above methods was used to study the field computation and the performance of a simple wire-antenna configuration, which is part of a volumetric detection system. The specifications regarding this surveillance system were that it should be easily installed and deployed under various environmental conditions. Equivalent models of human and animals were replaced by conducting cylinders with an equivalent radar cross-section in order to insert their model into the software, for field computations. This is a crude approximation for the complex inhomogenrous structure of human. However, the result can be used as a preliminary study of the performance of the antenna system.

Numerical computation results in Chapter 3 showed that, among various combinations, the antenna system consisting of two vertically polarized halfwave dipoles is capable of best discriminating between the intrusion of standing (vertically oriented)

human beings against small animals. It is also capable, although with less margin, of detecting crawling (horizontally oriented) humans. On the other hand, the coverage of the system is less efficient in terms of radiation pattern as compared to a horizontally oriented bistatic system, especially in the presence of metallic structures. In this case, zero radiation patterns occur at different angles, which precludes a hemispherical coverage. Also, it was found that the earth constitutive parameters affect the field strength in the practical range but not the radiation pattern in a significant manner. Finally, it is felt that a complementory system such as leaky cables, should be added to enhance the coverage at grazing angles.

The method used for numerical computations was applied for testing the validity of scaled down models for which near scattered field measurements were performed in an anechoic chamber. It was found that for observation points very near the scatterer ($1/20\lambda$), discrepancies occurred between the experimental measurements and numerical computations. The latter displayed oscillations which were subsequently confirmed to be produced by numerical instabilities.

In order to confirm the above conclusion concerning the numerical method, a new analytical solution based on spherical eigenmode expansion was developed. The analytical solution was found to yield stable solutions, even very near the scatterer. Comparisons with measurements showed that proximity of the scatterer probably influences the antenna probe feed points. However, for observation points located at distances larger than $1/5\lambda$ from the scatterer, discrepancies tend to disappear and the three methods agree remarkably well.

Finally, this study has shown that the software package that analyses antenna systems and scattering structures above imperfect grounds is very efficient and enables an optimization of simple antenna systems in realistic conditions. However, numerical instabilities may occur for observation points within a small fraction of a wavelength from radiating objects. The analytical solution presented here is a

closed-form solution which utilizes eigenmode expansion. It has been found stable and to converge rapidly. In addition, it is not restricted to simple scatterer but can be extended to more complex sources (e.g. near field) or scatterers. Nevertheless, the results found here can be used for future work as a reference.

APPENDIX

Spherical eigenmode expansion for an offcenter point source

The spherical wave expansion of an offcenter point source at $A(r_s, \theta_s, \phi_s)$ derived in chapter 5 is:

$$h_0^{(2)}(kR) = \frac{e^{-jkR}}{-jkR} = \sum_{n=0}^{\infty}(2n+1)h_n^{(2)}(kr_s)j_n(kr)P_n(\cos\gamma) \quad (r < r_s)$$
$$= \sum_{n=0)}^{\infty}(2n+1)h_n^{(2)}(kr)j_n(kr_s)P_n(\cos\gamma) \quad (r > r_s) \qquad (A.1)$$

where $h_0^{(2)}(kR)$ is symmetrical with respect to r_s and r, and the Associate Legendre Polynomials $P_n^m(\cos\theta)$ are given by:

$$P_n(\cos\gamma) = \sum_{m=0}^{n}\epsilon_m \frac{(n-m)!}{(n+m)!}P_n^m(\cos\theta)P_n^m(\cos\theta_s)\cos m(\phi-\phi_s)$$

$\epsilon_m = 1$, if $m = 0$, and $\epsilon_m = 2$ otherwise. $j_n(\rho)$ and $h_n^{(2)}(\rho)$ are Spherical Bessel Functions and are related to the Bessel function by $j_n(\rho) = (\frac{\pi}{2\rho})^{1/2}J_{n+\frac{1}{2}}^{(2)}(\rho)$ and $h_n^{(2)}(\rho) = (\frac{\pi}{2\rho})^{1/2}H_{n+\frac{1}{2}}^{(2)}(\rho)$.

Consider the case where $r < r_s$. Defining the spherical wave point source mentioned above as a function f and following the procedure in [2] one can determine three independent orthogonal vector wave solutions L,M,N. Since the divergence of the electric field is zero , and L is a purely longitudinal field, the vector solution can be expressed in term of M,N alone. Where

$$M_r = 0, \qquad M_\theta = \frac{1}{\sin\theta}\frac{\partial f}{\partial\phi}, \qquad M_\phi = -\frac{\partial f}{\partial\theta},$$

and

$$N_r = \frac{n(n+1)}{kr}f, \qquad N_\theta = \frac{1}{kr}\frac{\partial^2(rf)}{\partial r\partial\theta}, \qquad N_\phi = \frac{1}{kr\sin\theta}\frac{\partial^2(rf)}{\partial r\partial\phi}. \qquad (A.2)$$

The electric field generated from a spherical symmetrical point source $e^{\frac{-jkR}{-jkR}}$ in vector form is expressed in terms of spherical wave expansion functions as follows:

$$\mathbf{E}_{inc} = \mathbf{M} + \mathbf{N}$$

where the components of M and N are

$$\begin{aligned}
M_r &= 0, \\
M_\theta &= -\sum_{n=0}^{\infty}(2n+1)h_n^{(2)}(kr_s)j_n(kr) \\
&\quad \sum_{m=0}^{n}\epsilon_m m\frac{(n-m)!}{(n+m)!}P_n^m(\cos\theta_s)\frac{P_n^m(\cos\theta)}{\sin\theta}\sin m(\phi-\phi_s), \\
M_\phi &= -\sum_{n=0}^{\infty}(2n+1)h_n^{(2)}(kr_s)j_n(kr) \\
&\quad \sum_{m=0}^{n}\epsilon_m\frac{(n-m)!}{(n+m)!}P_n^m(\cos\theta_s)\frac{\partial}{\partial\theta}[P_n^m(\cos\theta)]\cos m(\phi-\phi_s). \\
N_r &= \sum_{n=0}^{\infty}(2n+1)(n)(n+1)h_n^{(2)}(kr_s)\frac{j_n(kr)}{kr} \\
&\quad \sum_{m=0}^{n}\epsilon_m\frac{(n-m)!}{(n+m)!}P_n^m(\cos\theta_s)P_n^m(\cos\theta)\cos m(\phi-\phi_s), \\
N_\theta &= \sum_{n=0}^{\infty}(2n+1)h_n^{(2)}(kr_s)\frac{[krj_n(kr)]'}{kr} \\
&\quad \sum_{m=0}^{n}\epsilon_m\frac{(n-m)!}{(n+m)!}P_n^m(\cos\theta_s)\frac{\partial}{\partial\theta}[P_n^m(\cos\theta)]\cos m(\phi-\phi_s), \\
N_\phi &= -\sum_{n=0}^{\infty}(2n+1)h_n^{(2)}(kr_s)\frac{[krj_n(kr)]'}{kr} \\
&\quad \sum_{m=0}^{n}\epsilon_m m\frac{(n-m)!}{(n+m)!}P_n^m(\cos\theta_s)\frac{P_n^m(\cos\theta)}{\sin\theta}\sin m(\phi-\phi_s).
\end{aligned} \tag{A.3}$$

The scattered electric field formed by the induced current on the conducting sphere surface can also be expressed in terms a set of spherical wave functions,

$$\mathbf{E}_{scat} = \sum_{n=0}^{\infty} a_n^r m_0 + b_n^r n_0$$

where

$$
\begin{aligned}
E_{scat\ r} &= \sum_{n=0}^{\infty}\sum_{m=0}^{n} b_n^r(n)(n+1)\frac{h_n^{(2)}(kr)}{kr}p_n^m(\cos\theta)\cos m\phi, \\
E_{scat\ \theta} &= \sum_{n=0}^{\infty}\sum_{m=0}^{n} a_n^r[-mh_n^{(2)}(kr)\frac{P_n^m(\cos\theta)}{\sin\theta}\sin m\phi] \\
&\quad + b_n^r[\frac{[krh_n^{(2)}(kr)]'}{kr}\frac{\partial}{\partial\theta}[P_n^m(\cos\theta)]\cos m\phi], \\
E_{scat\ \phi} &= \sum_{n=0}^{\infty}\sum_{m=0}^{n} a_n^r[-h_n^{(2)}(kr)\frac{\partial}{\partial\theta}[P_n^m(\cos\theta)]\cos m\phi] \\
&\quad + b_n^r[-m\frac{[krh_n^{(2)}(kr)]'}{kr}\frac{P_n^m(\cos\theta)}{\sin\theta}\sin m\phi]
\end{aligned}
\tag{A.4}
$$

Applying the boundary condition, i.e. the total tangential electric field is zero at $r = a$, where a is the radius of the sphere, onto the surface of the sphere yields

$$
\begin{aligned}
E_{inc_\theta} + E_{scat_\theta} &= 0 \\
E_{inc_\phi} + E_{scat_\phi} &= 0
\end{aligned}
\tag{A.5}
$$

The incident electric field and scattered electric field components in the $\theta-$direction at $r = a$ can be found by substituting r with a in the equations,

$$
\begin{aligned}
E_{inc_\theta}|_{r=a} &= \sum_{n=0}^{\infty}\sum_{m=0}^{n} \epsilon_m(2n+1)\frac{(n-m)!}{(n+m)!}h_n^{(2)}(kr_s)P_n^m(\cos\theta_s) \\
&\quad [-mj_n(ka)\frac{P_n^m(\cos\theta)}{\sin\theta}\sin m(\phi-\phi_s) \\
&\quad + \frac{[kaj_n(ka)]'}{ka}\frac{\partial}{\partial\theta}[P_n^m(\cos\theta)]\cos m(\phi-\phi_s)] \\
E_{scat\ \theta}|_{r=a} &= \sum_{n=0}^{\infty}\sum_{m=0}^{n} a_n^r[-mh_n^{(2)}(ka)\frac{P_n^m(\cos\theta)}{\sin\theta}\sin m\phi] \\
&\quad + b_n^r[\frac{[kah_n^{(2)}(ka)]'}{ka}\frac{\partial}{\partial\theta}[P_n^m(\cos\theta)]\cos m\phi],
\end{aligned}
\tag{A.6}
$$

Similarly, the ϕ components are:

$$
\begin{aligned}
E_{inc_\phi}|_{r=a} = & \sum_{n=0}^{\infty}\sum_{m=0}^{n} \epsilon_m (2n+1)\frac{(n-m)!}{(n+m)!} h_n^{(2)}(kr_s) P_n^m(\cos\theta_s) \\
& [-j_n(ka)\frac{\partial}{\partial\theta}[P_n^m(\cos\theta)]\cos m(\phi-\phi_s) \\
& - m\frac{[kaj_n(ka)]'}{ka}\frac{P_n^m(\cos\theta)}{\sin\theta}\sin m(\phi-\phi_s)] \\
E_{scat\ \phi}|_{r=a} = & \sum_{n=0}^{\infty}\sum_{m=0}^{n} a_n^r[-h_n^{(2)}(ka)\frac{\partial}{\partial\theta}[P_n^m(\cos\theta)]\cos m\phi] \\
& + b_n^r[-m\frac{[kah_n^{(2)}(kr)]'}{ka}\frac{P_n^m(\cos\theta)}{\sin\theta}\sin m\phi]
\end{aligned}
\tag{A.7}
$$

Since the sphere is symmetric with respect to the ϕ angle, one can always line up the source point with an axis in order to simplify the matching. In this case, taking $\phi_s = 0$, the boundary condition at $r = a$ at θ direction becomes,

$$
\begin{aligned}
& E_{inc_\theta}|_{r=a} = -E_{scat_\theta}|_{r=a} \\
& \sum_{n=0}^{\infty}\sum_{m=0}^{n} \epsilon_m (2n+1)\frac{(n-m)!}{(n+m)!} h_n^{(2)}(kr_s) P_n^m(\cos\theta_s) \\
& \{-mj_n(ka)\frac{P_n^m(\cos\theta)}{\sin\theta}\sin m\phi + \frac{[kaj_n(ka)]'}{ka}\frac{\partial}{\partial\theta}[P_n^m(\cos\theta)]\cos m\phi\} \\
= & -\{\sum_{n=0}^{\infty}\sum_{m=0}^{n} a_n^r[-mh_n^{(2)}(ka)\frac{P_n^m(\cos\theta)}{\sin\theta}\sin m\phi] \\
& + b_n^r[\frac{[kah_n^{(2)}(ka)]'}{ka}\frac{\partial}{\partial\theta}[P_n^m(\cos\theta)]\cos m\phi]\}
\end{aligned}
\tag{A.8}
$$

and also for the tangential electric fields at ϕ direction is:

$$
\begin{aligned}
& E_{inc_\phi}|_{r=a} = -E_{scat_\phi}|_{r=a} \\
& \sum_{n=0}^{\infty}\sum_{m=0}^{n} \epsilon_m (2n+1)\frac{(n-m)!}{(n+m)!} h_n^{(2)}(kr_s) P_n^m(\cos\theta_s) \\
& \{-j_n(ka)\frac{\partial}{\partial\theta}[P_n^m(\cos\theta)]\cos m\phi - m\frac{[kaj_n(ka)]'}{ka}\frac{P_n^m(\cos\theta)}{\sin\theta}\sin m\phi\} \\
= & -\{\sum_{n=0}^{\infty}\sum_{m=0}^{n} a_n^r[-h_n^{(2)}(ka)\frac{\partial}{\partial\theta}[P_n^m(\cos\theta)]\cos m\phi] \\
& + b_n^r[-m\frac{[kah_n^{(2)}(kr)]'}{ka}\frac{P_n^m(\cos\theta)}{\sin\theta}\sin m\phi]\}
\end{aligned}
\tag{A.9}
$$

This is a set of two inhomogeneous equations with two unknowns, namely a_n^r and b_n^r. In order to find a_n^r, one has to eliminate b_n^r. First, the equation (A.8), which involves E_θ, is multipied by $m\frac{P_n^m(\cos\theta)}{\sin\theta}\sin m\phi$, and the equation (A.9), which involves E_ϕ, is multipied by $\frac{\partial}{\partial\theta}P_n^m(\cos\theta)\cos m\phi$. The two equations are added together, and the terms with b_n^r are subtracted, leaving only a_n^r:

$$
\begin{aligned}
&-\{\sum_{n=0}^{\infty}\sum_{m=0}^{n} a_n^r[-m^2 h_n^{(2)}(ka)(\frac{P_n^m(\cos\theta)}{\sin\theta})^2\sin^2 m\phi \\
&-h_n^{(2)}(ka)(\frac{\partial}{\partial\theta}[P_n^m(\cos\theta)])^2\cos m^2\phi]\}, \\
&=\sum_{n=0}^{\infty}\sum_{m=0}^{n}\epsilon_m(2n+1)\frac{(n-m)!}{(n+m)!}h_n^{(2)}(kr_s)P_n^m(\cos\theta_s) \\
&[-m^2 j_n(ka)(\frac{P_n^m(\cos\theta)}{\sin\theta})^2\sin^2 m\phi - j_n(ka)(\frac{\partial}{\partial\theta}P_n^m(\cos\theta))^2\cos m^2\phi \\
&+m\frac{[kaj_n(ka)]'}{ka}\frac{P_n^m(\cos\theta)}{\sin\theta}\frac{\partial}{\partial\theta}[P_n^m(\cos\theta)]\sin m\phi\cos m\phi \\
&-m\frac{[kaj_n(ka)]'}{ka}\frac{P_n^m(\cos\theta)}{\sin\theta}\frac{\partial}{\partial\theta}[P_n^m(\cos\theta)]\sin m\phi\cos m\phi]
\end{aligned}
\tag{A.10}
$$

Equation (A.10) then becomes

$$
\begin{aligned}
&\sum_{n=0}^{\infty}\sum_{m=0}^{n} a_n^r h_n^{(2)}(ka)[m^2(\frac{P_n^m(\cos\theta)}{\sin\theta})^2\sin^2 m\phi+(\frac{\partial}{\partial\theta}[P_n^m(\cos\theta)])^2\cos m^2\phi] \\
&=\sum_{n=0}^{\infty}\sum_{m=0}^{n}\epsilon_m(2n+1)\frac{(n-m)!}{(n+m)!}h_n^{(2)}(kr_s)P_n^m(\cos\theta_s)j_n(ka)(-1) \\
&[m^2(\frac{P_n^m(\cos\theta)}{\sin\theta})^2\sin^2 m\phi+(\frac{\partial}{\partial\theta}[P_n^m(\cos\theta)])^2\cos m^2\phi]
\end{aligned}
\tag{A.11}
$$

Therefore,

$$
a_n^r=-\sum_{n=0}^{\infty}(2n+1)h_n^{(2)}(kr_s)\frac{j_n(ka)}{h_n^{(2)}(ka)}\sum_{m=0}^{n}\epsilon_m\frac{(n-m)!}{(n+m)!}P_n^m(\cos\theta_s). \tag{A.12}
$$

Similarly, b_n^r can be found by multiplying (A.9) by $\frac{\partial}{\partial\theta}[P_n^m(\cos\theta)]\cos m\phi$, and (A.10)

by $m\frac{P_n^m(\cos\theta)}{\sin\theta}\sin m\phi$, and then subtract the two equations,

$$
\begin{aligned}
&-\{\sum_{n=0}^{\infty}\sum_{m=0}^{n} b_n^r[(\frac{[kah_n^{(2)}(ka)]'}{ka})(\frac{\partial}{\partial\theta}[P_n^m(\cos\theta)])^2\cos^2 m\phi \\
&-m^2\frac{[kah_n^{(2)}(ka)]'}{ka}(\frac{P_n^m(\cos\theta)}{\sin\theta})^2\sin m^2\phi]\}, \\
&=\sum_{n=0}^{\infty}\sum_{m=0}^{n}\epsilon_m(2n+1)\frac{(n-m)!}{(n+m)!}h_n^{(2)}(kr_s)P_n^m(\cos\theta_s) \qquad (A.13)\\
&[\frac{[kaj_n(ka)]'}{ka}(\frac{\partial}{\partial\theta}[P_n^m(\cos\theta)])^2\cos^2 m\phi+m^2\frac{[kaj_n(ka)]'}{ka}(\frac{P_n^m(\cos\theta)}{\sin\theta})^2\sin m^2\phi \\
&-mj_n(ka)\frac{P_n^m(\cos\theta)}{\sin\theta}\frac{\partial}{\partial\theta}[P_n^m(\cos\theta)]\sin m\phi\cos m\phi \\
&+mj_n(ka)\frac{P_n^m(\cos\theta)}{\sin\theta}\frac{\partial}{\partial\theta}[P_n^m(\cos\theta)]\sin m\phi\cos m\phi]
\end{aligned}
$$

Then equation (A.13) simplifies to;

$$
\begin{aligned}
&\sum_{n=0}^{\infty}\sum_{m=0}^{n} b_n^r\frac{[kah_n^{(2)}(ka)]'}{ka}[(\frac{\partial}{\partial\theta}[P_n^m(\cos\theta)])^2\cos^2 m\phi+m^2(\frac{P_n^m(\cos\theta)}{\sin\theta})^2\sin m^2\phi], \\
&=\sum_{n=0}^{\infty}\sum_{m=0}^{n}\epsilon_m(2n+1)\frac{(n-m)!}{(n+m)!}h_n^{(2)}(kr_s)P_n^m(\cos\theta_s)\frac{[kaj_n(ka)]'}{ka} \qquad (A.14)\\
&[(\frac{\partial}{\partial\theta}[P_n^m(\cos\theta)])^2\cos^2 m\phi+m^2(\frac{P_n^m(\cos\theta)}{\sin\theta})^2\sin m^2\phi]
\end{aligned}
$$

Similarly b_n^r is obtained as:

$$
b_n^r=-\sum_{n=0}^{\infty}(2n+1)h_n^{(2)}(kr_s)\frac{[kaj_n(ka)]'}{[kah_n^{(2)}(ka)]'}\sum_{m=0}^{n}\epsilon_m\frac{(n-m)!}{(n+m)!}P_n^m(\cos\theta_s) \qquad (A.15)
$$

```
C
C                    MAIN  PROGRAM
C
C To evaluate the total electric field scattered by
C a perfect conducting sphere.  The incident electric
C field is the field generated by a offcentered point
C source.  The wavefront of the point source is
C constant in phase and magnitude.  The approximation
C of the spherical wave is a summation of spherical
C wave functions.  They consists of spherical Bessel
C function, and Associate Legendre Polynomials.
C
C
      IMPLICIT REAL*8 (A-H,O-Z)
      COMPLEX*16 ESRAD,ESTHETA,ESPHI,ZKRJ,ZKEX,EINC,
     +           ESCAT2,ESCAT,ETOL,
     +           ETOL2,EIRAD,EITHETA,EIPHI,EINC2
      INTEGER*4 N
      CHARACTER*12 FILENAME,FILENAME1,FILENAME2
      WRITE (2,10)
   10 FORMAT (/,2X,'ETOL DATA FILENAME>',$)
      READ (1,'(a)') FILENAME
      OPEN (12,FILE=FILENAME,STATUS='NEW')
      WRITE (2,11)
   11 FORMAT (/,2X,'ESCAT DATA FILENAME>',$)
      READ (1,'(a)') FILENAME1
      OPEN (11,FILE=FILENAME1,STATUS='NEW')
      WRITE (2,12)
   12 FORMAT (/,2X,'EINC DATA FILENAME>',$)
      READ (1,'(a)') FILENAME2
      OPEN (10,FILE=FILENAME2,STATUS='NEW')
C
C Input of summation number 'N', this is the maximum
C number that the summation would go.  The individual
C summation under is determine by the convergence factor
C input later on
C
      WRITE (2,*) 'N?'
      READ (1,*) N
C
C Input the rectangular coordinates of the source point
C
      WRITE (2,*) 'X1,Y1,Z1?'
      READ (1,*) X1,Y1,Z1
C
C Input the radius of the conducting sphere
C
      WRITE (2,*) 'RP?(RADIUS OF SPHERE?)IN METER'
      READ (1,*) RP
C
C Input the radius of the measuring points
C
      WRITE (2,*) 'SS?'
      READ (1,*) SS
      PI=DACOS(-1.0D0)
C
C Format for plotting graphs of the output data file
C
      WRITE (10,701)
  701 FORMAT (T1,'Ei vs PHI')
```

```
      WRITE (10,702)
 702  FORMAT (T1,'.HL = PHI')
      WRITE (10,703)
 703  FORMAT (T1,'.VL = EP')
      WRITE (10,704)
 704  FORMAT (T1,'----------------------')
      WRITE (11,801)
 801  FORMAT (T1,'Es vs PHI')
      WRITE (11,802)
 802  FORMAT (T1,'.HL = PHI')
      WRITE (11,803)
 803  FORMAT (T1,'.VL = EP')
      WRITE (11,804)
 804  FORMAT (T1,'----------------------')
      WRITE (12,901)
 901  FORMAT (T1,'Et vs PHI')
      WRITE (12,902)
 902  FORMAT (T1,'.HL = PHI')
      WRITE (12,903)
 903  FORMAT (T1,'.VL = EM')
      WRITE (12,904)
 904  FORMAT (T1,'----------------------')
C
C Input the frequency of operation, and convergence factor
C
      WRITE (2,*) 'FREQ?(Hz), CONVERGENCE FACTOR?'
      READ (1,*) FREQ, CONV
C
C Compute the value of propagating constant beta (k)
C
      E0=8.8542D-012
      U0=4.0D-7*PI
      OMEGA=2.0D0*PI*FREQ
      ZK=OMEGA*DSQRT(U0*E0)
C
C Compute the spherical coordinates of the source point
C
      RS2=X1**2+Y1**2+Z1**2
      RS=DSQRT(RS2)
      THETAS=DACOS(Z1/RS)
      IF (X1 .NE. 0.0D0) THEN
         W1=DABS(Y1/X1)
         PHIS=DATAN(W1)
         IF (X1 .LT. 0.0D0 .AND. Y1 .GT. 0.0D0) PHIS=PI-PHIS
         IF (X1 .LT. 0.0D0 .AND. Y1 .LT. 0.0D0) PHIS=PI+PHIS
         IF (X1 .GT. 0.0D0 .AND. Y1 .LT. 0.0D0) PHIS=-PHIS
         IF (X1 .LT. 0.0D0 .AND. Y1 .EQ. 0.0D0) PHIS=PI
      ELSE
         PHIS=PI/2.0D0
         IF (Y1 .LT. 0.0D0) PHIS=-PI/2.0D0
      END IF
C
C Compute ks, kp, cos(theta s), and sin(theta s)
C
      XKS=ZK*RS
      XKP=ZK*RP
      XS=DCOS(THETAS)
      XSS=DSIN(THETAS)
C
C The observation points are compute in a loop of 36 points
```

```
C around the sphere
C
      DO 9999 K=1,36
C
C Compute the spherical coordinates of the observation points
C
          A=(K-1)*10.0D0
          RO2=SS**2+0.008**2
          RO=DSQRT(RO2)
          THETAO=DACOS(0.008/RO)
          PHIO=(K-1)*PI/18.0D0
C
C Compute ko, cos(theta o), and sin(theta o)
C
          XKO=ZK*RO
          XO=DCOS(THETAO)
          XOS=DSIN(THETAO)
C
C The three components of the incident electric field
C
          CALL ERAD1 (N,XKS,XKO,XS,XSS,XO,XOS,PHIS,PHIO,
     +                RS,RO,CONV,EIRAD)
          CALL ETHETA1 (N,XKS,XKO,XS,XSS,XO,XOS,PHIS,PHIO,
     +                  RS,RO,CONV,EITHETA)
          CALL EPHI1 (N,XKS,XKO,XS,XSS,XO,XOS,PHIS,PHIO,
     +                RS,RO,CONV,EIPHI)
C
C The three components of the scattered electric field
C
          CALL ERAD2 (N,XKS,XKO,XKP,XS,XSS,XO,XOS,PHIS,PHIO,
     +                RS,RO,CONV,ESRAD)
          CALL ETHETA2 (N,XKS,XKO,XKP,XS,XSS,XO,XOS,PHIS,PHIO,
     +                  RS,RO,CONV,ESTHETA)
          CALL EPHI2 (N,XKS,XKO,XKP,XS,XSS,XO,XOS,PHIS,PHIO,
     +                RS,RO,CONV,ESPHI)
C
C The incident electric field
C
          EINC2=(EIRAD)**2+(EITHETA)**2+(EIPHI)**2
          EINC=CDSQRT(EINC2)
          EINCM=CDABS(EINC)
          WRITE (10,*) A,EINCM
C
C The scattered electric field
C
          ESCAT2=(ESRAD)**2+(ESTHETA)**2+(ESPHI)**2
          ESCAT=CDSQRT(ESCAT2)
          ESCATM=CDABS(ESCAT)
          WRITE (11,*) A,ESCATM
C
C The total electric field
C
          ETOL2=(EIRAD+ESRAD)**2+(EITHETA+ESTHETA)**2
     +          +(EIPHI+ESPHI)**2
          ETOL=CDSQRT(ETOL2)
          ETOLM=CDABS(ETOL)
          WRITE (12,*) A,ETOLM
9999    CONTINUE
        STOP
        END
```

```
C
C A series of six main subroutines to evaluate the individual
C spherical components of the incident and scattered waves
C
C Main subroutine to compute the r component of incident field
C
      SUBROUTINE ERAD1 (N,XKS,XKO,XS,XSS,XO,XOS,PHIS,PHIO,
     +                  RS,RO,CONV,EIRAD)
      IMPLICIT REAL*8 (A-H,O-Z)
      COMPLEX*16 HNS,HNO,RADNI,EIRAD1,EIRAD,ABC1,ABD1
      DIMENSION BJS(82),BJO(82)
      CALL BEJH (XKO,N,BJO)
      CALL BEJH (XKS,N,BJS)
      EIRAD1=DCMPLX(0.0D0,0.0D0)
      DO 1001 I=0,N
         ABC1=EIRAD1
         CALL HN (XKS,I,HNS)
         CALL HN (XKO,I,HNO)
         IF (RO .LT. RS) THEN
            RADNI=I*(I+1)*(2.0*I+1)*HNS*(BJO(I+1)/XKO)
         ELSE
            RADNI=I*(I+1)*(2.0*I+1)*BJS(I+1)*(HNO/XKO)
         END IF
         SUMNR=0.0D0
         DO 2001 J=0,I
            EMFA=EMFACT(J,I)
            PMNS=PLGNDR(I,J,XS)
            PMNO=PLGNDR(I,J,XO)
            RPHI=J*(PHIO-PHIS)
            RADNJ=EMFA*PMNS*PMNO*DCOS(RPHI)
            SUMNR=SUMNR+RADNJ
2001     CONTINUE
         EIRAD1=EIRAD1+(RADNI*SUMNR)
         ABD1=EIRAD1
         IF (I .EQ. 0) ABD1=1.0D0
         ABE1=CDABS((ABD1-ABC1)/ABD1)
         IF (ABE1 .LT. CONV) GOTO 1231
1001  CONTINUE
1231  EIRAD=EIRAD1
      RETURN
      END
C
C
C Main subroutine to compute the r component of scattered field
C
C
      SUBROUTINE ERAD2 (N,XKS,XKO,XKP,XS,XSS,XO,XOS,PHIS,PHIO,
     +                  RS,RO,CONV,ESRAD)
      IMPLICIT REAL*8 (A-H,O-Z)
      COMPLEX*16 HNS,HNO,RADNI,ARN,BRN,ESRAD1,ESRAD,ABC1,ABD1
      DIMENSION BJS(82),BJO(82)
      CALL BEJH (XKO,N,BJO)
      CALL BEJH (XKS,N,BJS)
      ESRAD1=DCMPLX(0.0D0,0.0D0)
      DO 1001 I=0,N
         ABC1=ESRAD1
         CALL HN (XKS,I,HNS)
         CALL HN (XKO,I,HNO)
         CALL RN (XKP,I,ARN,BRN)
         IF (RO .LT. RS) THEN
```

```
            RADNI=I*(I+1)*(2.0*I+1)*HNS*(HNO/XKO)*BRN
         ELSE
            RADNI=I*(I+1)*(2.0*I+1)*BJS(I+1)*(HNO/XKO)*BRN
         END IF
         SUMNR=0.0D0
         DO 2001 J=0,I
            EMFA=EMFACT(J,I)
            PMNS=PLGNDR(I,J,XS)
            PMNO=PLGNDR(I,J,XO)
            RPHI=J*(PHIO-PHIS)
            RADNJ=EMFA*PMNS*PMNO*DCOS(RPHI)
            SUMNR=SUMNR+RADNJ
2001     CONTINUE
         ESRAD1=ESRAD1+(RADNI*SUMNR)
         ABD1=ESRAD1
         IF (I .EQ. 0) ABD1=1.0D0
         ABE1=CDABS((ABD1-ABC1)/ABD1)
         IF (ABE1 .LT. CONV) GOTO 1231
1001  CONTINUE
1231  ESRAD=ESRAD1
      RETURN
      END
C
C
C Main subroutine to compute the theta component of incident field
C
C
      SUBROUTINE ETHETA1 (N,XKS,XKO,XS,XSS,XO,XOS,PHIS,PHIO,
     +                    RS,RO,CONV,EITHETA)
      IMPLICIT REAL*8 (A-H,O-Z)
      COMPLEX*16 HNS,HNO,HNOD,EITHETA2,EITHETA,ABC2,ABD2,
     +           THAMI,THANI
      DIMENSION BJS(82),BJO(82)
      CALL BEJH (XKO,N,BJO)
      CALL BEJH (XKS,N,BJS)
      EITHETA2=DCMPLX(0.0D0,0.0D0)
      DO 1002 I=0,N
         ABC2=EITHETA2
         CALL HN (XKS,I,HNS)
         CALL HN (XKO,I,HNO)
         CALL BNOD (XKO,I,BJOD)
         CALL HND (XKO,I,HNOD)
         IF (RO .LT. RS) THEN
            THAMI=(2.0*I+1)*HNS*BJO(I+1)
            THANI=(2.0*I+1)*HNS*(BJOD/XKO)
         ELSE
            THAMI=(2.0*I+1)*BJS(I+1)*HNO
            THANI=(2.0*I+1)*BJS(I+1)*(HNOD/XKO)
         END IF
         SUMMT=0.0D0
         SUMNT=0.0D0
         DO 2002 J=0,I
            EMFA=EMFACT(J,I)
            PMNS=PLGNDR(I,J,XS)
            PMNO=PLGNDR(I,J,XO)
            PMNOD=PLGNDR(I,J+1,XO)
            IF (XOS .EQ. 0.0D0) THEN
               PMNOS=PS(I,J,XO)
            ELSE
               PMNOS=PMNO/XOS
```

```
            END IF
            RPHI=J*(PHIO-PHIS)
            THAMJ=EMFA*PMNS*PMNOS*(-J)*DSIN(RPHI)
            THANJ=EMFA*PMNS*PMNOD*DCOS(RPHI)
            SUMMT=SUMMT+THAMJ
            SUMNT=SUMNT+THANJ
 2002     CONTINUE
          EITHETA2=EITHETA2+(THAMI*SUMMT+THANI*SUMNT)
          ABD2=EITHETA2
          IF (I .EQ. 0) ABD2=1.0D0
          ABE2=CDABS((ABD2-ABC2)/ABD2)
          IF (ABE2 .LT. CONV) GOTO 1232
 1002   CONTINUE
 1232   EITHETA=EITHETA2
        RETURN
        END
C
C
C Main subroutine to compute the theta component of scattered field
C
C
        SUBROUTINE ETHETA2 (N,XKS,XKO,XKP,XS,XSS,XO,XOS,PHIS,PHIO,
     +                      RS,RO,CONV,ESTHETA)
        IMPLICIT REAL*8 (A-H,O-Z)
        COMPLEX*16 HNS,HNO,HNOD,ARN,BRN,ESTHETA2,ESTHETA,ABC2,ABD2,
     +             THAMI,THANI
        DIMENSION BJS(82),BJO(82)
        CALL BEJH (XKO,N,BJO)
        CALL BEJH (XKS,N,BJS)
        ESTHETA2=DCMPLX(0.0D0,0.0D0)
        DO 1002 I=0,N
           ABC2=ESTHETA2
           CALL HN (XKS,I,HNS)
           CALL HN (XKO,I,HNO)
           CALL BNOD (XKO,I,BJOD)
           CALL HND (XKO,I,HNOD)
           CALL RN (XKP,I,ARN,BRN)
           IF (RO .LT. RS) THEN
              THAMI=(2.0*I+1)*HNS*HNO*ARN
              THANI=(2.0*I+1)*HNS*(HNOD/XKO)*BRN
           ELSE
              THAMI=(2.0*I+1)*BJS(I+1)*HNO*ARN
              THANI=(2.0*I+1)*BJS(I+1)*(HNOD/XKO)*BRN
           END IF
           SUMMT=0.0D0
           SUMNT=0.0D0
           DO 2002 J=0,I
              EMFA=EMFACT(J,I)
              PMNS=PLGNDR(I,J,XS)
              PMNO=PLGNDR(I,J,XO)
              PMNOD=PLGNDR(I,J+1,XO)
              IF (XOS .EQ. 0.0D0) THEN
                 PMNOS=PS(I,J,XO)
              ELSE
                 PMNOS=PMNO/XOS
              END IF
              RPHI=J*(PHIO-PHIS)
              THAMJ=EMFA*PMNS*PMNOS*(-J)*DSIN(RPHI)
              THANJ=EMFA*PMNS*PMNOD*DCOS(RPHI)
              SUMMT=SUMMT+THAMJ
```

```
            SUMNT=SUMNT+THANJ
2002        CONTINUE
            ESTHETA2=ESTHETA2+(THAMI*SUMMT+THANI*SUMNT)
            ABD2=ESTHETA2
            IF (I .EQ. 0) ABD2=1.0D0
            ABE2=CDABS((ABD2-ABC2)/ABD2)
            IF (ABE2 .LT. CONV) GOTO 1232
1002     CONTINUE
1232     ESTHETA=ESTHETA2
         RETURN
         END
C
C
C Main subroutine to compute the phi component of incident field
C
C
         SUBROUTINE EPHI1 (N,XKS,XKO,XS,XSS,XO,XOS,PHIS,PHIO,
     +                     RS,RO,CONV,EIPHI)
         IMPLICIT REAL*8 (A-H,O-Z)
         COMPLEX*16 HNS,HNO,HNOD,EIPHI3,EIPHI,ABC3,ABD3,
     +              PHIMI,PHINI
         DIMENSION BJS(82),BJO(82)
         CALL BEJH (XKO,N,BJO)
         CALL BEJH (XKS,N,BJS)
         EIPHI3=DCMPLX(0.0D0,0.0D0)
         DO 1003 I=0,N
            ABC3=EIPHI3
            CALL HN (XKS,I,HNS)
            CALL HN (XKO,I,HNO)
            CALL BNOD (XKO,I,BJOD)
            CALL HND (XKO,I,HNOD)
            IF (RO .LT. RS) THEN
               PHIMI=(2.0*I+1)*HNS*BJO(I+1)
               PHINI=(2.0*I+1)*HNS*(BJOD/XKO)
            ELSE
               PHIMI=(2.0*I+1)*BJS(I+1)*HNO
               PHINI=(2.0*I+1)*BJS(I+1)*(HNOD/XKO)
            END IF
            SUMMP=0.0D0
            SUMNP=0.0D0
            DO 2003 J=0,I
               EMFA=EMFACT(J,I)
               PMNS=PLGNDR(I,J,XS)
               PMNO=PLGNDR(I,J,XO)
               PMNOD=PLGNDR(I,J+1,XO)
               IF (XOS .EQ. 0.0D0) THEN
                  PMNOS=PS(I,J,XO)
               ELSE
                  PMNOS=PMNO/XOS
               END IF
               RPHI=J*(PHIO-PHIS)
               PHIMJ=EMFA*PMNS*PMNOD*(-1)*DCOS(RPHI)
               PHINJ=EMFA*PMNS*PMNOS*(-J)*DSIN(RPHI)
               SUMMP=SUMMP+PHIMJ
               SUMNP=SUMNP+PHINJ
2003        CONTINUE
            EIPHI3=EIPHI3+(PHIMI*SUMMP+PHINI*SUMNP)
            ABD3=EIPHI3
            IF (I .EQ. 0) ABD3=1.0D0
            ABE3=CDABS((ABD3-ABC3)/ABD3)
```

```
          IF (ABE3 .LT. CONV) GOTO 1233
1003      CONTINUE
1233      EIPHI=EIPHI3
          RETURN
          END
C
C
C Main subroutine to compute the phi component of scattered field
C
C
          SUBROUTINE EPHI2 (N,XKS,XKO,XKP,XS,XSS,XO,XOS,PHIS,PHIO,
     +                      RS,RO,CONV,ESPHI)
          IMPLICIT REAL*8 (A-H,O-Z)
          COMPLEX*16 HNS,HNO,HNOD,ARN,BRN,ESPHI3,ESPHI,ABC3,ABD3,
     +               PHIMI,PHINI
          DIMENSION BJS(82),BJO(82)
          CALL BEJH (XKO,N,BJO)
          CALL BEJH (XKS,N,BJS)
          ESPHI3=DCMPLX(0.0D0,0.0D0)
          DO 1003 I=0,N
             ABC3=ESPHI3
             CALL HN (XKS,I,HNS)
             CALL HN (XKO,I,HNO)
             CALL BNOD (XKO,I,BJOD)
             CALL HND (XKO,I,HNOD)
             CALL RN (XKP,I,ARN,BRN)
             IF (RO .LT. RS) THEN
                PHIMI=(2.0*I+1)*HNS*HNO*ARN
                PHINI=(2.0*I+1)*HNS*(HNOD/XKO)*BRN
             ELSE
                PHIMI=(2.0*I+1)*BJS(I+1)*HNO*ARN
                PHINI=(2.0*I+1)*BJS(I+1)*(HNOD/XKO)*BRN
             END IF
             SUMMP=0.0D0
             SUMNP=0.0D0
             DO 2003 J=0,I
                EMFA=EMFACT(J,I)
                PMNS=PLGNDR(I,J,XS)
                PMNO=PLGNDR(I,J,XO)
                PMNOD=PLGNDR(I,J+1,XO)
                IF (XOS .EQ. 0.0D0) THEN
                   PMNOS=PS(I,J,XO)
                ELSE
                   PMNOS=PMNO/XOS
                END IF
                RPHI=J*(PHIO-PHIS)
                PHIMJ=EMFA*PMNS*PMNOD*(-1)*DCOS(RPHI)
                PHINJ=EMFA*PMNS*PMNOS*(-J)*DSIN(RPHI)
                SUMMP=SUMMP+PHIMJ
                SUMNP=SUMNP+PHINJ
2003         CONTINUE
             ESPHI3=ESPHI3+(PHIMI*SUMMP+PHINI*SUMNP)
             ABD3=ESPHI3
             IF (I .EQ. 0) ABD3=1.0D0
             ABE3=CDABS((ABD3-ABC3)/ABD3)
             IF (ABE3 .LT. CONV) GOTO 1233
1003      CONTINUE
1233      ESPHI=ESPHI3
          RETURN
          END
```

```
C
C A set of subroutines to compute the functions of the
C spherical wave expansion technique to evaluate the
C total electric field
C
      SUBROUTINE RN (XKP,N,ARN,BRN)
      IMPLICIT REAL*8 (A-H,O-Z)
      COMPLEX*16 HNP,HNPD,ARN,BRN
      INTEGER*4 N
      DIMENSION ZJ(82),ZY(82)
      CALL BEJH (XKP,N,ZJ)
         BJP=ZJ(N+1)
         BJPM=ZJ(N)
      BNPD=XKP*BJPM+(N)*BJP
      CALL BEYH (XKP,N,ZY)
         BYP=ZY(N+1)
         BYPM=ZY(N)
      YNPD=XKP*BYPM+(N)*BYP
      HNP=DCMPLX(BJP,-BYP)
      HNPD=DCMPLX(BNPD,-YNPD)
      ARN=-BJP/HNP
      IF (N .EQ. 0) THEN
         HNPD=1.D0
      END IF
      BRN=-BNPD/HNPD
      RETURN
      END
C
C
      SUBROUTINE BNOD (XKB,N,BNBD)
      IMPLICIT REAL*8 (A-H,O-Z)
      INTEGER*4 N
      DIMENSION Z(82)
      PI=DACOS(-1.0D0)
      CALL BEJH (XKB,N,Z)
         BJB=Z(N+1)
         BJBM=Z(N)
      BNBD=XKB*BJBM+(N)*BJB
      IF (N .EQ. 0) BNBD=0.0D0
      RETURN
      END
C
C
      SUBROUTINE HND (XKB,N,HNBDS)
      IMPLICIT REAL*8 (A-H,O-Z)
      COMPLEX*16 HNBD,HNBDS
      INTEGER*4 N
      DIMENSION Z(82),W(82)
      PI=DACOS(-1.0D0)
      CALL BEJH (XKB,N,Z)
         BJB=Z(N+1)
         BJBM=Z(N)
      BNBD=XKB*BJBM+(N)*BJB
      CALL BEYH (XKB,N,W)
         BYB=W(N+1)
         BYBM=W(N)
      YNBD=XKB*BYBM+(N)*BYB
      HNBDS=DCMPLX(BNBD,-YNBD)
      IF (N .EQ. 0) HNBDS=DCMPLX(0.0D0,0.0D0)
      RETURN
```

```
      END
C
C Subroutine to compute the spherical Hankel function
C
      SUBROUTINE HN (XKB,N,HNBS)
      IMPLICIT REAL*8 (A-H,O-Z)
      COMPLEX*16 HNB,HNBS
      INTEGER*4 N
      DIMENSION ZJ(82),ZY(82),GAM(82)
      PI=DACOS(-1.0D0)
      COT=DSQRT(PI/(2.0*XKB))
      IF (XKB .GT. 0.01) THEN
         CALL BEJH (XKB,N,ZJ)
            BJB=ZJ(N+1)
         CALL BEYH (XKB,N,ZY)
            BYB=ZY(N+1)
         HNBS=DCMPLX(BJB,-BYB)
      ELSE
         GAM(1)=DSQRT(PI)
         XMULT=1.0D0
         DO 999 I=1,N
            XMULT=XMULT*(2.0*I-1)
            GAM(I+1)=XMULT*GAM(1)/2.0**I
999      CONTINUE
         HN2=(2.0D0/XKB)**(N+0.5D0)*GAM(N+1)/PI
         HNBS=DCMPLX(0.0D0,COT*HN2)
      END IF
      RETURN
      END
C
C Subroutine to compute the first spherical Bessel function
C
      SUBROUTINE BEJH (X,N,Z)
      IMPLICIT REAL*8 (A-H,O-Z)
      DIMENSION Z(82),GAM(82)
      INTEGER*4 N
      PI=DACOS(-1.0D0)
      IF (X .LT. 1.0D-10) X=1.0D-10
      CO=1.0D0/X
      COT=DSQRT(PI/(2.0D0*X))
      IF (X .GT. 0.30) THEN
         Z(1)=CO*DSIN(X)
         IF (N)1,1,2
2        Z(2)=CO*(DSIN(X)/X-DCOS(X))
         IF (N-1)1,1,3
3        DO 4 I=2,N
            Z(I+1)=(2.0*(I-0.5D0)/X)*Z(I)-Z(I-1)
4        CONTINUE
      ELSE
         GAM(1)=DSQRT(PI)
         XMULT=1.0D0
         DO 999 I=1,N+1
            XMULT=XMULT*(2.0*I-1)
            GAM(I+1)=XMULT*GAM(1)/2.0**I
999      CONTINUE
         Z(1)=COT*(X**0.5D0/(2.0**0.5D0*GAM(2)))
         DO 777 J=1,N
            Z(J+1)=COT*(X**(J+0.5D0)/(2.0**(J+0.5D0)*GAM(J+2)))
777      CONTINUE
         END IF
```

```
1     RETURN
      END
C
C Subroutine to compute the second spherical Bessel function
C
      SUBROUTINE BEYH (X,N,Z)
      IMPLICIT REAL*8 (A-H,O-Z)
      DIMENSION Z(82),GAM(82)
      INTEGER*4 N
      PI=DACOS(-1.0D0)
      IF (X .LT. 1.0D-10) X=1.0D-10
      CO=1.0D0/X
      COT=DSQRT(PI/(2.0D0*X))
      IF (X .GT. 0.02) THEN
         Z(1)=-CO*DCOS(X)
         IF (N)1,1,2
2        Z(2)=-CO*(DSIN(X)+DCOS(X)/X)
         IF (N-1)1,1,3
3        DO 4 I=2,N
            Z(I+1)=(2.0*(I-0.5D0)/X)*Z(I)-Z(I-1)
4        CONTINUE
      ELSE
         GAM(1)=DSQRT(PI)
         XMULT=1.0D0
         DO 999 I=1,N
            XMULT=XMULT*(2.0*I-1)
            GAM(I+1)=XMULT*GAM(1)/2.0**I
999      CONTINUE
         Z(1)=-COT*((2.0**0.5D0*GAM(1))/(PI*X**0.5D0))
         DO 777 J=1,N
            Z(J+1)=-COT*((2.0**(J+0.5D0)*GAM(J+1))/(PI*X**(J+0.5D0)))
777      CONTINUE
         END IF
1     RETURN
      END
C
C
      FUNCTION EMFACT (M,N)
      IMPLICIT REAL*8 (A-H,O-Z)
      INTEGER*4 M,N,ITOP,IBOT
      ITOP=N-M
      IBOT=N+M
      TOP=FACTP(ITOP)
      BOT=FACTP(IBOT)
      TB=(TOP/BOT)
      IF (M .EQ. 0) THEN
         EMFACT=TB
      ELSE
         EMFACT=2.0D0*TB
      END IF
      RETURN
      END
C
C
      FUNCTION FACTP (N)
      REAL*8 FACTP
      INTEGER*4 N
      FACTP=1.0D0
      IF (N .LT. 1) GOTO 2
      DO 10 I=2,N
```

```
          FACTP=FACTP*I
10      CONTINUE
2       RETURN
        END
C
C Subroutine to compute the Associate Legendre Polynomials
C
        FUNCTION PLGNDR(L,M,X)
        REAL*8 X,PMM,SOMX2,FACT,PMMP1,PLL,PLGNDR
        INTEGER*4 L,M,LL
        PMM=1.0D0
        IF(M .GT. 0) THEN
           SOMX2=DSQRT((1.0D0-X)*(1.0D0+X))
           FACT=1.0D0
           DO 10 I=1,M
              PMM=-PMM*FACT*SOMX2
              FACT=FACT+2.0D0
10         CONTINUE
        END IF
        IF(L .EQ. M) THEN
           PLGNDR=PMM
        ELSE
           PMMP1=X*(2.0D0*M+1)*PMM
           IF(L. EQ. M+1) THEN
              PLGNDR=PMMP1
           ELSE
              DO 20 LL=M+2,L
                 PLL=(X*(2.0D0*LL-1)*PMMP1-(LL+M-1)*PMM)/
     +                (LL-M)
                 PMM=PMMP1
                 PMMP1=PLL
20            CONTINUE
              PLGNDR=PLL
           END IF
        END IF
        IF (L .LT. M) THEN
           PLGNDR=0.0D0
        END IF
        RETURN
        END
C
C
          FUNCTION PS(N,M,X)
          IMPLICIT REAL*8 (A-H,O-Z)
          INTEGER*4 M,N
          PI=DACOS(-1.0D0)
          XAB=DABS(X)
          SM=1.0D0-XAB
          IF(SM .LT. 1.0D-10) THEN
             IF (X .GT. 0.0D0) THEN
                PS=(-1)**(M)*((N*(N+1))/2.0D0)
             ELSE
                PS=(-1)**(N+M-1)*((N*(N+1))/2.0D0)
             END IF
          END IF
          RETURN
          END
```

BIBLIOGRAPHY

[1] A.W. Rudga, K. Milne, A.D. Olver, & R.Knight, "*The handbook of antenna design vol.2*" pp.717-178, p.781.

[2] J.A. Stratton, "*Electromagnetic Theory*," pp. 393-421, pp. 563-587, McGraw Hill, New York, 1941.

[3] A. Sommerfeld, "Uber die Ausbreitung der drahtlosen Telegraphie," *Ann. Phys.*, vol. 28, pp. 665-736, 1909.

[4] A. Karwowski, "Low-frequency approach to the problem of a horizontal wire antenna above an imperfect ground," *IEE Proceeding*, vol. 131, Pt.H., no. 3, pp. 214-216, June 1984.

[5] A. Karwowski, "Low-frequency approach to the problem of a vertical wire antenna above an imperfect ground," *IEE Proceeding*, vol. 132, Pt.H., no. 2, pp. 123-126, April 1985.

[6] Y. Rahmat-Samii, R. Mittra and P. Parhami, "Evaluation of Sommerfeld integrals for lossy half-space problems," *Electromagnetics*, vol. 1, no. 1, pp. 1-28, 1981.

[7] I.S. Lindell and E. Alanen, "Exact Image Theory for the Sommerfeld Half-Space Problem, Part I: Vertical Magnetic Dipole," *IEEE Trans. Antennas and Propagation*, vol. AP-32, no. 2, pp. 126-133, Feb. 1984.

[8] I.S. Lindell and E. Alanen, "Exact Image Theory for the Sommerfeld Half-Space Problem, Part II: Vertical Electric Dipole," *IEEE Trans. Antennas and Propagation*, vol. AP-32, no. 8, pp. 841-847, Aug. 1984.

[9] I.S. Lindell and E. Alanen, "Exact Image Theory for the Sommerfeld Half-Space Problem, Part III: General Formulation," *IEEE Trans. Antennas and Propagation*, vol. AP-32, no. 10, pp. 1027-1032, Oct. 1984.

[10] J.R. Wait, "Image Theory of a Quasi-Static Magnetic dipole over a Dissipative Half-space," *Electronic Letters*, vol. 5, no. 13, pp. 281-282, 1969.

[11] G.J. Burke, E.K. Miller et al, "Computer Modeling of Antenna near the Ground," *Electromagnetics*, vol. 1, pp. 29-49, 1981.

[12] G.J. Burke and E.K. Miller, "Modeling Antenna Near to and Penetrating a Lossy Interface," *IEEE Trans. Antennas and Propagation*, vol. AP-32, no. 10, pp. 1040-1049, Oct. 1984.

[13] R.F. Harrington, "*Field Computation by Moment Method*," pp.1-19, 127-150, Second edition, New York, 1968.

[14] M.M. Ney, "Method of Moments as Applied to Electromagnetic Problems," *IEEE Trans. Microwave theory and Tech.*, vol. MTT-33, no. 10, pp. 972-980, Oct. 1985.

[15] G. Costache, "*course notes for Numerical Methods in Electromagnetic Engineering*," University of Ottawa, 1986.

[16] E.K. Miller *et al.* "Analysis of Wire Antenna in the presence of a Conducting half-space. part I. The Vertical Antenna in Free Space," *Canadian Journal of Physics* vol. 50, pp. 879-888, 1972.

[17] E.F. Kuester and D.C. Chang, "Evaluation of Sommerfeld integrals associated with dipole sources above earth," *Univ. Colorada, Electromagnetics Lab.,Sci. Rep.*, pp. 182-188, Jan. 1979.

[18] G.H. Wong, S.S. Stuchly, A. Kraszewski and M.A. Stuchly, "Probing Electromagnetic Fields in Lossy Spheres and Cylinders," *IEEE Trans. Microwave Theory and Tech.*, vol. MTT-32, no. 8, pp. 824-828, Aug. 1984.

[19] F.V. Schultz, R.C. Burgener and S. King, "Measurement of the Radar Cross Section of a Man," *Proceeding of the IRE*, pp. 476-481, Feb. 1958.

[20] H. Massoudi et al., "A geometrical-optic and an exact solution for internal fields in and energy absorption by a cylindrical model of man irradiated by an electromagnetic plane wave," *Radio Science*, vol. 14, no. 6S, pp. 35-42, Nov.-Dec. 1979.

[21] R.W.P. King and C.W. Harrison, Jr., "Scattering by Imperfectly Conducting Spheres," *IEEE Trans. Antennas and Propagation*, vol. AP-19, no. 2, pp. 197-207, March 1971.

[22] A.C. Ludwig, "Near-Filed Far-Field Transformations Using Spherical-Wave Expansions," *IEEE Trans. Antennas and Propagation*, vol. AP-19, no. 2, pp. 214-220, March 1971.

[23] P.D. Potter, "Application of Spherical Wave Theory to Cassegrainian Fed Paraboloids," *IEEE Trans. Antennas and Propagation*, vol. AP-15, no. 6, pp. 727-736, Nov. 1967.

[24] S.W. Lee, V. Jamnejad and R. Mittra, "Near Field of Scattering by a Hollow Semi-Infinite Cylinder and Its Application to Sensor Booms," *IEEE Trans. Antennas and Propagation*, vol. AP-21, no.2, pp. 182-188, March 1973.

[25] R.F. Harrington, "*Time-Harmonic Electromagnetic Fields*," McGraw-Hill, New York, 1961.

[26] R.F. Harrington, "*Introduction to Electromagnetic Engineering*," p.196, pp.276-283, McGraw-Hill, New York, 1958.

[27] Edited by Uslenghi, "*Electromagnetic Scattering*," Academic Press, New York, 1978.

[28] S.A. Schelkunoff, "*Advanced Antenna Theory*," pp.153-160, Wiley, New York, 1952.

[29] S.A. Schelkunoff, "*Antenna Theory and Practice*," pp.579-580, Wiley, New York, 1952.

[30] S.A. Schelkunoff, "*Electromagnetic Field*," Blaisdell, New York, 1963

[31] S.A. Schelkunoff, "*Applied Mathematics for Engineers and Scienists*," Princeton, Van Nostrand, New York, 1965.

[32] W.R. Smythe, "*Static and Dynamic Electricity*," pp.142-167, Third edition, McGraw-Hill, New York, 1968.

[33] D.S. Jones, "*The Theory of Electromagnetism*," pp.65-93, pp.483-502, Pergamon Press, MacMillian, New York, 1964.

[34] J.R. Mentzer, "*Scattering and Diffraction of radio waves*," Pergamon Press, London, New York, 1955.

[35] J.K. Raines, "Improve antenna design using 19^{th}-Century math," *Microwave & RF*, pp. 167-170, May 1986.

[36] W.L. Stuzman & G.A. Thiele, "*Antenna Theory and design*," John Wiley & sons, New York, 1981.

[37] J.A. Kong, "*Theory of Electromagnetic Waves*," Wiley, New York, 1975.

[38] D.J. Gale & J.C. Beal, "Comparative testing of Leaky coaxial cables for communications and Guider radar," *IEEE Trans. Microwave theory & Techniques*, vol. MTT-28, no. 9, pp. 1006-1013, Sept. 1980.

[39] S.S. Stuchly *et al.*, "Computer-based scanning system for electromagnetic dosimetry," *Rev. Sci. Instrum.*, 54(11), pp.1547-1550, Nov 1983.